

Search for electroweak production of supersymmetry  
in events with two tau leptons in the final state with  
the ATLAS detector at the LHC

Suche nach elektroschwacher Produktion von  
Supersymmetrie in Ereignissen mit zwei Tau  
Leptonen im Endzustand mit dem ATLAS Detektor  
am LHC



Masterarbeit an der Fakultät für Physik  
der  
Ludwig-Maximilians-Universität München

vorgelegt von

**Fabian Rücker**

geboren am 27.04.1989 in Köln

2.08.2013

Gutachterin: Prof. Dr. Dorothee Schaile

---

# Table of Contents

<b>1</b>	<b>Introduction</b>	<b>1</b>
<b>2</b>	<b>Theoretical Foundations</b>	<b>3</b>
2.1	The Standard Model	3
2.2	Remaining Challenges of the Standard Model	5
2.3	Supersymmetry	6
2.3.1	Supersymmetry breaking	7
2.3.2	The Minimal Supersymmetric Model (MSSM)	8
2.3.3	The pMSSM	9
2.3.4	Weak production of gauginos and sleptons	10
2.3.5	Decay of gauginos and sleptons	10
<b>3</b>	<b>Experimental Setup</b>	<b>14</b>
3.1	The Large Hadron Collider	14
3.2	The ATLAS detector	16
3.2.1	ATLAS coordinate system	17
3.2.2	Magnet System	18
3.2.3	Inner detector	19
3.2.4	The Electromagnetic Calorimeter	22
3.2.5	The Hadronic Calorimeter	23
3.2.6	Muon Spectrometer	23
3.2.7	Forward Detectors	26
3.2.8	Trigger and Data Acquisition	27
3.2.9	Computing Infrastructure	28

<b>4</b>	<b>Analysis</b>	<b>29</b>
4.1	Object Definitions	29
4.1.1	Jets	29
4.1.2	Taus	30
4.1.3	Electrons	31
4.1.4	Muons	31
4.1.5	Missing Transverse Energy	31
4.2	Overlap Removal	33
4.3	Event Quality Criteria	34
4.4	Trigger Selection	34
<b>5</b>	<b>Search for direct stau production</b>	<b>36</b>
5.1	Direct stau production	36
5.1.1	Data Samples	37
5.2	Standard Model Background	38
5.2.1	Estimation of the QCD multijet background	38
5.3	Statistics	43
5.3.1	Hypothesis Test	43
5.3.2	Exclusion Limits	44
5.4	Preselection	45
5.5	Signal Region	50
5.6	Exclusion limits	55
<b>6</b>	<b>Further optimization studies of direct gaugino and direct stau searches</b>	<b>59</b>
6.1	Number of taus	62
6.2	Trigger thresholds	66
<b>7</b>	<b>Conclusion and Outlook</b>	<b>68</b>
	<b>Appendices</b>	<b>68</b>
<b>A</b>	<b>Variable Distributions in the OS region</b>	<b>69</b>

<b>B Variable Distributions in the OS+Preselection region . . . . .</b>	<b>77</b>
<b>Bibliography . . . . .</b>	<b>85</b>

---

# CHAPTER 1

## Introduction

The idea that matter can be broken down into elementary indivisible building blocks has been around since ancient times and found its embodiment in the term 'atom', which means 'the indivisible'.

In 1897 J.J. Thompson discredited the atom as an elementary particle since he discovered the electron and formulated the Thompson Model of the atom in 1904.

Since then a multitude of elementary particles has been found and theoretical frameworks have been developed to accommodate them. In the 1960's the modern form of the Standard Model was formulated. It describes all elementary particles and their interactions, excluding gravity, in the framework of two quantum theories. Quantum Chromodynamics (QCD) covers the strong interaction between quarks and the nuclear force between protons and neutrons in an atom. The electromagnetic and the weak interaction are unified in the electroweak theory.

One aspect of the Standard Model that is not confirmed by experiment yet, is the mechanism how fermions and massive gauge bosons acquire their mass. The proposed Higgs mechanism, which breaks the electroweak symmetry, introduces a scalar boson called the Higgs boson. In 2012 the search for the Higgs boson greatly progressed with the discovery of a higgs-like boson at ATLAS [1] and CMS [2].

However the introduction of the Higgs boson leads to a fine-tuning problem as the mass of the Higgs boson depends on contributions from all particles coupling to it. To stabilize the Higgs mass a high level of fine-tuning is necessary. The fine-tuning problem can be solved in supersymmetric extensions (SUSY) of the Standard Model which introduces a new symmetry between bosons and fermions. SUSY also provides a dark matter candidate and gauge coupling unification. In addition the theory of general relativity can be incorporated in SUSY.

Some of the new elementary particles introduced in SUSY may be produced and detectable at the LHC. The particle content of a supersymmetric extension of the Standard Model depends on the SUSY model that is chosen. In this thesis electroweak production of supersymmetric particles in  $p$ - $p$  collisions at the LHC at  $\sqrt{s} = 8$  TeV is studied in the framework of the phenomenological minimal supersymmetric model (pMSSM). Specifically the electroweak production of staus, charginos and neutralinos is studied. The stau is the superpartner of the tau and is assumed to be light in the pMSSM. Charginos (neutralinos) arise from mixing of the superpartners of the charged (neutral) SM bosons in the electroweak sector.

In this thesis events with hadronically decaying taus and no light leptons in the fi-

nal state are selected. This complements previous studies on electroweak production of supersymmetric particles carried out by the ATLAS collaboration which covered final states with electrons and muons where the neutralinos and charginos decay with equal probability to all lepton flavours [3][4][5]. Furthermore the CMS collaboration has presented preliminary limits on the chargino and neutralino masses in tau dominated scenarios [6].

This thesis is structured as follows. Chapter 2 covers the theoretical foundations. The current status of the Standard Model is reviewed and supersymmetry and the phenomenological minimal supersymmetric model (pMSSM) are introduced. In chapter 3 the experimental setup, namely the Large Hadron Collider (LHC) and the ATLAS experiment, is described.

This thesis covers two separate electroweak production channels leading to a final state with hadronically decaying taus, which are both studied in the framework of the pMSSM and assuming R-parity conservation (introduced in Section 2.3.3). Both studies share the same analysis outline which is presented in chapter 4. In chapter 6 event selection criteria for weak production of gauginos and staus with subsequent decay to taus are studied at Truth level. An analysis for the exclusive search for direct stau production is presented in chapter 5. A signal region is developed and exclusion limits on the direct stau production cross-section are computed. Finally chapter 7 gives a conclusion and an outlook.

---

# CHAPTER 2

## Theoretical Foundations

### 2.1 The Standard Model

The Standard Model (SM) is a well established theory describing fundamental particles and their interactions. It has been tested to a high precision in numerous experiments. The short overview given here is based on [7], [8] and [9].

The particle content of the SM consists of three generations of fermions, the gauge bosons and the Higgs boson. Fermions are by definition particles characterized by Fermi-Dirac statistics with half integer spin<sup>1</sup>. Each generation of fermions consists of an up- and a down-type quark, a charged lepton and a neutral leptonic neutrino. An overview of the SM fermions, their respective charges and masses is shown in Table 2.1. Furthermore each fermion has its own antiparticle with the same mass and spin but oppositely signed charge quantum numbers.

The Standard Model describes the strong, weak and electromagnetic interaction, with the latter two unified in the electroweak theory.

The interactions are mediated by so called "gauge bosons" that are summarized in Table 2.2. Bosons are characterized by Bose-Einstein statistics and have integer spin. The mediator of the electromagnetic interaction is the massless photon  $\gamma$ , which couples to the electric charge of particles. The weak interaction, which is unique in the way that it allows flavour changing charged currents at tree level, is caused by the emission or absorption of the massive  $Z$ -Boson and the massive  $W$ -Bosons. They couple to the weak isospin of particles.

The strong force, which binds protons and neutrons and also the quarks in hadronic particles together, is mediated by massless gluons.

There are 8 gluons that mediate the strong interaction between coloured particles. The different colour charges are referred to as red, green, blue and the corresponding anti-colours anti-red, anti-green and anti-blue.

Quarks are subject to all three fundamental forces in the SM as they also carry colour while leptons that do not carry colour only take part in electroweak interactions.

The mathematical framework of the Standard Model is that of a Quantum Field Theory. Using the Lagrangian formalism the equation of motion of a particle, that is represented by a quantum field, can be determined from a Lagrangian density using the Euler-Lagrange equation.

---

<sup>1</sup>In this thesis natural units are used.  $\hbar = 1$  and  $c = 1$



### Quarks

Generation	Name	Symbol	Charge [e]	Mass [MeV]
1	up	$u$	$+\frac{2}{3}$	1.5 to 3.3
	down	$d$	$-\frac{1}{3}$	3.5 to 6.0
2	charm	$c$	$+\frac{2}{3}$	$(1.27 \pm 0.03) \cdot 10^3$
	strange	$s$	$-\frac{1}{3}$	$95 \pm 5$
3	top	$t$	$+\frac{2}{3}$	$(173.1 \pm 1.24) \cdot 10^3$
	bottom	$b$	$-\frac{1}{3}$	$(4.66 \pm 0.03) \cdot 10^3$

### Leptons

1	electron	$e$	-1	0.511
	electron-neutrino	$\nu_e$	0	$< 2.2 \cdot 10^{-6}$
2	muon	$\mu$	-1	105.7
	muon-neutrino	$\nu_\mu$	0	$< 170 \cdot 10^{-3}$
3	tau	$\tau$	-1	1776.8
	tau-neutrino	$\nu_\tau$	0	$< 18.2$

Table 2.1: The fermion particle content of the SM. All fermions have a spin of  $\frac{1}{2}$  and also an antiparticle [10].

Name	Symbol	Interaction	Charge[e]	Mass [GeV]
gluon	$g$	strong	0	0 (theory)
photon	$\gamma$	electromagnetic	0	0 (theory)
W-Boson	$W^\pm$	weak	$\pm 1$	$80.385 \pm 0.015$
Z-Boson	$Z$	weak	0	$91.1876 \pm 0.0021$

Table 2.2: The gauge bosons of the Standard Model [10].

In the SM the strong interaction with its gauge bosons, the gluons, is described in the quantum theory of Quantum Chromodynamics (QCD) and the weak and electromagnetic interaction, with the photon  $\gamma$ , the  $Z$  boson and the  $W^\pm$  bosons as its gauge bosons, in the electroweak theory.

Both of these quantum field theories are gauge theories in which the Lagrangian density is invariant under a continuous group of local transformations. For the case of QCD this is the group  $SU(3)$  and for the electroweak theory it is  $U(1) \otimes SU(2)$ .

The electroweak theory predicts massless gauge bosons due to the fact that a mass term in the Lagrangian for the gauge bosons would break local gauge invariance. However the  $Z$  and  $W$  bosons are found to be massive in experiment. The Higgs Mechanism provides a solution for this problem. A complex scalar field, the Higgs field, is introduced and the  $SU(2) \otimes U(1)$  symmetry is spontaneously broken via the Higgs mechanism. Via this mechanism the  $Z$  and  $W^\pm$  bosons acquire their mass. In addition the Higgs mechanism introduces another scalar particle, the Higgs boson, and fermions obtain their mass by a Yukawa interaction with the Higgs field.

## 2.2 Remaining Challenges of the Standard Model

This section is based on [11]. The Standard Model (SM) has been highly successful and has been tested to high precision over an energy range from a fraction of an electron Volt to about 100 GeV. The search for the Higgs boson, which is a building block of the Standard Model, has greatly progressed with the discovery of a Higgs-like boson at ATLAS [1] and CMS [2] in 2012. However there are open questions and inconsistencies which make the Standard Model an incomplete theory. There are a number of observations made through experiment that remain unexplained in the Standard Model:

- The existence of dark matter that has been established by studies of the fluctuations in the spectrum of the relic microwave background from the big bang [12], [13] and gravitational lensing measurements of the Bullet Cluster [14].
- Most of the energy of the universe is "dark energy". This is suggested by observations of type Ia supernovae at large red shifts [15] as well as the cosmic microwave background radiation [16].
- The existence of gravity.

In addition to these observations there also exist theoretical arguments that suggest that the Standard Model is incomplete. The Standard Model has a number of free parameters such as the fermion masses, the Higgs boson mass, mixing angles and the gauge coupling strengths of the strong, weak and electromagnetic forces. Grand Unified Theories (GUT) attempt to unify these three forces which means that the coupling strengths should reach the same strength. This can be achieved in supersymmetric models such as the MSSM but not in the Standard Model (see Figure 2.1).

Another problem of the Standard Model is a hierarchy problem. In contrast to fermion masses which are protected by symmetry and the gauge boson masses which are protected by gauge invariance, the divergence structure of field theories with elementary scalars is quite different. Radiative corrections to the scalar Higgs boson in the Standard Model, like the ones from Feynman diagrams shown in Figure 2.2, are quadratically divergent. There are quadratically divergent contributions from gauge boson loops, fermion loops and scalar loops like the higgs boson self-coupling loops. However the top quark loop contribution dominates. These loop corrections would make the Higgs mass huge, comparable to the scale at which new physics appears (i.e. Planck scale), unless there is a fine-tuned cancellation between the quadratic radiative corrections. Therefore this problem is often referred to as a fine-tuning or naturalness problem.

Corrections from fermion and boson loops contribute with a different sign. In supersymmetric theories corrections from fermion (boson) loops are exactly cancelled out by the corrections from the loops involving their respective bosonic (fermionic) superpartners which have the same mass. Therefore the problem is solved in supersymmetric theories.

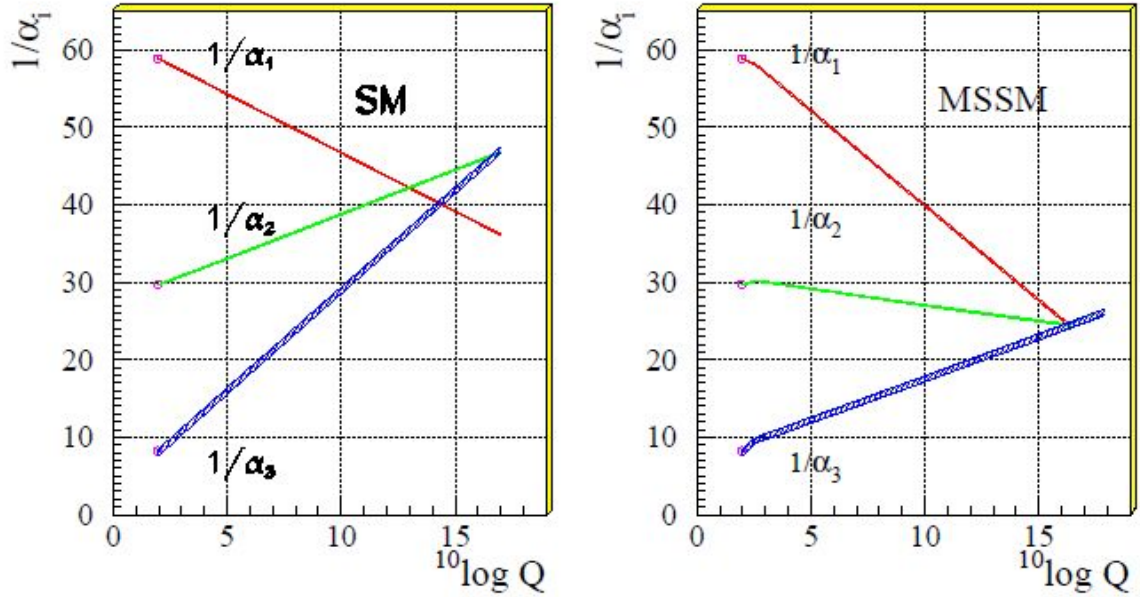


Fig. 2.1: Evolution of the inverse of the three coupling constants in the Standard Model (left) and in the MSSM (right).  $\alpha_1$ ,  $\alpha_2$  and  $\alpha_3$  correspond to the U(1), SU(2) and SU(3) gauge coupling constants. [17]



Fig. 2.2: One-loop quantum corrections to the Higgs squared mass parameter  $m_H^2$ , due to a fermion  $f$  (left) and a scalar  $S$  (right) [18].

## 2.3 Supersymmetry

This section is based on [18]. Supersymmetry (SUSY) is a promising theoretical framework that provides solutions for problems of the Standard Model. Most notably supersymmetric theories solve the hierarchy problem and provide gauge coupling unification (see Fig 2.1). Furthermore supersymmetric models can incorporate gravity and provide a natural dark matter candidate. The underlying symmetry of SUSY is a spacetime symmetry between boson and fermion fields which can be transformed into one another via the operator  $Q$ :

$$Q |Boson\rangle = |Fermion\rangle \quad Q |Fermion\rangle = |Boson\rangle \quad (2.1)$$

$Q$  and  $Q^\dagger$  are anticommuting spinors that carry spin angular momentum  $\frac{1}{2}$  and satisfy the supersymmetric algebra which reads

$$\{Q_s, Q_r^\dagger\} = -2\sigma_{sr}^\mu P_\mu \quad (2.2)$$

$$\{Q_s, Q_r\} = 0 \quad (2.3)$$

$$\{Q_s^\dagger, Q_r^\dagger\} = 0 \quad (2.4)$$

where  $P^\mu$  is the four-momentum generator of spacetime translations. Irreducible representations of the supersymmetry algebra are called supermultiplets and contain both fermion and boson fields. A field  $|\Omega'\rangle$  is proportional to a combination of  $Q$  and  $Q^\dagger$  operators acting on  $|\Omega\rangle$  up to a spacetime translation or rotation if  $|\Omega\rangle$  and  $|\Omega'\rangle$  are members of the same supermultiplet. The fermion and boson fields in a supermultiplet are called superpartners and each supermultiplet has an equal number of fermionic and bosonic degrees of freedom.

Furthermore the operator  $P^2$  commutes with the operators  $Q, Q^\dagger$  and with all the spacetime rotation and translation operators. Therefore members of the same supermultiplet have equal eigenvalues of  $P^2$  and thus equal masses. Members of the same multiplet also have the same electric charge, weak isospin and color degrees of freedom which follows from the fact that the supersymmetry generators  $Q, Q^\dagger$  commute with the generators of gauge transformations. To summarize, members of the same supermultiplet have the same mass and quantum numbers but different spin.

As no supersymmetric particle has been observed yet, supersymmetry must be a broken symmetry and the superpartners of SM particles must have significantly larger masses.

### 2.3.1 Supersymmetry breaking

Supersymmetry is a broken symmetry. In an unbroken supersymmetric theory the quadratically divergent contributions from loop Feynman diagrams (such as in Figure 2.2) exactly cancel. For example the quadratically divergent contribution from a fermion loop

$$\Delta m_H^2 = -\frac{|\lambda_f|^2}{8\pi^2} \Lambda_{UV}^2 \quad (2.5)$$

is cancelled by the introduction of two complex scalar fields that contribute each to the higgs mass correction as

$$\Delta m_H^2 = \frac{\lambda_S}{16\pi^2} \left[ \Lambda_{UV}^2 - 2m_S^2 \ln \left( \frac{\Lambda_{UV}}{m_S} \right) + \mathcal{O} \left( \frac{1}{\Lambda^2} \right) \right]. \quad (2.6)$$

Here  $\Lambda_{UV}$  denotes the energy scale at which new physics appears and  $\lambda_f$  ( $\lambda_S$ ) is the respective coupling constant of the yukawa coupling of a fermion (scalar) field to the Higgs field.

To achieve cancellation the associated dimensionless couplings should be related (in this case  $\lambda_s = |\lambda_f|^2$ ). In order for supersymmetric theories to provide a solution to

the hierarchy problem even in the case that supersymmetry is broken, the relationship between the dimensionless couplings must be maintained. Otherwise the Higgs mass would for example receive quadratically divergent corrections of the form

$$\Delta m_H^2 = \frac{1}{8\pi^2} (\lambda_s - |\lambda_f^2|) \Lambda_{UV}^2 + \dots \quad (2.7)$$

This leads to the notion to consider "soft" supersymmetry breaking. The effective Lagrangian of the MSSM can be written as

$$\mathcal{L} = \mathcal{L}_{SUSY} + \mathcal{L}_{soft} \quad (2.8)$$

where  $\mathcal{L}_{SUSY}$  covers all the gauge and Yukawa interactions and preserves supersymmetry invariance.  $\mathcal{L}_{soft}$  violates supersymmetry but the mass terms and coupling parameters only have positive mass dimension. Furthermore corrections to the Higgs mass must be of the form

$$\Delta m_H^2 = m_{soft}^2 \left[ \frac{\lambda}{16\pi^2} \ln \left( \frac{\Lambda_{UV}}{m_{soft}} \right) + \dots \right] \quad (2.9)$$

Here  $\lambda$  denotes various dimensionless couplings and the additional terms are independent of  $\Lambda_{UV}$  and come from higher loop corrections. To ensure that the correction to the Higgs mass remains small compared to the scale of the electroweak breaking of 174 GeV,  $m_{soft}$  should be small and therefore mass splitting between superpartners is reasonably small. If we assume  $\Lambda_{UV} \sim M_P$  and  $\lambda \sim 1$  it can be shown that the masses of at least the lightest few superpartners should not be much larger than 1 TeV. This energy range is accessible at the LHC.

### 2.3.2 The Minimal Supersymmetric Model (MSSM)

It is theoretically possible to build different supersymmetric models to extend the Standard Model. One of them is the Minimal Supersymmetric Model (MSSM). The MSSM contains the smallest number of new particles and new interactions consistent with the known phenomenology. For each chiral fermion in the Standard model there is a pair of spin-0 particles (particle and antiparticle), called sfermions, with the same internal quantum numbers as the fermion.

The naming convention for the superpartners of fermions is to add an s in front of its name (for example selectron, smuon, squark). The subscripts L and R on the sfermion mass eigenstates indicate only the chirality of their respective superpartner as they are spin-0 particles and cannot have handedness or chirality.

The superpartners of the Higgs and gauge fields are fermionic higgsinos and gauginos respectively. The Higgs doublet of the SM is promoted to a doublet of superfields and a second Higgs doublet has to be introduced. That is due to the fact that a single Higgs doublet cannot be solely responsible for the mass of both up- and down-type fermions. The MSSM imposes R-parity conservation to forbid baryon and lepton number violation. R-parity is defined as

$$P_R = (-1)^{2s+3B+L} \quad (2.10)$$

Particle	Notation	Spin	Sparticle	Notation	Spin
left-handed quark	$q_L$	$\frac{1}{2}$	'left-handed' squark	$\tilde{q}_L$	0
right-handed quark	$q_R$	$\frac{1}{2}$	'right-handed' squark	$\tilde{q}_R$	0
left-handed lepton	$l_L$	$\frac{1}{2}$	'left-handed' slepton	$\tilde{l}_L$	0
right-handed lepton	$l_R$	$\frac{1}{2}$	'right-handed' slepton	$\tilde{l}_R$	0
gluon	$g$	1	gluino	$\tilde{g}$	$\frac{1}{2}$
W Bosons	$W^\pm$	1	charginos	$\tilde{\chi}_{1,2}^\pm$	$\frac{1}{2}$
charged Higgs	$H^\pm$	0			
Z boson	$Z^0$	1	neutralinos	$\tilde{\chi}_{1,2,3,4}^0$	$\frac{1}{2}$
photon	$\gamma$	1			
neutral Higgs	$H_0$	0			

Table 2.3: The MSSM mass eigenstates

with spin  $S$ , baryon number  $B$  and lepton number  $L$ .

Standard Model particles and the Higgs bosons have an R-parity of +1 and sparticles of  $-1$ . Therefore sparticles can only be produced in pairs and the lightest supersymmetric particle (LSP) is stable. In R-parity conserving models the nature of cold dark matter is explained as a relic density of stable LSP's.

Table 2.3 lists the mass eigenstates of the newly added particles of the MSSM and their respective spin. The chargino (neutralino) mass eigenstates arise from mixing of the superpartners of the charged (neutral) bosons in the electroweak sector. From the two complex Higgs doublets only two charged and three neutral spin-0 bosons are left in the physical spectrum of the MSSM. The other degrees of freedom are absorbed in the Higgs mechanism.

### 2.3.3 The pMSSM

The MSSM has over 120 free parameters. Most of the free parameters arise in the soft SUSY-breaking sector which describes the mechanism of SUSY-breaking in the MSSM. There are a number of different scenarios for SUSY-breaking, including mSUGRA [19], GMSB [20], AMSB [21] and gaugino mediated SUSY-breaking [22].

However as the nature of the breaking mechanism is not known, model-independent statements about SUSY signatures at particle colliders and the properties of the LSP are particularly important.

This approach is taken in the phenomenological MSSM in which the MSSM is constrained to have a viable phenomenology. This is done by three assumptions.

- No new source of CP-violation;
- Absence of FCNC's<sup>2</sup> at tree level;

---

<sup>2</sup>Flavour Changing Neutral Currents

- First and second sfermion generation universality.

This leaves the pMSSM with 19 real and independent parameters at the weak scale as summarized in Table 2.4.

Parameter	
$\tan \beta$	Ratio of VEVs <sup>2</sup> of the Higgs doublet fields
$\mu$	Higgs-Higgsino mixing parameter
$M_A$	Mass of the pseudoscalar Higgs boson
$M_1, M_2, M_3$	Bino, wino and gluino mass parameters
$m_{\tilde{q}}^3, m_{\tilde{u}_R}, m_{\tilde{d}_R}, m_{\tilde{l}}^4, m_{\tilde{e}_R}$	1st/2nd generation sfermion mass parameters
$m_{\tilde{Q}}^3, m_{\tilde{t}_R}, m_{\tilde{b}_R}, m_{\tilde{L}}^4, m_{\tilde{\tau}_R}$	Third generation sfermion mass parameters
$A_t, A_b, A_\tau$	Third generation trilinear couplings

Table 2.4: Free parameters of the pMSSM

### 2.3.4 Weak production of gauginos and sleptons

The size of the production cross-section of sparticle pairs at the LHC depends on the values of the parameters of the underlying theoretical model.

In Figure 2.3 the production cross-section at next-to-leading order in p-p collisions for various sparticle pairs is shown for a center of mass energy of 8 TeV at the LHC. If coloured sparticles are heavy and gauginos and sleptons are light, the production cross-sections for gauginos and sleptons may be larger than that for coloured sparticles. In this case first signs of SUSY are expected in decays of gauginos and sleptons at the LHC.

The electroweak production of supersymmetric particles at the LHC is studied in various different channels. In this thesis electroweak production processes that lead to a final state with hadronically decaying taus and not additional leptons are considered.

In chapter 6 the processes with direct gaugino production (Figure 2.4) and direct stau production (Figure 2.7) with subsequent decay to hadronically decaying taus are studied. In chapter 5 an analysis for the search for exclusively direct stau production is presented. Strong SUSY production is not considered in this thesis.

### 2.3.5 Decay of gauginos and sleptons

For the discovery of SUSY at particle accelerators, an understanding of the decay modes of sparticles and of the experimental signatures of events involving sparticles is crucial.

<sup>2</sup>Vacuum Expectation Values

<sup>3</sup>SUSY breaking squark parameter (only one for each generation of ‘left’ squarks).

<sup>4</sup>SUSY breaking slepton parameter (only one for each generation of ‘left’ sleptons).

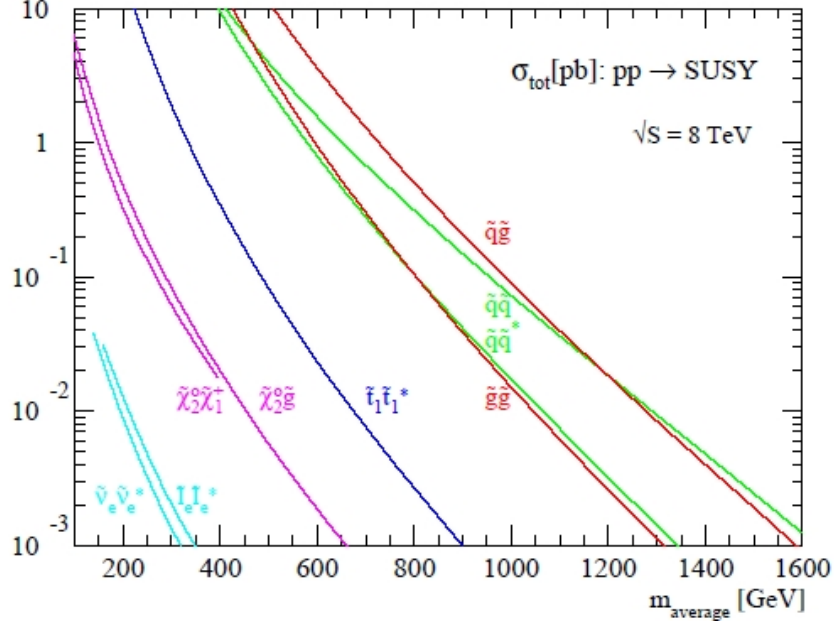


Fig. 2.3: Production cross-section in p-p collisions at  $\sqrt{s} = 8 \text{ TeV}$  as a function of the average mass of sparticles [23].

In this thesis R-parity conservation is assumed and the LSP is the lightest Neutralino  $\tilde{\chi}_1^0$  (also denoted as  $N_1$ ). In general a sparticle will decay to a lighter sparticle and a SM particle if the decay is kinematically allowed. If there is no kinematically allowed two-body decay, a three-body occurs. In this thesis only weak production of gauginos and staus is considered. The gaugino decay modes depend on the gaugino masses and on the MSSM parameters  $M_1$ ,  $M_2$ ,  $\tan(\beta)$  and  $\mu$  that enter the neutralino and chargino mixing matrices.

In the framework of the pMSSM the main decay processes for gauginos are

- $\tilde{\chi}_i^0 \rightarrow W^{\pm(*)} \tilde{\chi}_j^\mp \rightarrow l^\pm \nu \tilde{\chi}_j^\mp$
- $\tilde{\chi}_i^0 \rightarrow Z^{0(*)} \tilde{\chi}_j^0 \rightarrow l^\pm l^\mp \tilde{\chi}_j^0$
- $\tilde{\chi}_i^\pm \rightarrow Z^{0(*)} \tilde{\chi}_j^\pm \rightarrow l^\pm l^\mp \tilde{\chi}_j^\pm$
- $\tilde{\chi}_i^\pm \rightarrow W^{\pm(*)} \tilde{\chi}_j^0 \rightarrow l^\pm \nu \tilde{\chi}_j^0$

for  $i > j$  and  $i \geq 0$  ( $i, j = 0, 1, 2, 3$ ) where  $l$  is an  $e, \mu$  or  $\tau$  lepton and the  $W^\pm$  bosons and the  $Z^0$  boson are real particles in the case of a two-body decay and virtual particles in the case of a three-body decay .

The main decay modes for the stau lepton in the pMSSM are

- $\tilde{\tau}^\pm \rightarrow \tilde{\chi}_1^0 \tau$



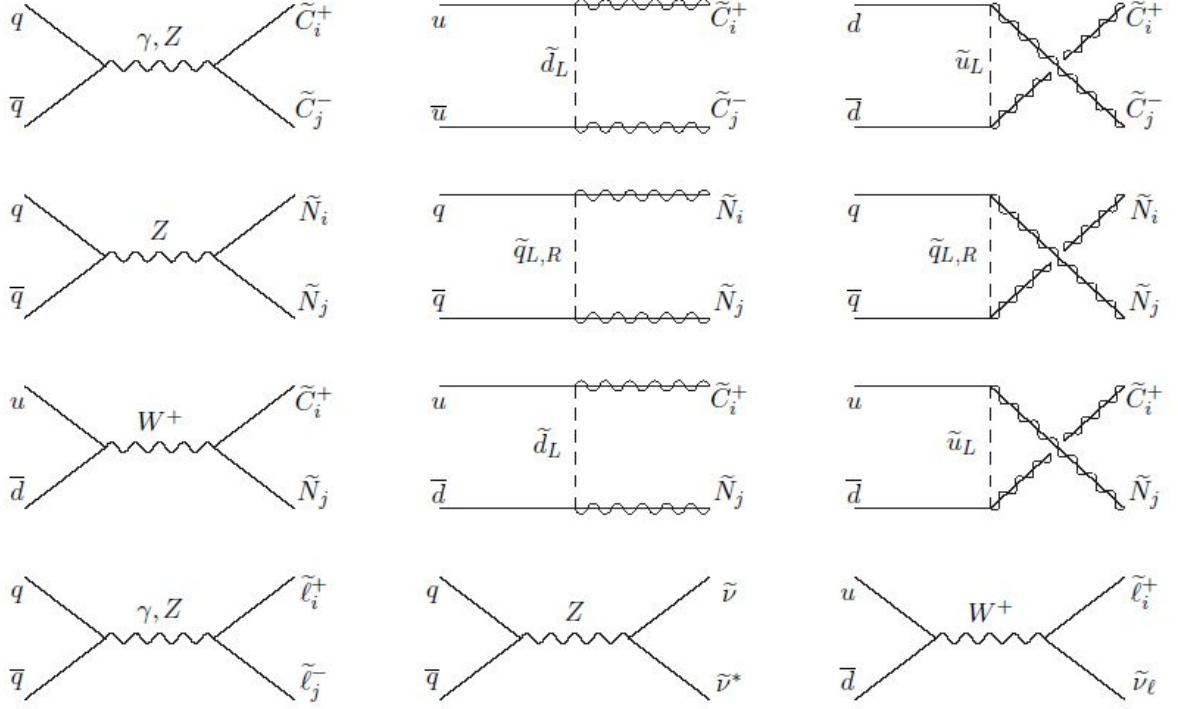


Fig. 2.4: Feynman diagrams for electroweak production of sparticles at hadron colliders from quark antiquark annihilation. Here the notation is slightly changed.  $C^\pm$  denotes a chargino  $\chi^\pm$  and  $N$  a neutralino  $\chi^0$ . [18]

- $\tilde{\tau}^\pm \rightarrow \tilde{\chi}_1^\pm \nu$

The branching fractions for different decay modes of the stau strongly depend on the mass of the stau and the gauginos (most prominently on the mass of the neutralino). Examples of Feynman diagrams that lead to two oppositely charged tau leptons in the final state, as they are studied in this thesis, are shown in Figure 2.5 and Figure 2.6 for gaugino production and decay and in Figure 2.7 for direct stau production and subsequent decay.

The LSP, which is the lightest Neutralino  $\tilde{\chi}_1^0$  in the framework of the pMSSM, is stable in R-parity conserving models and will lead to missing transverse energy at the ATLAS detector.

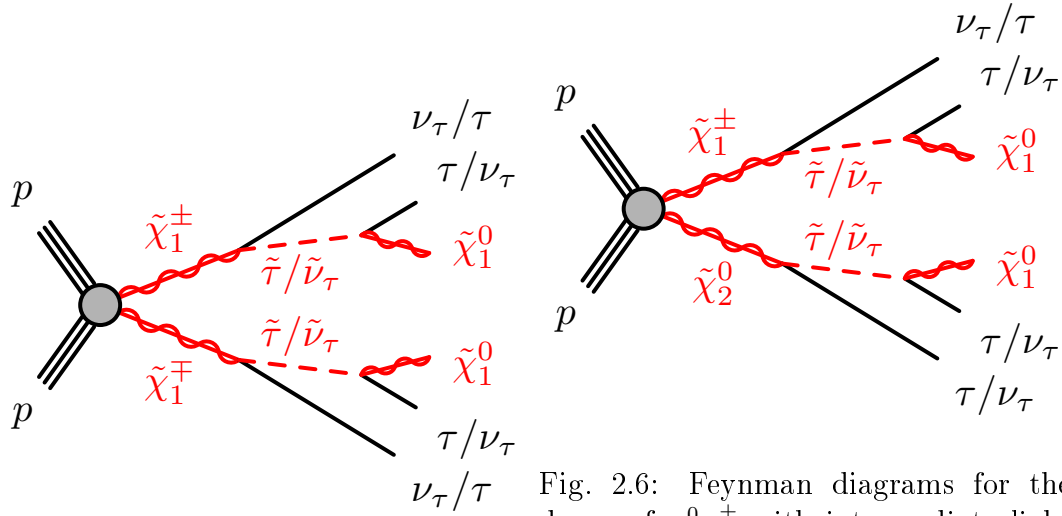


Fig. 2.5: Feynman diagram for the decay of  $\chi_1^\pm\chi_1^\mp$  with intermediate staus and stau-sneutrinos.

Fig. 2.6: Feynman diagrams for the decay of  $\chi_2^0\chi_1^\pm$  with intermediate light staus and stau-sneutrinos. One of the final state staus could be missed because it is not reconstructed or out of the detector acceptance. This would also lead to a final state with exactly two taus.

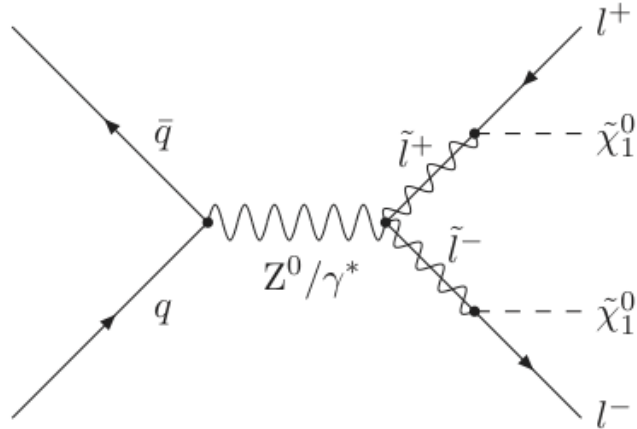


Fig. 2.7: Feynman diagram for direct charged slepton pair production and subsequent decay into a final state with two oppositely charged leptons [24]

---

# CHAPTER 3

## Experimental Setup

### 3.1 The Large Hadron Collider

The information used here on the Large Hadron Collider can be found in [25].

The Large Hadron Collider (LHC) is a synchrotron-type hadron accelerator and collider located at the CERN<sup>1</sup> site near Geneva, Switzerland. Its main goals are to prove or disprove the existence of the Standard Model Higgs boson, which progressed greatly with the discovery of a Higgs-like boson in 2012 by ATLAS [1] and CMS [2], and to discover physics beyond the Standard Model.

The LHC was installed in the existing 26.7 km tunnel, which was constructed for the LEP<sup>2</sup> machine. It is located between 45 m and 170 m below the surface. As the LHC collides protons (or heavy ions), the two particle beams rotate in two separate rings, whereas in a particle-antiparticle collider, such as LEP, both beams can share a single ring.

Protons (or heavy ions) are accelerated through the accelerator complex shown in 3.1 until they are finally transferred into the LHC in bunches and with an energy of 450 GeV. In the LHC the injected bunched beam is captured, accelerated and stored using a 400 Mhz superconducting cavity system that is designed to accelerate the beam up to an energy of 7 TeV, which leads to a centre of mass collision energy of 14 TeV.

Since the first  $p$ - $p$  collisions November 23, 2009 the beam energy has been increased to 3.5 TeV in 2011 and 4 TeV in 2012, as it became apparent after the incident in 2008 that further work is needed before pushing the machine further. After the long shutdown in 2013/14 the LHC is scheduled to reach the design beam energy of 7 TeV.

To keep the protons or ions on their desired path an extensive magnet system is used. More than 1200 main superconducting magnets, cooled below 2 K using superfluid helium, operate with a nominal magnetic field of 8.33 TeV at 7 TeV beam energy. In addition quadrupole and corrector magnets provide stable beams and high luminosity. The four main LHC detectors are located in the caverns at the four interaction points of the LHC. The ALICE<sup>3</sup> detector is designed to study the physics of strongly inter-

---

<sup>1</sup>European Organization for Nuclear Research

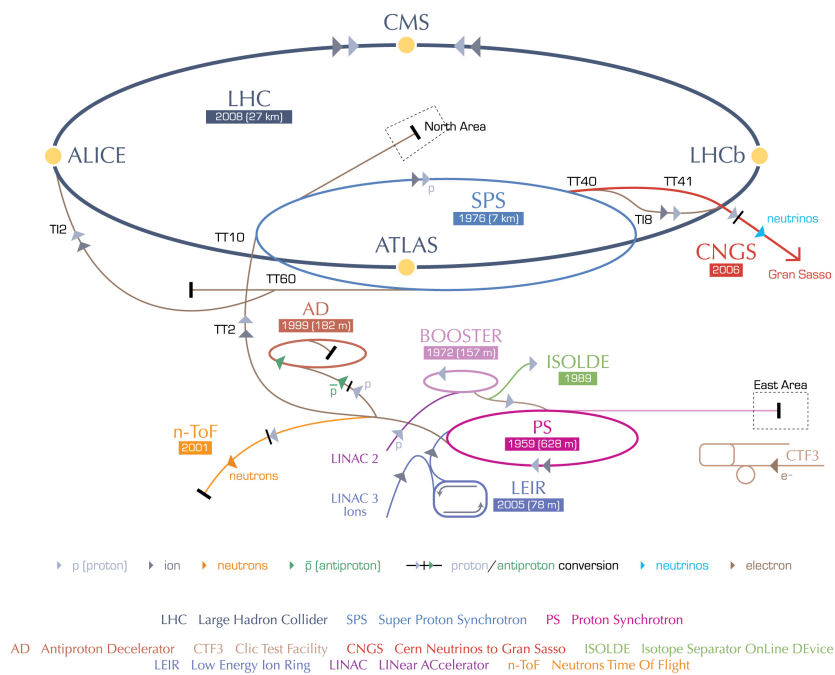
<sup>2</sup>Large Electron Positron Collider

<sup>3</sup>A Large Ion Collider Experiment

acting matter at extreme high energy densities. ATLAS<sup>4</sup> and CMS<sup>5</sup> are two general purpose detectors to investigate a wide range of physics. LHCb<sup>6</sup> is designed to study CP-Violation and rare decays involving bottom (beauty) or charm quarks. Additionally three experiments (LHCf<sup>7</sup>, MoEDAL<sup>8</sup>, TOTEM<sup>9</sup>) are located along the beam line in the vicinity of the main particle detectors.

The LHC is designed to achieve a bunch spacing of 25 ns which corresponds to 2808 bunches for each proton beam. In 2012, with a proton beam energy of 4 TeV, the maximum number of bunches in a beam was 1380 and the maximum average bunch intensity was  $1.66 \cdot 10^{11}$  protons per bunch [26]. The mean number of interactions per crossing was 20.7 [26] and the peak luminosity delivered to ATLAS was  $7.73 \cdot 10^{33} \text{ cm}^{-2}\text{s}^{-1}$ . During 2012 4 TeV the LHC delivered  $23.3 \text{ fb}^{-1}$  to the ATLAS detector.

### CERN's accelerator complex



European Organization for Nuclear Research | Organisation européenne pour la recherche nucléaire

© CERN 2008

Fig. 3.1: The CERN accelerator complex [27]

<sup>4</sup>A Toroidal LHC ApparatuS

<sup>5</sup>Compact Muon Solenoid

<sup>6</sup>Large Hadron Collider beauty

<sup>7</sup>Large Hadron Collider forward experiments

<sup>8</sup>Monopole and Exotics Detector at the LHC

<sup>9</sup>Total elastic and diffractive cross-section measurement experiment

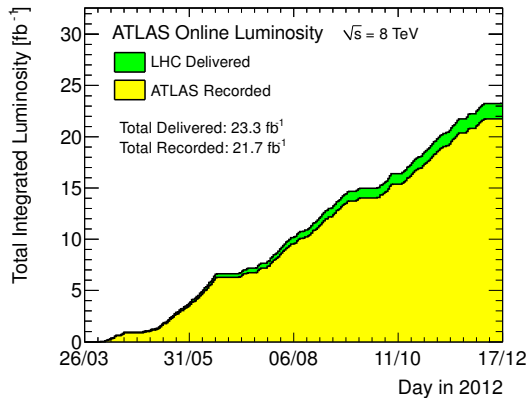


Fig. 3.2: ATLAS integrated luminosity in 2012 [26].

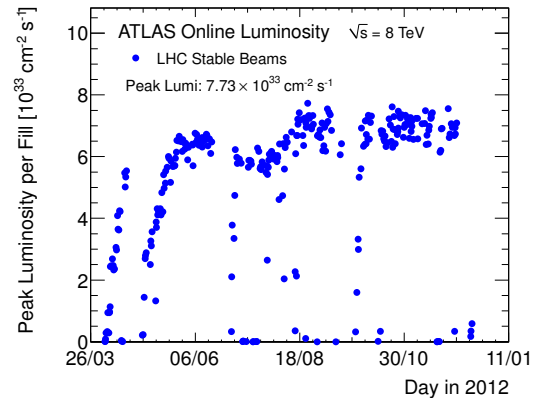


Fig. 3.3: ATLAS peak luminosity in 2012 [26].

## 3.2 The ATLAS detector

The information about the ATLAS detector, its components and the computing infrastructure is mainly taken from the ATLAS Technical Report [28]. Further sources are cited in the text.

The ATLAS detector is one of the two general purpose detectors at the LHC. It is located in a cavern at point 1. It has a length of 46 m, a diameter of 25 m and weighs approximately 7000 tons [29]. The ATLAS collaboration is formed by over 3000 physicists. The ATLAS detector is designed to measure parameters of the Standard Model to a high precision and search for a broad range of physics beyond the Standard Model. Important goals are the searches for supersymmetric particles, heavy W- and Z-like objects, quark compositeness and extra dimensions. In addition CP violation in bottom-quark decays and the top quark properties are studied.

The ability to study such a broad range of physics is expected to maximize the detector's potential for the discovery of physics beyond the Standard Model [30] [28].

One of the main goals of the ATLAS experiment is the search for the Standard Model Higgs boson. Depending on the mass of the Higgs boson, a wide range of production and decay mechanisms are possible and the ATLAS detector was designed to be sensitive in most of them. Since the discovery of a Standard Model Higgs-like boson in 2012, its properties are studied in several decay modes to establish if it is the Higgs boson predicted from the SM or a Higgs Boson of an extension of the Standard Model.

In addition to the physics goals, the experimental conditions at the LHC had to be taken into account in the design of the ATLAS detector. The detector electronics and sensor elements must have fast response time and be radiation hard due to the high radiation environment at the LHC.

The layout of the ATLAS detector is shown in 3.2. Surrounding the beam pipe we find the inner detector 3.2.3. Charged particles are bent by the magnetic field of a thin

superconducting solenoidal magnet placed around the inner detector cavity and are detected in the inner detector.

The electromagnetic calorimeter and the hadronic calorimeter measure the energy of particles.

The outermost muon spectrometer measures the tracks of muons which are bent by the field of the superconducting toroidal magnets.

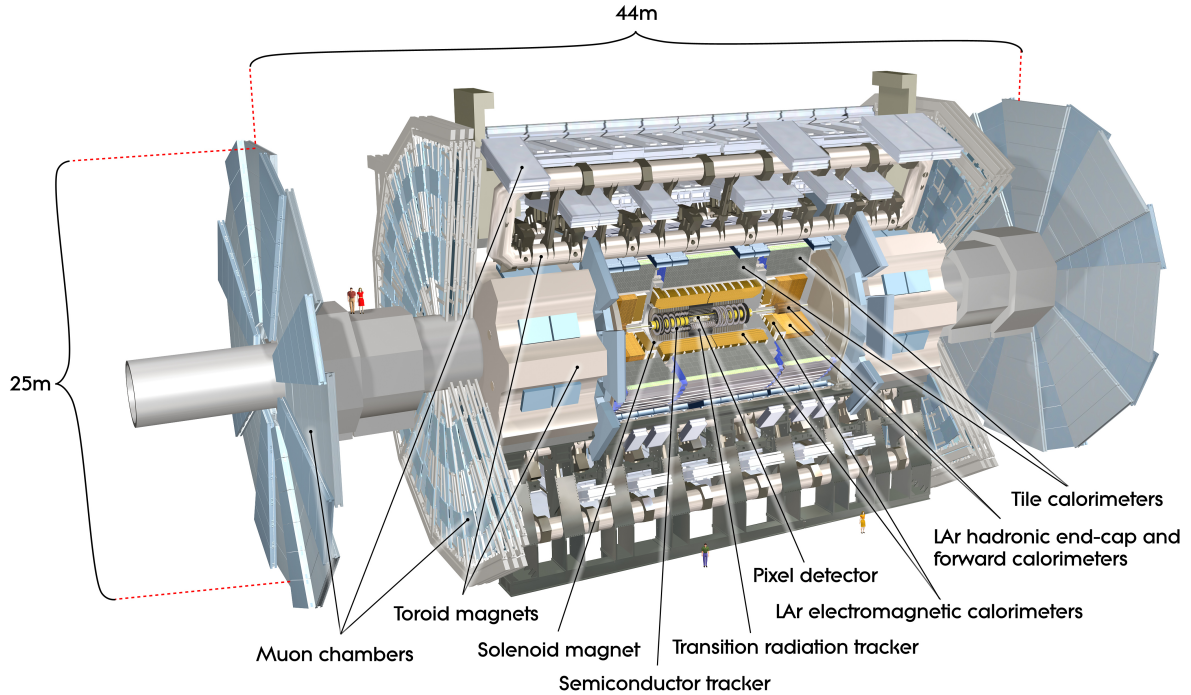


Fig. 3.4: The layout of the ATLAS detector [31]

### 3.2.1 ATLAS coordinate system

With respect to the interaction point, which is defined as the origin of the coordinate system (shown in 3.2.1), the ATLAS detector is forward-backward symmetric. The beam direction defines the  $z$ -axis, the positive  $x$ -axis is defined to point to the center of the LHC ring and the positive  $y$ -axis is pointing upwards.

Variables in the transverse plane, such as the transverse momentum  $p_T$  or the transverse energy  $E_T$ , are defined as projections onto the  $x$ - $y$  plane. The azimuthal angle  $\phi$  is measured around, while the polar angle  $\theta$  is measured from the beam axis.

Two commonly used variables are the pseudorapidity  $\eta$ , which describes the angle of the particle relative to the beam axis,

$$\eta = -\ln \left( \tan \left( \frac{\theta}{2} \right) \right) \quad (3.1)$$

and the distance  $\Delta R$  in the pseudorapidity-azimuthal angle space defined as

$$\Delta R = \sqrt{\Delta\eta^2 + \Delta\phi^2} \quad (3.2)$$

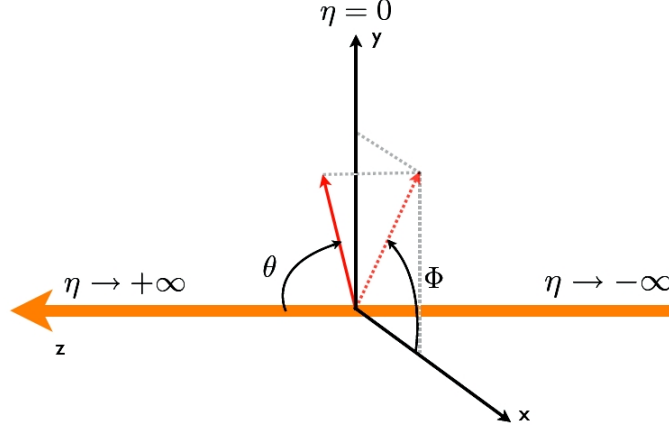


Fig. 3.5: The ATLAS coordinate system[32]

### 3.2.2 Magnet System

The magnet system is an essential part of the ATLAS detector as its magnetic field bends the tracks of charged particles, therefore making the measurement of their momentum possible. Charged particles in a magnetic field are deflected by the Lorentz force which is proportional to the particles speed and the magnetic field strength. Due to the limited size of the toroidal magnets, the magnetic field strength has to be sufficiently high to achieve measurable radii of the particle tracks. On the other hand the interaction of the magnet structure with the particles has to be minimized, resulting in a light and open structure.

The ATLAS magnet system consists of the Central Solenoid (CS) surrounding the inner detector, a toroid system consisting of the Barrel Toroid (BT) and the two End-Cap Toroids (ECT) [33].

Superconducting magnets with aluminium stabilized NbTi/Cu conductors cooled to 4.5 K are used. The central solenoid is 5.3 m long and only 19 cm thin and the resulting magnetif field in the inner dectector is nearly uniform with a field strength of 2 T [33]. The Barrel Toroid and the two End-Cap Toroids consist of 8 coils each, radially and symmetrically located around the beam axis, with magnetic fields of 3.9 T and 4.1 T respectively [33].

The overall size of the magnet system is determined by the Barrel Toroid and End-Cap Toroids. It has a length of 26 m, an outer diameter of 10.7 m and a width of 1.7 m [33].

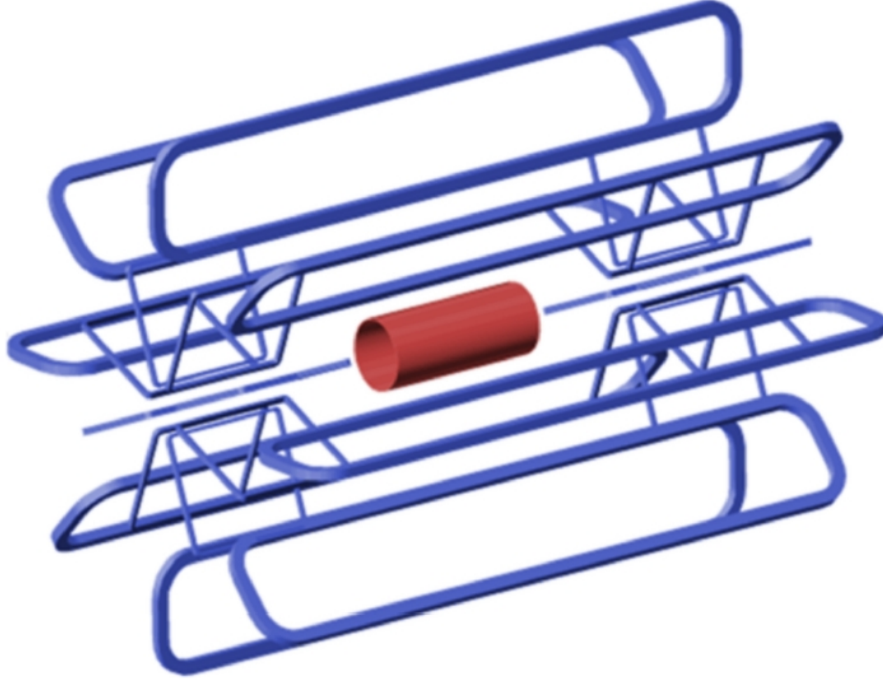


Fig. 3.6: View of the bare windings of the Central Solenoid (red) and of the Barrel and End-Cap Toroids (blue) [33]

### 3.2.3 Inner detector

To provide excellent pattern recognition and measurements of primary and secondary vertices the inner detector (shown in 3.7 and 3.8) is built very close to the beam line at a radial distance of only 50.5 mm and extends to 1082 mm from the center of the beam pipe. It is composed of three independent subdetectors, which are complementary and provide excellent momentum resolution within the pseudorapidity range  $|\eta| < 2.5$  and electron identification within  $|\eta| < 2.0$ . Due to the very high luminosity of the LHC, the spatial and momentum resolution must be very high. This demand is met with the use of discrete space-points from silicon pixel layers and stereo pairs of silicon microstrip layers (SCT) at inner radii. Vertexing for heavy-flavour and  $\tau$ -tagging is also allowed by the Semiconductor Trackers and the Transition Radiation Tracker provides continuous tracking and electron identification.

#### The Pixel Detector

Due to the high particle density close to the interaction point a high spatial resolution of the innermost detector is required to provide primary and secondary vertex measurements and tracking of charged particles. Due to the high particle flux through the detector, its radiation hardness was a major factor that had to be considered when it



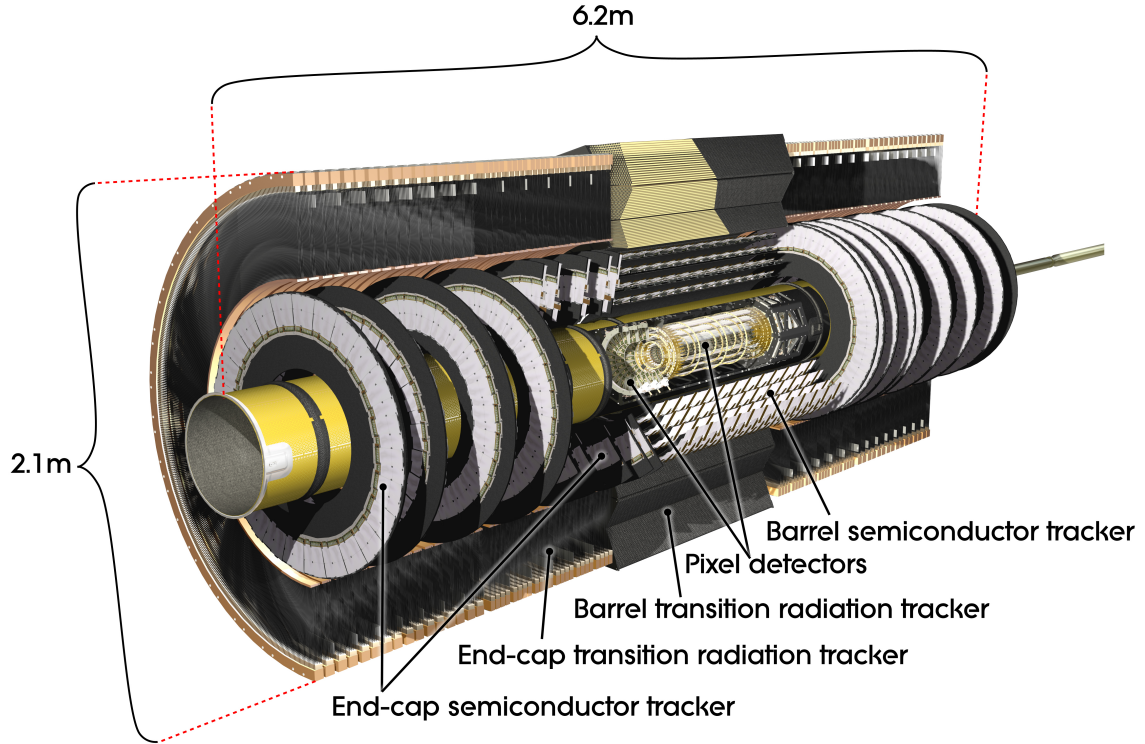


Fig. 3.7: The ATLAS inner detector [31]

was designed. Both of these requirements were matched by silicon pixel sensors.

The 1744 silicon pixel sensors are all identical and are operated at a temperature of  $-10\text{ }^{\circ}\text{C}$  to  $-5\text{ }^{\circ}\text{C}$ . The nominal pixel size is  $50 \times 400\ \mu\text{m}^2$  and there are 47232 pixels on each sensor. The resolution is  $115\ \mu\text{m}$  in  $z$  direction and  $10\ \mu\text{m}$  in the  $(R - \phi)$  plane for the three concentric layers and  $115\ \mu\text{m}$  in  $R$  direction and  $10\ \mu\text{m}$  in the  $(R - \phi)$  plane for the six end cap disks. Due to the high level of radiation the inner pixel vertexing layer has to be replaced after three years of operation at design luminosity.

### The Semiconductor Tracker (SCT)

Due to the factor of cost pixel sensors are not used in every layer of the inner detector. However as the average particle density decreases as the particles move away from the interaction point, the demands on the spatial resolution of the Semiconductor Tracker is not quite as high as for the Pixel Detector.

The Semiconductor Tracker consists of 4088 two-sided silicon modules which cover an area of  $63\text{m}^2$  and are distributed over 4 cylindrical barrels and 18 planar endcaps. Readout strips with a length of 12 cm with a spacing of  $80\ \mu\text{m}$  are placed on the modules. This allows the measurement of the position of the particles with a resolution of  $17\ \mu\text{m}$  in the transverse direction with respect to the strips [29].

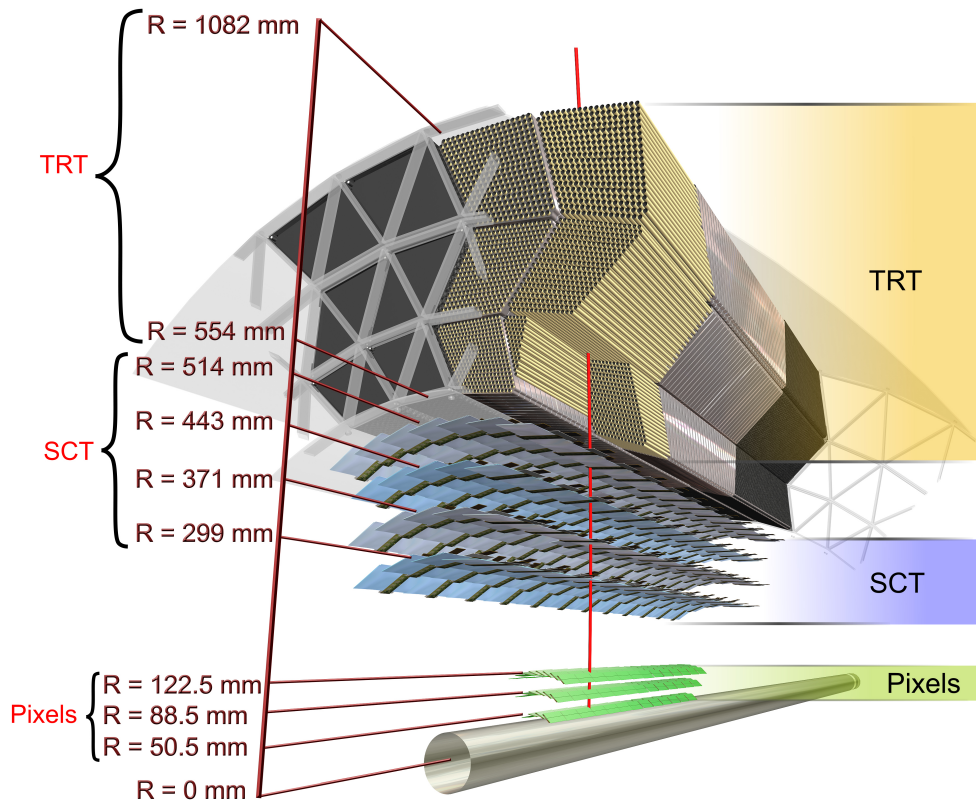


Fig. 3.8: A high energy particle crossing the ATLAS inner detector barrel [31]

### The Transition Radiation Tracker (TRT)

Compared to the Pixel Detector with over 80 Mio and the Semiconductor Tracker with over 6 Mio the Transition Radiation Tracker only has 350k readout channels.

It extends from a radius of 554 mm to a radius of 1082 mm (see Fig. 3.7) and it is composed of several layers of gaseous straw tubes with a diameter of 4 mm interleaved with transition radiation material. The barrel consists of 73 planes of 144 cm long straws arranged parallel to the beam line. The endcaps consist of 160 planes of 37 cm long straws arranged radially in wheels. The TRT provides only  $R - \phi$  information with a resolution of  $130 \mu\text{m}$  per straw.

Even though the single straw resolution is larger than that of the SCT and the Pixel Detector, the TRT contributes significantly to the momentum measurement of the charged particles in the  $|\eta| < 2.0$  region due to the large number of measurements, as the particle hits 36 straws on average, and the long track length that is measured.

Furthermore the TRT provides electron identification complementary to that of the electromagnetic calorimeter as passing electrons produce a large number of transition-radiation photons in the xenon-based gas mixture of the straw tubes.

### 3.2.4 The Electromagnetic Calorimeter

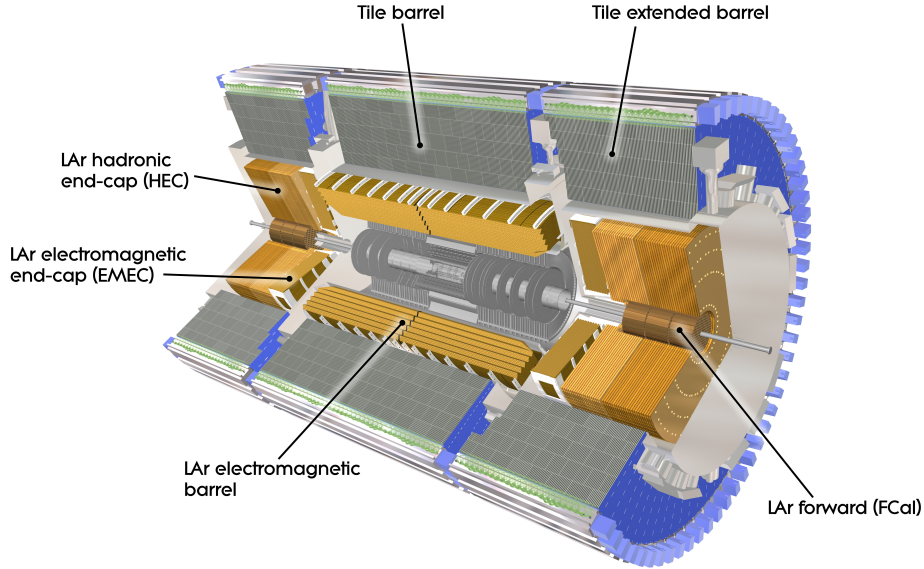


Fig. 3.9: The full ATLAS calorimeter [31]

The Electromagnetic Calorimeter (shown as part of the full ATLAS calorimeter in Fig. 3.2.4) is mainly used to measure the energy of electrons and photons. Many layers of lead and steel form an accordion structure. A copper electrode, immersed in liquid Argon cooled to  $-185\text{ }^\circ\text{C}$ , is placed between the lead and steel particle absorbers. As it enters the calorimeter an electron or a photon interacts with the absorbers and a shower of low energy particles, such as electrons, positrons and photons, is produced. The low energy particles ionize the liquid argon and the free electrons are collected by the electrode. The energy of the original high energy electron or photon can be determined from the amount of charge collected.

The calorimeter system has electromagnetic coverage in the range of  $|\eta| < 4.9$  together with the Forward Calorimeter. Presamplers complement the electromagnetic calorimeters over the full ECal  $\eta$  region and provide a measurement of the energy lost in front of the calorimeters.

The relative energy resolution of the Electromagnetic Calorimeter is parametrized by  $\frac{\sigma_E}{E} = \frac{10\%}{\sqrt{E}} \oplus \frac{170\text{ MeV}}{E} \oplus 0.7\%$  [34].

### 3.2.5 The Hadronic Calorimeter

The energy of hadrons is measured by the Hadronic Calorimeter (shown as part of the full ATLAS calorimeter in Fig. 3.2.4). The barrel and extended barrels cover the region  $|\eta| < 1.7$  and extend from 2.3 m to a radius of 4.3 m. Hadrons pass through an array of interleaved steel and scintillator sheets. Due to the interaction with steel a particle shower of low energy particles is produced. The shower transverses the scintillator and causes it to radiate light. The light is collected by wavelength-shifting fibres that carry it to photomultipliers, where the light intensity is converted into an electric current. As the readout is done in three different layers, the shower can be tracked up to a certain extent.

The endcaps of the Hadronic Calorimeter cover the region  $1.5 < |\eta| < 3.2$  and use as in the Electromagnetic Calorimeter, liquid Argon is used as the active material but copper is used instead of lead as the absorber material.

The thickness of the Hadronic Calorimeter is approximately 9.7 interaction lengths in the barrel (10 in the end-caps). Such a thickness ensures good resolution for high energy jets. Furthermore the total thickness of 11 interaction lengths (including also the outer support) limits punch-through well below the irreducible level of prompt or decay muons. This thickness offers, together with the large  $\eta$  coverage, a good MET measurement which is important in particular for SUSY searches.

### 3.2.6 Muon Spectrometer

The outermost component of the ATLAS Detector is the Muon Spectrometer (shown in Fig. 3.2.6). In the barrel region ( $|\eta| < 1.4$ ) the Muon Spectrometer chambers are installed in three cylindrical layers at 5, 7.5 and 10 m from the beam axis. In the transition ( $1.4 < |\eta| < 1.6$ ) and in the end-cap region ( $1.6 < |\eta| < 2.7$ ) the chambers are arranged in planes perpendicular to the beam line. The Muon Spectrometer consists of four subsystems:

- Monitored Drift Tube Chambers (MDT's),
- Cathode-Strip Chambers (CSC's),
- Resistive Plate Chambers (RPC's),
- Thin Gap Chambers (TGC's).

The MDT and CSC provide, together with the inner detector, precise muon tracking. The RPC and TGC are fast trigger chambers capable of transmitting track information within a few tens of nanoseconds after the passage of a particle. In the muon chambers the muons are bent by the magnetic field of the large superconducting air-core toroid magnets.

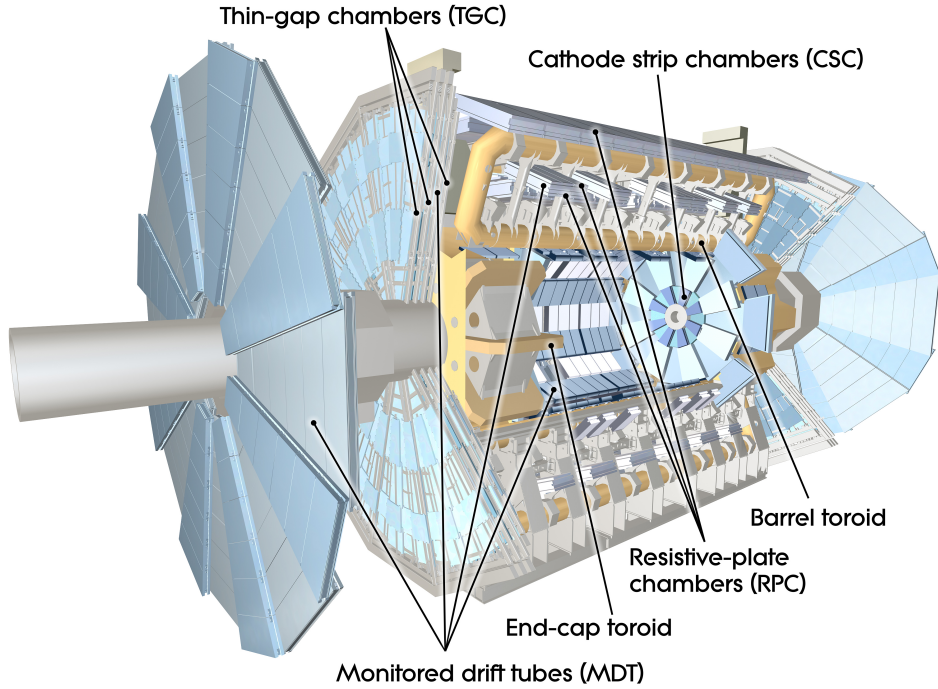


Fig. 3.10: Overview of the ATLAS Muon Spectrometer components [31]

### Monitored Drift Tube Chamber (MDT)

The Monitored Drift Tube Chambers cover the pseudorapidity range  $|\eta| < 2.7$  (in the innermost end-cap layer it is limited to  $|\eta| < 2.0$  (see Section 3.2.6)) and are located between and on the eight coils of the superconducting barrel toroid magnet. The chambers have 3 to 8 layers of drift tubes that are filled with a  $Ar/CO_2/H_2O$  (93/7/ < 1000ppm) gas mixture at a pressure of 3 bar. In the center of each tube a tungsten-rhenium wire with a diameter of  $50 \mu\text{m}$  at a potential of 3080 V acts as an anode. A passing muon ionizes the atoms in the gas mixture and the resulting free electrons are collected at the cathode. The minimal radial distance from the wire, which is placed tangentially to a circle around the beam axis, is measured. This corresponds to a precise measurement of the  $\eta$  coordinate. The average resolution per tube is  $80 \mu\text{m}$  [35] and depends only weakly on the angle of incidence of the track onto the chamber plane due to the radial electric field configuration. The sagitta of a track crossing three MDT chambers is expected to be measured with a resolution of  $\Delta S = 45 \mu\text{m}$  which corresponds to a momentum resolution of  $\frac{\delta p}{p} = \Delta S \times \frac{p}{500 \mu\text{m}}$ , where  $p$  is in units of TeV [36].

### Cathode-Strip Chamber (CSC)

Instead of MDT's, 32 (16 on either side) CSC's are used in the forward region in the innermost layer ( $2 < |\eta| < 2.7$ ) due to their ability to cope with counting rates up to

1000 Hz/cm<sup>2</sup> and their excellent time resolution of 7 ns per plane [36]. The CSC's are multiwire proportional chambers. The wires are oriented parallel to the central wire which points in the radial direction. The CSC's use, just as the MDT's, an Ar/CO<sub>2</sub> gas mixture but the cathodes are segmented and the CSC's are able to measure two coordinates. The strips perpendicular to the wires provide a measurement of  $\eta$  and the strips parallel to the wires provide a measurement of  $\phi$ . The CSC reaches a resolution of approximately 60  $\mu\text{m}$  as the resolution depends heavily on the read-out pitch [36].

## Resistive Plate Chamber (RPC)

The RPC's cover the barrel region  $|\eta| < 1.05$  and are arranged as three concentric cylindrical trigger stations around the beam axis with two independent detector layers each (see Fig. 3.11). In the picture, RPC3 provides the trigger for high momentum tracks in the range 9-35 GeV while the two inner chambers RPC1 and 2 provide the low  $p_T$  trigger (6-9 GeV) [36]. The RPC is a gaseous parallel electrode-plate detector with a 2 mm thick active gas volume. An electric field with a field strength of 4.9 kV/mm is applied between the two plates. Both the  $\eta$  and the  $\phi$  coordinates are measured. Therefore the RPC's (and also the TGC's) complement the MDT measurement with the second coordinate as the measurement is matched to the measurement made by the MDT's via  $\eta$ . The RPC detector reaches a time resolution of about 2 ns for the whole experiment [37].

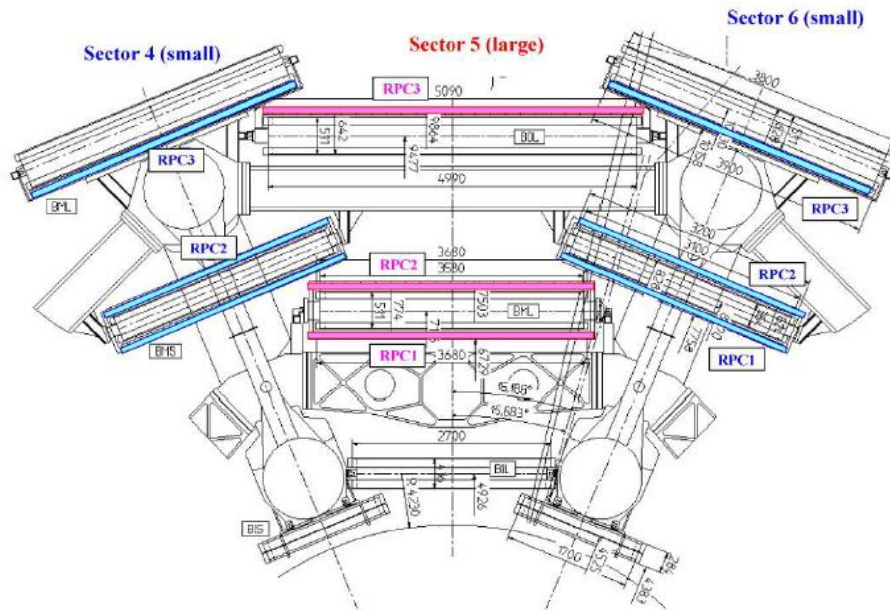


Fig. 3.11: Layout of the standard RPC Chamber [36]

## Thin Gap Chamber (TGC)

TGC's are multi-wire proportional chambers and provide good time resolution and high rate capability. They cover the end-cap region ( $1.05 < |\eta| < 2.4$ ). They provide a muon trigger and complement the MDT measurements with a measurement of the second coordinate ( $\phi$ ). The TGC's are arranged in four layers with the three last layers being used to generate the trigger information by a system of fast coincidences.

### 3.2.7 Forward Detectors

Three forward detector pairs complement the measurements made by the inner detector, the calorimeters and the Muon Spectrometer. Closest to the interaction point LUCID<sup>10</sup> is installed at a distance of  $\pm 17$  m.

At a distance of  $\pm 140$  m from the interaction point, where the LHC beam pipe is divided into two separate pipes, the ZDC<sup>11</sup> is installed.

The third pair of forward detectors, located in Roman pots  $\pm 240$  m from the interaction point, are the ALFA<sup>12</sup> detectors.

## LUCID

LUCID consists of twenty 1.5 m long aluminium tubes, with a diameter of 15 mm, surrounding the beam pipe and arranged to point to the interaction point. The tubes are filled with  $C_4F_{10}$  at a pressure of 1.2-1.4 bar. When a particle transverses through a tube it emits Cerenkov light that is measured by PMT's<sup>13</sup>. The number of particles per tube can be distinguished from the signal amplitude. Its main purpose is to measure the integrated luminosity and monitor the instantaneous luminosity and beam conditions at ATLAS.

## ZDC

The ZDC's primarily detect forward neutral particles with  $|\eta| > 8.3$  in heavy ion and p-p collisions. Its main purpose is the event characterization of heavy ion collisions. They also enhance the acceptance of ATLAS central and forward detectors for diffractive processes and to provide an additional minimum-bias trigger for ATLAS [38].

---

<sup>10</sup>LUMinosity measurement using Cerenkov Integrating Detector

<sup>11</sup>Zero-Degree Calorimeter

<sup>12</sup>Absolute Luminosity For ATLAS

<sup>13</sup>Photomultiplier tubes

## ALFA

The ALFA detector system measures elastic  $p$ - $p$  scattering under angles as small as  $3\ \mu\text{rad}$  which offers a calibration of the absolute luminosity. To achieve measurements at such small angles the detectors are placed in Roman pots that can be brought as close as 1 mm to the beam at a distance of  $\pm 240\text{ m}$  to the interaction point. These measurements are carried out during dedicated runs with high beta optics. [39]

### 3.2.8 Trigger and Data Acquisition

In 2012 the LHC provided a crossing rate of 20 MHz and the mean number of interactions per crossing was 20.7. To reduce the rate, at which data has to be recorded, to  $\approx 400\text{ Hz}$  a trigger system is installed. It consists of the hardware based L1 trigger, the software based L2 trigger and the event filter. The ATLAS trigger and Data Acquisition System is shown schematically in 3.2.8.

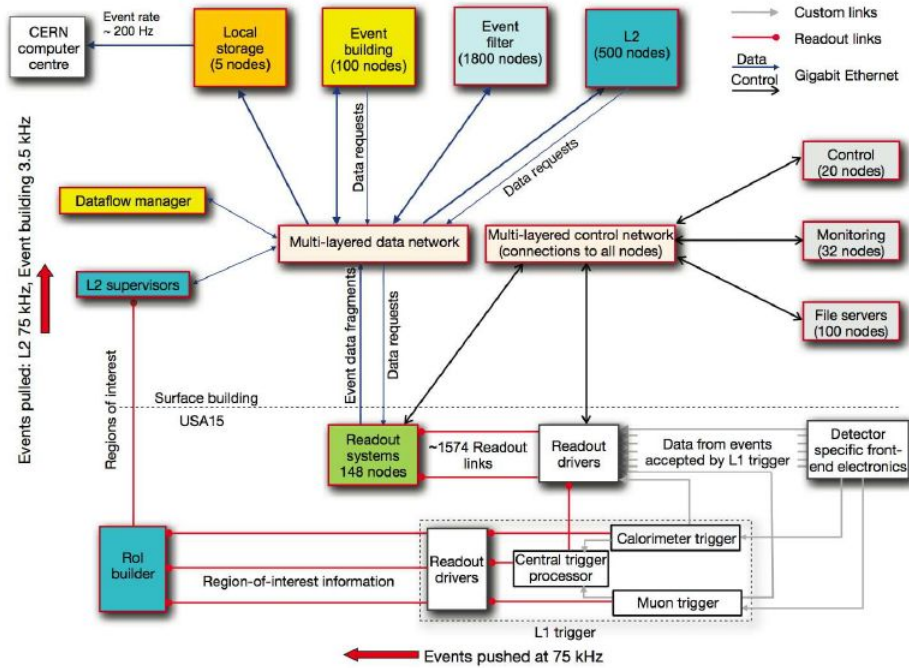


Fig. 3.12: Diagram of the ATLAS trigger and Data Acquisition System [28]

#### Level 1 Trigger

The L1 trigger performs the initial event selection based on the information from all the calorimeter subsystems and the RPC and TGC detectors of the Muon Spectrometer. The trigger selects events with large  $E_T^{miss}$ , high- $p_T$  muons, electrons/photons, jets and



$\tau$ -leptons decaying into hadrons. It also selects Regions-of-Interest (ROI's) of the detector which are used by the L2 trigger to perform a further selection of events. The L1 trigger decision reaches the front-end electronics within  $2.5 \mu\text{s}$  after the bunch crossing. The L1 trigger is implemented as a system of purpose-built hardware processors.

## Level 2 Trigger

The L2 trigger receives information from the Data Acquisition System based on the ROI's where the L1 trigger has identified possible trigger objects. This limits the amount of data which has to be transferred from the detector readout. Event building is performed for the events that fulfill the L2 selection criteria. The L2 trigger reduces the event rate below 3.5 kHz and it has an average processing time of 40 ms per event.

## Event Filter

The Event Filter receives the fully assembled events which passed the L1 and L2 selection criteria and uses standard ATLAS event reconstruction to further select events. The Event Filter also classifies the events according to the ATLAS physics streams. The average processing time is of the order of 4 seconds and the event rate is reduced to 400 Hz at which data is recorded for offline analysis.

## 3.2.9 Computing Infrastructure

The computing infrastructure of ATLAS is decentralised as it is not a feasible option to store and process the huge amount of data produced at ATLAS in a central computing centre at the CERN site. For this purpose the Worldwide LHC Computing Grid (WLCG) [40] was launched in 2002. It is organized in four levels, called Tiers. The Tier-0 facility at CERN receives RAW data from the Event Filter and distributes it after a first event processing to the Tier-1 centers. Eleven Tier-1 sites reprocess the data and provide long term access to RAW and derived datasets. Tier-2 facilities also host datasets (AOD, TAG, DPD) and provide analysis capacity. Furthermore they process all the simulation jobs for the experiment. Tier-3's are small computing clusters down to desktop computers that store end user data and provide access to the Grid resources. Users can send analysis jobs to the centres that store the data via a Grid User Interface such as Ganga [41].

---

# CHAPTER 4

## Analysis

In this chapter the event selection together with the definition of the physics objects is described. The object definitions, the Overlap Removal and ‘Event Quality’ criteria are the same for both studies presented in this thesis and were adopted from the analysis described in [24]. However it has to be noted that the studies on the pMSSM grid with direct gaugino and direct slepton production are carried out at Truth level.

### 4.1 Object Definitions

When describing the object definitions we distinguish between ‘baseline’ objects, which are input to the Overlap Removal, and ‘signal’ objects which have passed the Overlap Removal and fulfill further stringent requirements. A summary of the object definitions is given in Table 4.1.

#### 4.1.1 Jets

The anti- $k_T$  jet algorithm [42] with a distance parameter  $R = 0.4$  and topological clusters [43] as input is used to reconstruct jets. The Local Hadron Calibration [44], which distinguishes between electromagnetic and hadronic clusters, calibrates the jet energies. It corrects for the non-compensating nature of the calorimeter, before jet reconstruction is started and final jet-level energy calibrations are applied (LC+JES calibration). As input to the Overlap Removal baseline jets must have  $p_T > 20$  GeV and  $|\eta| < 4.5$ . To pass the Overlap Removal, jet clusters are only counted as jets if they do not overlap with either electrons or taus within  $\Delta R < 0.2$ . Furthermore jets are required to pass loose quality selection to reject jets which are not associated with real energy deposits in the calorimeter. These are jets from non-collision background events and cosmic-ray showers or calorimeter noise.

Signal jets have to fulfill further requirements, such as requirements on the jet vertex fraction (JVF) and b-tagging. The JVF gives a probability that a jet originated from a particular vertex. The discriminant is computed from all charged tracks of a jet that point to a primary vertex in the event. To identify jets originating from a hard scattering vertex and to reject jets from additional soft scattering (pile-up) vertices a

JVF greater than 0.2 is required, which was found to be the optimum point [45]. B-tagging is achieved with the MV1 tagging algorithm which is based on a neural network. It receives the output weights of the JetFitter+IP3D, IP3D and SV1 algorithms as input [46]. A jet must satisfy the 85% working point of the MV1 algorithm,  $MV1 > 0.122$ , to be tagged as a b-jet. As the inner detector only provides tracking in the region  $|\eta| < 2.5$  the JVf and b-tagging cannot be computed in the forward region  $|\eta| > 2.5$ . Therefore a higher  $p_T$ -threshold of  $> 30$  GeV is needed to suppress the contribution from pileup jets in the forward region.

Signal jets are classified in three exclusive categories: central light jets, central b-jets and forward jets.

- Central light jets (L25):  $p_T > 25$  GeV,  $|\eta| < 2.5$ ,  $JVF > 0.2$ ,  $MV1 < 0.122$  (no b-tag)
- Central b-jets (B20):  $p_T > 20$  GeV,  $|\eta| < 2.5$ ,  $MV1 > 0.122$  (b-tag)
- Forward jets (F30):  $p_T > 30$  GeV,  $2.5 < \eta < 4.5$

### 4.1.2 Taus

In general only hadronically decaying taus are considered as it is difficult to distinguish leptonically decaying taus from primary electrons or muons.

Jets with  $p_T > 10$  GeV and  $|\eta| < 2.5$  that were reconstructed with the anti- $k_T$  algorithm seed the tau reconstruction algorithm. Furthermore only tracks that can be associated with a tau cluster within a cone of  $\Delta R < 0.2$  around the axis of the seed jet are considered. Tau clusters are topological clusters in the electromagnetic and hadronic calorimeters [47]. Furthermore a correction of the reconstructed energy of the hadronic taus to the tau energy scale is necessary as the tau energy scale is calibrated independent of the jet energy scale by a Monte Carlo based procedure [48].

Baseline taus have  $p_T > 20$  GeV and  $|\eta| < 2.5$ , excluding the transition region between the electromagnetic barrel and the electromagnetic end-cap calorimeter ( $1.37 < |\eta| < 1.52$ ). Furthermore taus need to have 1 or 3 tracks (prongs) associated to them and the total charge of a track has to be  $\pm 1$ . This covers the most probable hadronic decays of tau leptons to either one or three charged pions and a neutrino.

To improve the discrimination between hadronically decaying taus and jets, electrons and muons a Boosted Decision Tree (BDT) method is used. Baseline taus need to pass the ‘medium’ selection criteria. This means that fake tau candidates are rejected with a signal efficiency of 50% (55%) for 1-prong (3-prong) tau candidates for the discrimination from jets, and a 85% signal efficiency for the discrimination from electrons [49]. Also a muon veto is applied to reject tau candidates from muons coinciding with anomalous energy deposits in the calorimeter.

In this analysis exactly two hadronically decaying taus are selected where one of the taus has to pass the ‘tight’ BDT identification which corresponds to a signal efficiency

of 30% (35%) for 1-prong (3-prong) candidates for the discrimination from jets and 75% signal efficiency for the discrimination from electrons [49].

### 4.1.3 Electrons

Electrons are detected as electromagnetic clusters in the Electromagnetic Calorimeter and leave tracks in the inner detector. The tracks and clusters are matched and depending on the number of hits on the electron track either the  $\eta$  and  $\phi$  from the inner detector track or from the electromagnetic cluster are used for the position variables of the electron. The  $p_T$  of the electron is defined as  $E_{cluster}/\cosh(\eta)$ . Baseline electrons which pass the requirements of  $p_T > 10$  GeV,  $|\eta| < 2.47$  and 'medium++' identification criteria, are then used as input to the Overlap Removal (described in 4.2). Baseline electrons that have passed the Overlap Removal are used to veto events in this analysis (light lepton veto).

### 4.1.4 Muons

Muons leave tracks in the Muon Spectrometer and the Inner Detector. They are reconstructed with the STACO algorithm which combines the tracks in both detector subsystems. In this analysis two kinds of reconstructed muons are used: "Combined" muons are formed from tracks that have been reconstructed independently in both the Muon Spectrometer and the Inner Detector. For the reconstruction of "Segment-tagged" muons, information from the Muon Spectrometer is only used to tag the tracks in the inner detector. The requirements on the number of hits for baseline muons are at least one hit in the pixel detector and hits in at least 5 layers of the Transition Radiation Tracker. In addition the  $p_T$  measurement of the Muon Spectrometer and the of the Inner Detector must be compatible. Also they need to fulfill  $p_T > 10$  GeV and  $|\eta| < 2.4$ . Together with electrons they are used to veto events in this analysis (light lepton veto). Muons from cosmic radiation, called "Cosmic Muons", are rejected via tight requirements on the longitudinal  $|z_0^{PV}| < 1.0$  mm and transverse impact parameter  $|d_0^{PV}| < 0.2$  mm, which are both measured with respect to the reconstructed primary vertex.

### 4.1.5 Missing Transverse Energy

The energy deposition in the calorimeter cells calibrated according to the physics objects to which they are associated, is used by the MET reconstruction algorithm. Also cells that are not associated to any object are included and weighted to take pile-up effects into account.

<b>Taus</b>				
	Baseline	Signal		
Cut	Value/Description	Value/Description		
algorithm	cluster seeded	cluster seeded		
$p_T$	$p_T > 20 \text{ GeV}$	$p_T > 20 \text{ GeV}$		
$\eta$ -acceptance	$ \eta  < 2.5$ , excl. $1.37 <  \eta  < 1.52$	$ \eta  < 2.5$ , excl. $1.37 <  \eta  < 1.52$		
n-prongs	n-prongs=1 or 3	n-prongs=1 or 3		
charge	$ q  = 1$	$ q  = 1$		
quality	medium	medium + at least 1 tight tau		
<b>Electrons</b>				
	Baseline	Signal		
Cut	Value/Description	Value/Description		
algorithm	egamma	not defined		
$p_T$	$p_T > 10 \text{ GeV}$			
$\eta$ -acceptance	$ \eta  < 2.47$			
quality	medium++			
<b>Muons</b>				
	Baseline	Signal		
Cut	Value/Description	Value/Description		
algorithm	STACO	not defined		
$p_T$	$p_T > 10 \text{ GeV}$			
$\eta$ -acceptance	$ \eta  < 2.4$			
isolation	-			
tracking cuts	various			
<b>Jets</b>				
	Baseline	Signal		
		L25	B20	F30
Cut	Value/Description	Value/Description		
algorithm	anti- $k_T$ ( $R = 0.4$ )	anti- $k_T$ ( $R = 0.4$ )		
$p_T$	$p_T > 20 \text{ GeV}$	$> 25 \text{ GeV}$	$> 20 \text{ GeV}$	$> 30 \text{ GeV}$
$\eta$ -acceptance	$ \eta  < 4.5$	$ \eta  < 2.5$	$ \eta  < 2.5$	$ \eta  > 2.5$ , $ \eta  < 4.5$
JVF	-	$JVF > 0.2$	-	-
b-tag	-	$MV1 < 0.122$	$MV1 > 0.122$	-

Table 4.1: All baseline and signal object selection criteria

## 4.2 Overlap Removal

The Overlap Removal procedure is needed to avoid the duplication of one particular object into two or more signal physics objects. The following 12 steps are applied consecutively and jets are considered before the application of loose quality criteria for the rejection of fake and non-collisional energy deposits. Steps 1-8 consider the overlap between light leptons and jets and steps 9-12 consider the overlap with tau leptons. Low mass resonances in the spectrum of the baseline leptons are removed in the steps 7,8 and 12.

1.  $\Delta R(e_1, e_2) \geq 0.1$ : If any two baseline electrons ( $e_1$  and  $e_2$ ) lie within a distance  $\Delta R < 0.1$  of each other, the electron with the lower cluster energy  $E_T$  is rejected.
2.  $\Delta R(e, j) \geq 0.2$ : If the distance between a baseline electron ( $e$ ) and a jet ( $j$ ) is smaller than 0.2 the jet is rejected.
3.  $\Delta R(j, e) \geq 0.4$ : If the distance between a remaining jet ( $j$ ) and a baseline electron ( $e$ ) is smaller than 0.4 the baseline electron is rejected.
4.  $\Delta R(j, \mu) \geq 0.4$ : If the distance between a jet ( $j$ ) and a baseline muon ( $\mu$ ) is less than 0.4 the baseline muon is rejected.
5.  $\Delta R(e, \mu) \geq 0.1$ : If a baseline electron and a baseline muon lie within a distance of  $R < 0.1$  both the electron and the muon are rejected.
6.  $\Delta R(\mu_1, \mu_2) \geq 0.05$ : If any two baseline muons ( $\mu_1$  and  $\mu_2$ ) lie within a distance of  $R < 0.05$  both muons are rejected.
7.  $\Delta m(e_1^\pm, e_2^\mp) \geq 12 \text{ GeV}$ : If the invariant mass of any baseline electron pair with opposite sign ( $e_1^\pm$  and  $e_2^\mp$ ) is less than 12 GeV both electrons are rejected.
8.  $\Delta m(\mu_1^\pm, \mu_2^\mp) \geq 12 \text{ GeV}$ : If the invariant mass of any baseline muon pair with opposite sign ( $\mu_1^\pm$  and  $\mu_2^\mp$ ) is less than 12 GeV both muons are rejected.
9.  $\Delta R(e, \tau) \geq 0.2$ : If the distance between a baseline electron ( $e$ ) and a baseline tau ( $\tau$ ) is smaller than 0.2 the tau-lepton is rejected.
10.  $\Delta R(\mu, \tau) \geq 0.2$ : If the distance between a baseline muon ( $\mu$ ) and a baseline tau ( $\tau$ ) is less than 0.2 the baseline tau-lepton is rejected.
11.  $\Delta R(j, \tau) \geq 0.2$ : If the distance between a baseline tau ( $\tau$ ) and a jet ( $j$ ) is smaller than 0.2 the jet is rejected.
12.  $\Delta m(\tau_1^\pm, \tau_2^\mp) \geq 12 \text{ GeV}$ : If the invariant mass of any baseline tau pair with opposite sign ( $\tau_1^\pm$  and  $\tau_2^\mp$ ) is less than 12 GeV both taus are rejected.

### 4.3 Event Quality Criteria

In this analysis events which contain exactly two hadronically decaying taus with opposite sign (Signal Region) or same sign (estimation of QCD background) are selected. Events are selected based on 'event quality' requirements which are summarized in table 4.2.

Cut	Description
GRL	Events in data must pass requirements on data quality
Incomplete TTC Veto	Events in data must not be incomplete as a result of a TTC restart for detector recovery during data-taking
LAr&Tile Error	Events in data must report no error after LAr and Tile quality assessment
Tile Hot Spot Veto	During data-taking period B1-B2, no jet pointing to a particularly noisy region in the tile calorimeter must be present in the event
Jet Cleaning	Events must not contain a jet which failed the jet quality selection
Primary Vertex	The primary vertex in the event must be associated with at least 5 tracks
Bad Muon Veto	Events must not have one or more muons failing the bad muon criteria
Cosmic Muon Veto	All muons in the event must pass the cosmic muon rejection cuts

Table 4.2: Summary of 'Event quality' criteria

### 4.4 Trigger Selection

In this analysis a combination of a di-tau trigger and a trigger on  $E_T^{miss}$  is used (Table 4.3). The trigger decisions are taken during data-taking. Therefore the trigger objects are not reconstructed using the full detector information and sophisticated reconstruction algorithms. The reconstructed objects used in this thesis have higher resolution than the trigger objects on which the trigger algorithms are based. As a result the efficiency dependence as a function of the reconstructed  $p_T$  is not an exact step-function, but the trigger efficiency rises slowly from 0 to the plateau (defined as the region in which the trigger efficiency is maximal and constant) as shown exemplarily in Fig 4.1. The region in which the trigger efficiency is not constant is called the turn-on region.

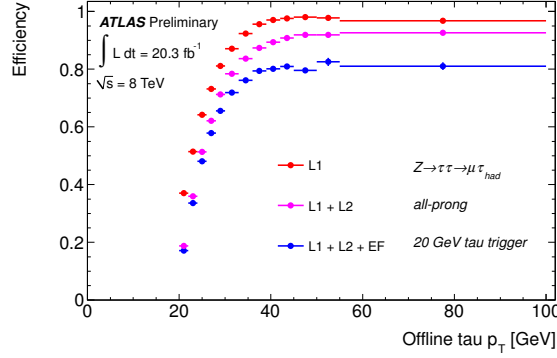


Fig. 4.1: Single tau trigger efficiency as a function of the offline tau transverse momentum. The tau trigger considered here has calorimetric isolation and a  $p_T$  threshold of 11 GeV at L1, a 20 GeV requirement on  $p_T$ , the number of tracks restricted to three or less, and medium selection on the BDT score at the EF. [26]

The efficiencies of the di-tau and the  $E_T^{miss}$  have been studied by members of the group. The di-tau trigger reaches its efficiency plateau with an efficiency of 65 % [24] when the leading tau has  $p_T > 40$  GeV and the next-to-leading tau has  $p_T > 25$  GeV [24]. The plateau region of the  $E_T^{miss}$  trigger is above 150 GeV [24]. It is fully efficient in the plateau region [24].

A logical OR is applied to the two triggers and additionally events have to fulfill an OR of the offline  $p_T$  and MET thresholds listed in Table 4.3 to only select events in the plateau region.

Trigger object	Trigger item	Online $p_T$ /MET thresholds
2 taus	EF_tau29Ti_medium1_tau20Ti_medium1	$p_T^{leading} > 40$ GeV, $p_T^{subleading} > 25$ GeV
MET	EF_xe80_tclw	MET > 150 GeV

Table 4.3: Triggers used in the analysis



---

## CHAPTER 5

# Search for direct stau production

An analysis for the search for direct stau production in  $p$ - $p$  collisions at  $\sqrt{s} = 8$  TeV is presented.

In this chapter the Standard Model background and the selection cuts applied to the variables of interest are discussed. A signal region is developed and the sensitivity of the analysis is determined using a hypothesis test and the computation of a lower limit on the cross-section that can be excluded with this analysis.

## 5.1 Direct stau production

The Feynman diagram for direct stau production in  $p$ - $p$  collisions is shown in Figure 2.7. The final state consists of two oppositely charged taus and two neutralinos.

Therefore this analysis requires exactly two hadronically decaying taus (referred to as hadronic taus) with opposite sign (OS) in the final state while events with additional light leptons (electrons, muons) in the final state are rejected (light lepton veto). The region characterized by these selection criteria will be referred to as the OS region.

The lightest neutralino  $\tilde{\chi}_0$  is stable in the pMSSM and, as it does not interact with the detector, the two neutralinos in the final state lead to large  $E_T^{miss}$ . Also the tau-neutrinos originating from the decay of the two taus contribute to  $E_T^{miss}$  as reconstruction of taus is only done for the visible decay products.

The SUSY signal points were simulated with HERWIG++ [50] including the full detector simulation. The following assumptions were made. Sneutrinos, selectrons and smuons are set to very high mass. Therefore only pairs of purely left-handed staus or purely right-handed staus are produced. The mass of the left-handed stau is assumed to be equal to the mass of the right-handed stau. Depending on the pMSSM parameters, staus can also decay to a chargino and a tau-neutrino. However the branching ratio for this decay is zero in the SUSY signal points that were used in this analysis as the chargino is too heavy to be produced. The signal points differ in the assumed mass of the stau and the mass of the lightest neutralino. As direct stau production is one of the SUSY processes with the smallest production cross-section at the LHC, the signal points are simulated with relatively low stau masses. Furthermore the current limit on the stau mass is  $> 81.9$  GeV, which was set at the DELPHI experiment at the LEP machine [10]. These chosen pMSSM parameters heavily influence the direct stau

production cross-section and the kinematics of the stau decay. As all gaugino masses except  $m_{\tilde{\chi}_{01}}$  are higher than the stau mass, the stau only decays via  $\tilde{\tau}^\pm \rightarrow \tau^\pm \tilde{\chi}_1^0$ . The parameters of the SUSY signal points and their respective production cross-sections are given in Table 5.1

The production cross-sections were calculated with Prospino [23] and are scaled to next-to-leading order using a  $k$ -factor ( $k = 1.3$ ), which is the multiplicative factor accounting for next-to-leading order contributions.

This thesis considers 4 signal points. After a first preliminary study more points are being generated but were not available at the time when this thesis was written.

$m_{\tilde{\tau}}$ [GeV]	$m_{\tilde{\chi}_0}$ [GeV]	$\sigma_{prod}$ [fb] (NLO)
100	0	131.38
100	20	131.16
100	40	129.34
120	0	73.66

Table 5.1: Properties of the 4 Signal MC Points used in the direct stau analysis. Each signal point contained 25000 generated events in full detector simulation with Herwig++ [50]

### 5.1.1 Data Samples

The analysis uses a data sample with an integrated luminosity of  $\int L = 5 \text{ fb}^{-1}$  recorded by the ATLAS detector during the  $p$ - $p$  collision runs at  $\sqrt{s} = 8 \text{ TeV}$  in 2012. The uncertainty on the integrated luminosity is estimated to be 3.6 % [51]. Via a "Good-Run-List" (GRL) the data quality and subsystem requirements are imposed. The GRL lists runs and luminosity blocks for which data quality and subsystem requirements are fulfilled.

The analysis is still 'blinded' at the first  $5 \text{ fb}^{-1}$  collected in 2012 at ATLAS. The full dataset corresponds to  $20.7 \text{ fb}^{-1}$  after the GRL has been imposed. 'Blinding' is a common practice in particle physics. When an analysis is developed to look for a faint signal in data it is possible that the physicist will wrongly interpret a statistical fluctuation in data as a true signal. The physicist could then deliberately or subconsciously fine-tune the analysis to enhance the significance of this feature. To avoid this, analyses are 'blinded' which usually means that the physicist is not allowed to look at data in the signal region while the analysis is under development. Once the analysis is fixed and approved it is 'unblinded'.

However this analysis was not 'blinded' in terms of the signal region but to a small part of the available dataset. The analysis is 'blinded' to  $5 \text{ fb}^{-1}$  of the available  $20.7 \text{ fb}^{-1}$  dataset collected by ATLAS in 2012. For this small part of the dataset the signal region is not 'blinded' due to the fact that a signal of direct stau production is not expected to be visible in  $5 \text{ fb}^{-1}$ .

## 5.2 Standard Model Background

A number of Standard Model processes contribute to the background for direct stau production. In this analysis they are categorized as Z+Jets, W+Jets, DiBoson,  $t\bar{t}$ , SingleTop and QCD multijet processes. In the following it is described which generators were used to simulate them, which processes are simulated and how these can lead to a final state with two oppositely charged taus (OS Region).

- **Z+Jets:**  
The Z+Jets MC samples were simulated with Sherpa [52]. The branching fraction of the Z-boson to decay to two oppositely charged taus is 3.37 % [10].
- **W+Jets:**  
The W+Jets MC samples were simulated with Sherpa [52]. The W-boson decays to a tau with a branching fraction of 11.25 % [10]. Furthermore a jet can be misidentified as a tau leading to a final state with two oppositely charged taus.
- **DiBoson:**  
The Diboson MC samples were simulated with Sherpa [52] and Jimmy [53]. They include WW, WZ and ZZ (Z stands for both the  $Z_0$ -boson and the photon) samples. These processes can lead to a final state with two oppositely charged taus in numerous ways according to the previously noted branching fractions of the W-bosons and Z-boson. Furthermore final states with more than two taus can contribute in the OS region as taus can be missed by the detector or the object reconstruction.
- **SingleTop:**  
The SingleTop MC samples were simulated with Mc@NLOJimmy [54] and AcerMCPythia [55]. They contain processes with a top quark which mainly decays to  $Wb$ . As the W-boson can decay to a tau and a jet can be misidentified as a tau these processes can also lead to a final state with two oppositely charged taus.
- **$t\bar{t}$**   
The  $t\bar{t}$  MC samples were simulated with Sherpa [52] and MadGraphPythia [56]. As noted previously a top quark mainly decays to a  $b$ -quark and a W-boson. The two W-bosons can then decay to two taus and tau-neutrinos.

The branching fraction of the hadronic decay of a tau is 64 % [10]. It should be noted that processes involving taus that decay leptonically are rejected due to the light lepton veto.

### 5.2.1 Estimation of the QCD multijet background

QCD multijet production is the major background process for processes with two taus in the final state. Jets can be misidentified as taus and due to the high QCD cross-section

the contribution to the SM background by these events is large.

For QCD multijet production no suitable MC sample is available. In this analysis the QCD multijet background is estimated from events with two hadronic taus with the same electric charge. This region is exclusive to the OS region and referred to as the same sign (SS) region.

In order to estimate the contribution due to QCD multijet processes in the OS region, from event yields in the SS region, two assumptions are made.

1. The data sample used in this analysis only consists of SM contributions. That means contributions from new physics are negligible.
2. The probability for QCD multijet processes to have two hadronic reconstructed taus with opposite charge is the same as to two hadronic taus with the same charge.

In this case the event yield in the OS region due to QCD multijet processes  $N_{OS,QCD}$  can be estimated using

$$N_{OS,QCD} = N_{SS,data} - N_{SS,SM(MC)}, \quad (5.1)$$

where

- $N_{SS,data}$  is the event yield in the SS region in the recorded data,
- $N_{SS,SM(MC)}$  is the event yield in the SS region due to all other contributing SM processes simulated with MC:  $Z/W+Jets$ ,  $t\bar{t}$ , Single Top and DiBoson.

To illustrate this as an example Figure 5.1 shows the distribution of the invariant mass of the two taus in the SS region. The purity of QCD events in the SS region is very high. Subtracting the event yields of the simulated SM contributions from the data gives the event yields from QCD multijet events. The result is used as an estimate for the QCD multijet background in the OS region which is shown in Figure 5.2. This is done for each bin of the histogram.

Further remarks about the distribution of the invariant mass of the two taus in the SS region have to be made. The distribution of data seems to peak at around 80 GeV which corresponds to the  $Z$ -boson peak seen in the OS distribution in Figure 5.2. As the  $Z$ -boson does not decay to taus with the same electric charge this is puzzling.

One possible explanation would be that the charge of one of the taus from a  $Z$ -boson decay is misidentified giving a final state with equally charged taus.

The charge of a hadronic tau is determined from the sum of the reconstructed track charges of its decay products. Charge misidentification of taus arises mostly from two effects. Single-prong decays can migrate to three-prong decays due to photon conversion or the presence of additional tracks from the underlying event. Also three-prong decays may be reconstructed as single-prong decays due to inefficiencies of the track

reconstruction and selection.

However the overall charge misidentification is estimated to be below  $\sim 3\%$  [28] and can therefore not explain the high event yield around 80 GeV.

The QCD contribution to the background is mainly due to di-jet events. In [57] the di-jet mass spectrum has been measured in the range  $48 \text{ GeV} \leq m(j, j) \leq 300 \text{ GeV}$ . It is shown in Figure 5.4 and shows a continuous rise (in a logarithmic graph) when going to lower invariant mass values. The shape of the data distribution in Figure 5.1 resembles this behaviour but is "cut off" at an invariant mass value of  $\sim 70 \text{ GeV}$ . This is due to the requirements on the  $p_T$  of the taus which were  $p_T(\tau^{\text{leading}}) > 40 \text{ GeV}$  and  $p_T(\tau^{\text{subleading}}) > 25 \text{ GeV}$ .

In Figure 5.3 the data distribution of the invariant mass of the two taus in the SS region is shown for higher  $p_T$  cuts of 60 GeV and 45 GeV for the leading and subleading tau respectively. One can see that the peak now moves to an invariant mass value of  $\sim 130 \text{ GeV}$ .

In conclusion the QCD estimation from events in the SS region works reasonably well. However in general the SM background is underestimated by approximately 15%. In the OS region the event yield is  $1.68 \cdot 10^5$  events in data and  $1.29 \cdot 10^5$  events in the estimated SM background. The SM background is therefore underestimated by  $\sim 22\%$  in total.

The development of the QCD estimation is not covered in this thesis as it would be very time consuming and is not necessary for a first sensitivity study for the search for direct stau production shown in this thesis. The QCD contribution can be estimated with more sophisticated techniques such as the data-driven ABCD method described in the CONF note [24].

For the development of the signal region it will be assumed that the events recorded at ATLAS are only events including SM processes (assumption 1).

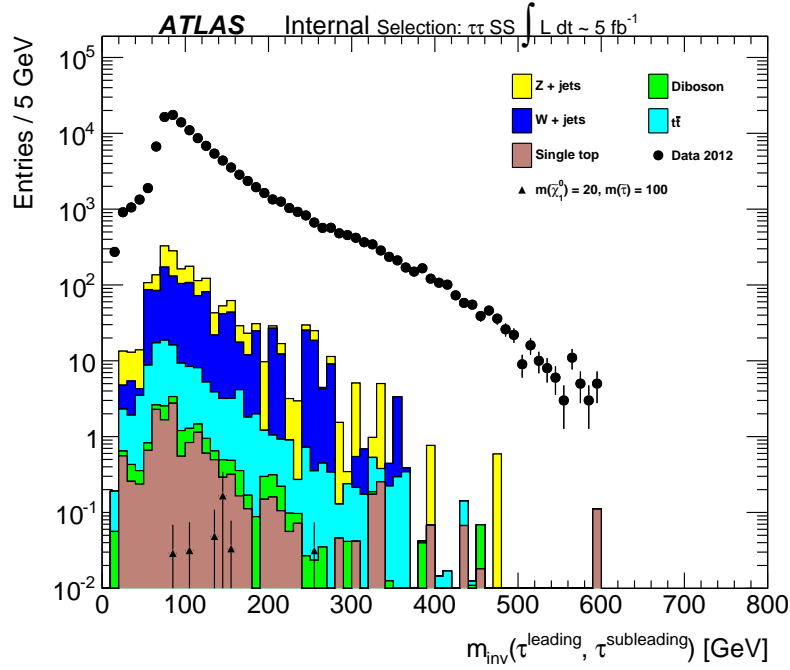


Fig. 5.1: Distribution of the invariant mass of the two taus in the SS region with  $p_T(\tau^{leading}) > 40$  GeV and  $p_T(\tau^{subleading}) > 25$  GeV.

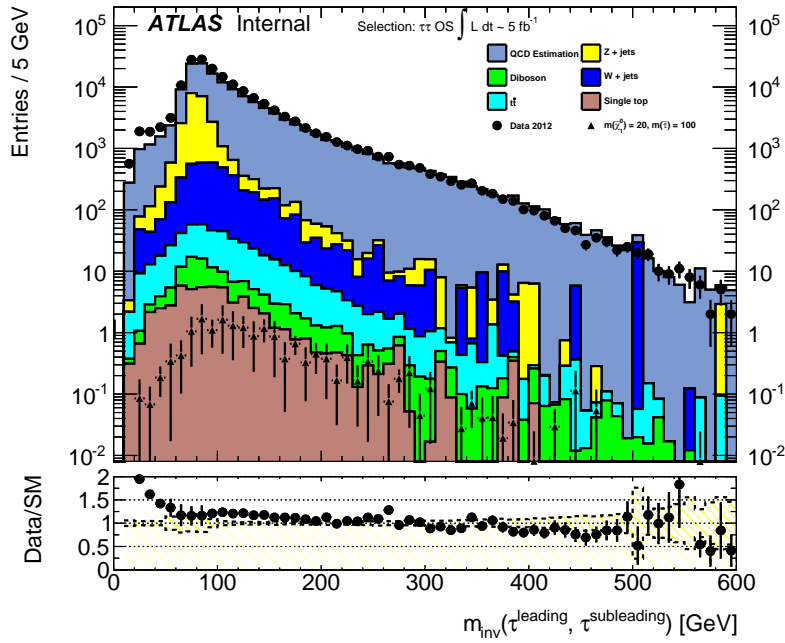


Fig. 5.2: Distribution of the invariant mass of the two taus in the OS region. The yellow band in the ratio plot at the bottom shows the ratio  $\frac{SMbackground}{SMbackground \pm 1\sigma error}$ .

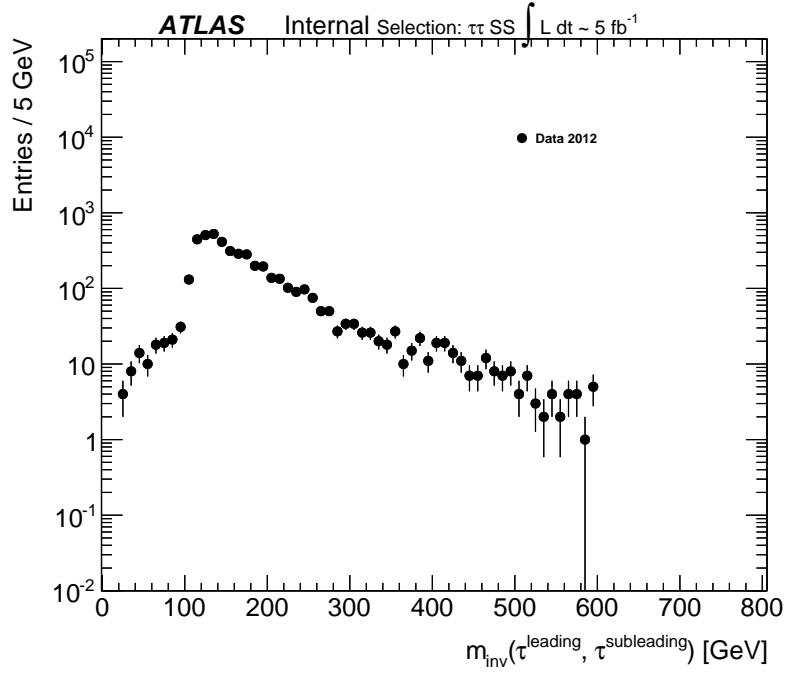


Fig. 5.3: Distribution of the invariant mass of the two taus in the SS region with  $p_T(\tau^{leading}) > 60$  GeV and  $p_T(\tau^{subleading}) > 45$  GeV.

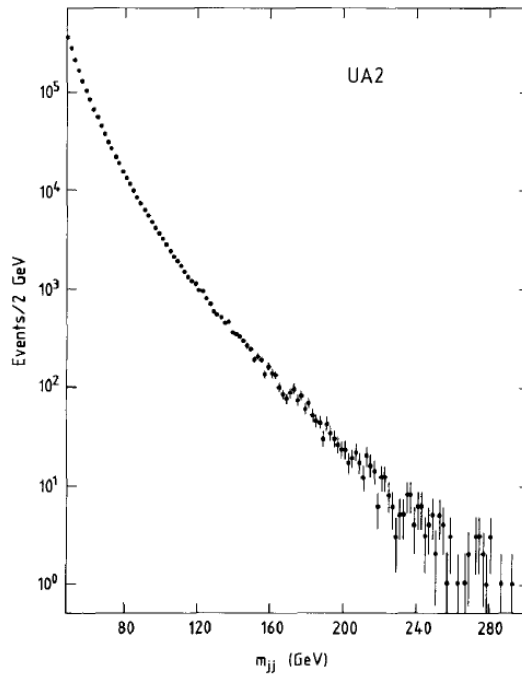


Fig. 5.4: The final di-jet mass spectrum measured by the UA2 collaboration at the CERN  $p\bar{p}$  collider [57].

## 5.3 Statistics

In an analysis for the search for a process that has been predicted but not yet seen, such as direct stau production, one wants to quantify the sensitivity of the analysis.

The figure of merit used here is the significance. In this analysis the significance that is used to optimize the signal region is defined as  $\frac{S}{\sqrt{S+B}}$ . In this definition  $S$  stands for the number of signal events and  $B$  for the number of SM background events. In this analysis the event yield in data is taken as the number of SM background events  $B$ . Therefore the errors on both the signal and the background events are poissonian. The systematic error is assumed to be zero.

### 5.3.1 Hypothesis Test

After the signal region is developed and the analysis selection is fixed, its expected sensitivity can be obtained using a hypothesis test for different signal hypotheses.

The hypotheses under consideration can be formulated as  $\mu S + B$ . Here,  $\mu$  is the signal strength parameter, which is a multiplicative factor on the signal production cross-section. The background-only hypothesis corresponds to  $\mu = 0$ . The hypothesis with  $\mu = 1$  is the hypothesis for direct stau production.

In order to determine the level of agreement of a hypothesis with observed data (or expected signal+background) a hypothesis test is carried out. A test statistic  $t_\mu$  is introduced.  $t_\mu$  is a function of the expected signal and background events and the signal strength  $\mu$ . A commonly used variable is the  $p$ -value. The  $p$ -value for a given hypothesis H is the probability to find a test statistic equal to the one that was observed assuming that hypothesis H is true. The relationship between the  $p$ -value and the probability distribution function  $f(t_\mu|\mu)$  is shown in Figure 5.5.

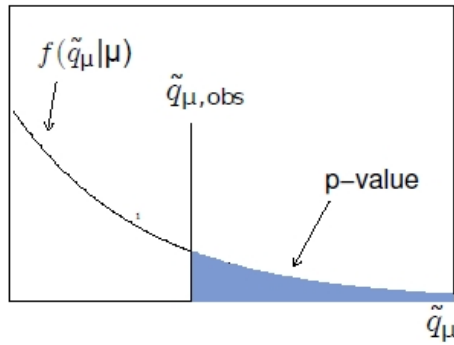


Fig. 5.5: Illustration how the  $p$ -value is obtained for a given test statistic  $\tilde{q}_\mu$  [58]



Integrating the probability distribution function gives the  $p$ -value

$$p_\mu = \int_{t_{\mu,obs}} f(t_\mu|\mu) dt_\mu, \quad (5.2)$$

where  $t_{\mu,obs}$  is the value of the test statistic observed from data (or expected signal+background).

In this analysis the used test statistic is a one sided profile test statistic

$$t_\mu = \begin{cases} \log \frac{L(\mu)}{L(\hat{\mu})} \\ 0, \end{cases} \quad \mu < \hat{\mu} \quad . \quad (5.3)$$

where  $L(\hat{\mu})$  is the maximized likelihood.

If only statistical and no systematic errors are considered the exact form of the likelihood is that of a poissonian distribution

$$L(\mu) = \frac{(\mu S + B)^n}{n!} e^{-(\mu S + B)}, \quad (5.4)$$

where  $n$  is the event yield.

If systematic errors are considered in addition to statistical errors the likelihood will depend upon a nuisance parameter  $\Theta$  which broadens the distribution. The nuisance parameter  $\Theta$  considers all systematic errors and the likelihood is now written as  $L(\mu, \Theta)$ .

### 5.3.2 Exclusion Limits

Ultimately the confidence level [58] in a certain hypothesis can be computed. For the signal+background hypothesis, corresponding to  $\mu = 1$  it is given by

$$CL_{S+B} = \int_{-\infty}^{t_{\mu,obs}} f(t_1|B) dt_1. \quad (5.5)$$

For the background-only hypothesis, corresponding to  $\mu = 0$ , it is defined analogously as

$$CL_B = \int_{-\infty}^{t_{\mu,obs}} f(t_0|B) dt_0. \quad (5.6)$$

High values for CL are achieved for a high level of agreement with the hypothesis.

The frequentist confidence level is given as

$$CL_S = \frac{CL_{S+B}}{CL_B}. \quad (5.7)$$

In order to exclude the signal hypothesis at a confidence level CL, the inequality

$$CL \geq 1 - CL_S \quad (5.8)$$

has to be fulfilled. Typically a confidence level CL of 95 % is considered as an exclusion. Using a number of signal hypotheses with varying signal strength  $\mu$  one can determine the hypothesis with the largest signal strength  $\mu$  which can not be excluded at 95 % confidence level. This is called the upper exclusion limit on the signal strength and quantifies the sensitivity of an analysis.

## 5.4 Preselection

After events have passed the event quality and trigger requirements, events have to fulfill preselection criteria. According to the experimental signature of direct stau production which was discussed in 5.1, events with exactly two oppositely charged hadronic taus and no light leptons in the final state are selected. As noted before this is referred to as the OS region.

In order to suppress SM background contributions, further selection cuts have to be applied. A range of variables seemed promising and the distributions of variables considered in the preselection are shown in Figure 5.6, 5.7, 5.8, 5.9 and 5.10. Distributions for other promising variables in the OS region can be found in Appendix A.

One of the largest contributions to the SM background originates from the decay of the Z-boson to two oppositely charged taus. In order to reject these events a Z-Veto is applied. The Z-Veto rejects events with an invariant mass of the two reconstructed taus between 71 GeV and 91 GeV. The invariant mass range that is rejected is chosen to be lower than the invariant mass of 91 GeV that one would expect due to the decay of a Z-boson. This is due to the fact that taus are only reconstructed using their visible decay products. Due to the escaping tau neutrinos the full energy of the tau is not reconstructed.

In the invariant mass distribution in the OS region in Figure 5.6 one can see that the Z-Veto will reduce the Z+Jets background significantly.

Further event variables can be constructed using the angular distribution of the taus and the  $E_T^{miss}$  vector such as the difference of the pseudorapidity between the reconstructed tau vectors

$$\Delta\eta(\tau, \tau) = |\eta(\tau^{leading}) - \eta(\tau^{subleading})|, \quad (5.9)$$

the distance between the two reconstructed tau vectors in the pseudorapidity-azimuthal angle plane

$$\Delta R(\tau, \tau) = \sqrt{(\eta(\tau^{leading}) - \eta(\tau^{subleading}))^2 + (\phi(\tau^{leading}) - \phi(\tau^{subleading}))^2} \quad (5.10)$$

and the angle between the  $E_T^{miss}$  vector and the tau vector in the  $\phi$  plane

$$\Delta\phi(\triangleleft E_T^{miss}, \tau) = \phi(E_T^{miss}) - \phi(\tau), \Delta\phi \in [0, \pi] \quad (5.11)$$

where the smaller angle of the angle between  $E_T^{miss}$  and one of the taus is selected.

The selected cuts are the following.

- $\Delta\eta(\tau, \tau) < 1.7 \text{ rad}$
- $0.7 \text{ rad} < \Delta R(\tau, \tau) < 3.3 \text{ rad}$
- $\min.(\Delta\phi(\triangleleft E_T^{miss}, \tau)) < 1.7 \text{ rad}$

The cut values were chosen to optimally exploit the difference in the shape of the signal (MC) and background (data) distributions. At the cut values the signal distribution

falls steeper than the SM background (data) distribution. The cuts on  $\Delta\eta(\tau, \tau)$  and  $\Delta R(\tau, \tau)$  reduce prominently the QCD background. The cut on  $\min.(\Delta\phi(\triangleleft E_T^{miss}, \tau))$  does not reduce a specific background contribution but is in general a good discriminant between SM background and SUSY signal.

In the process of direct stau production no jet is present in the final state of the Feynman diagram. However events can be accompanied by jets due to initial state radiation (ISR). Rejection of events with a b-jet in the final state (b-jet veto) improves the significance in this analysis. The b-jet veto significantly reduces the contribution from processes involving a top quark, such as  $t\bar{t}$  and SingleTop.

The event yields for data and SM background in the OS region and after the preselection cuts have been applied can be seen in Table 5.3. The event yields for the SUSY signal points and the achieved significance  $\frac{S}{\sqrt{(S+B)}}$  in the OS region and after the preselection cuts have been applied can be seen in Table 5.4. It can be seen from the table that the preselection cuts improve the significance.

The preselection cuts are summarized in Table 5.2.

Preselection
$71 \text{ GeV} < m(\tau, \tau) < 91 \text{ GeV}$ (Z Veto)
b-Jet Veto
$\Delta\eta(\tau, \tau) < 1.7 \text{ rad}$
$0.7 \text{ rad} < \Delta R(\tau, \tau) < 3.3 \text{ rad}$
$\min.(\Delta\phi(\triangleleft E_T^{miss}, \tau)) < 1.7 \text{ rad}$

Table 5.2: The preselection cuts

	OS region	Preselection region
Data	$674001 \pm 16410$	$161100 \pm 802$
Sum SM background	$518491 \pm 1456$	$128180 \pm 183$
Z+Jets	$82080 \pm 60$	$17080 \pm 30$
W+Jets	$15430 \pm 0.1$	$5440 \pm 0.01$
DiBoson	$271.6 \pm 3.8$	$92.50 \pm 2.07$
SingleTop	$222.3 \pm 8.6$	$24.03 \pm 2.78$
$t\bar{t}$	$1540 \pm 16$	$64.49 \pm 3.14$
QCD	$419148 \pm 1456$	$105480 \pm 181$

Table 5.3: Event yields for data (scaled to  $20.7 \text{ fb}^{-1}$ ), MC Contributions (normalized to  $20.7 \text{ fb}^{-1}$ ) and the QCD estimation( $20.7 \text{ fb}^{-1}$ ) for the OS region and after the preselection cuts have been applied

Signal		OS	Preselection	$\frac{S}{\sqrt{S+B}}$ (OS)	$\frac{S}{\sqrt{S+B}}$ (Preselection)
$m_{\tilde{\tau}}$ [GeV]	$m_{\tilde{\chi}_0}$ [GeV]				
100	0	$67.1 \pm 2.7$	$45.3 \pm 2.2$	$(8.18 \pm 0.01) \cdot 10^{-2}$	$(11.28 \pm 0.06) \cdot 10^{-2}$
100	20	$66.5 \pm 2.7$	$42.6 \pm 2.1$	$(8.10 \pm 0.01) \cdot 10^{-2}$	$(10.60 \pm 0.05) \cdot 10^{-2}$
100	40	$54.5 \pm 2.4$	$35.8 \pm 1.9$	$(6.66 \pm 0.0) \cdot 10^{-2}$	$(8.92 \pm 0.04) \cdot 10^{-2}$
120	0	$42.1 \pm 1.6$	$28.5 \pm 1.3$	$(5.13 \pm 0.01) \cdot 10^{-2}$	$(7.09 \pm 0.03) \cdot 10^{-2}$

Table 5.4: Event yields for SUSY signal points (normalized to  $20.7 \text{ fb}^{-1}$ ) and the  $\frac{S}{\sqrt{S+B}}$  significance in the OS region and after the preselection cuts have been applied

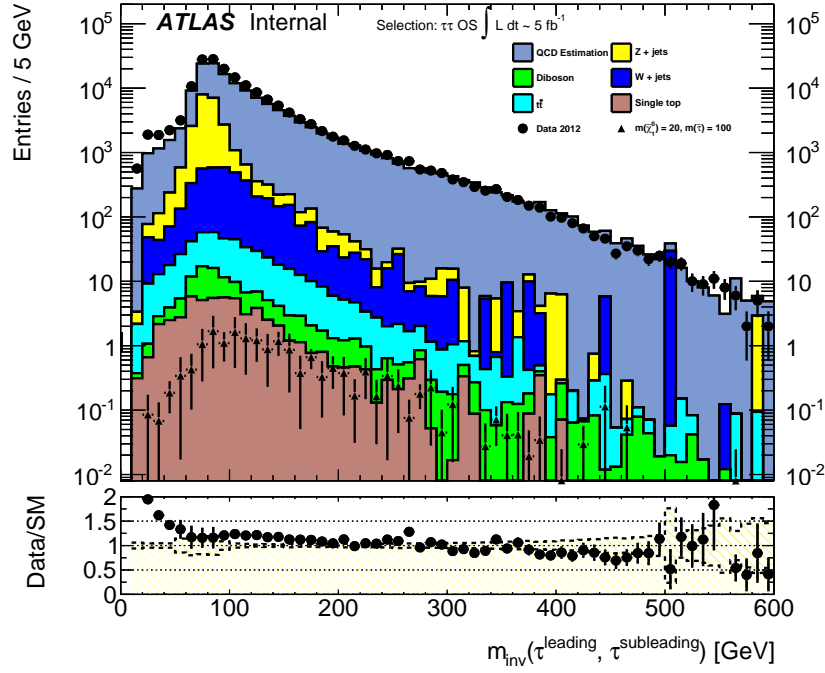


Fig. 5.6: Distribution of  $m(\tau, \tau)$  in the OS region.

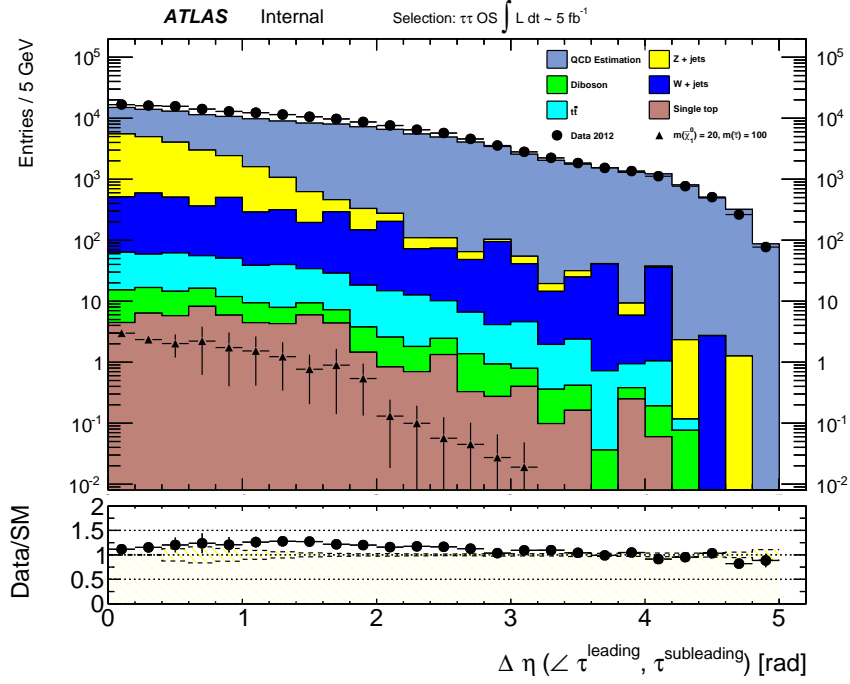


Fig. 5.7: Distribution of  $\Delta\eta(\tau, \tau)$  in the OS region.

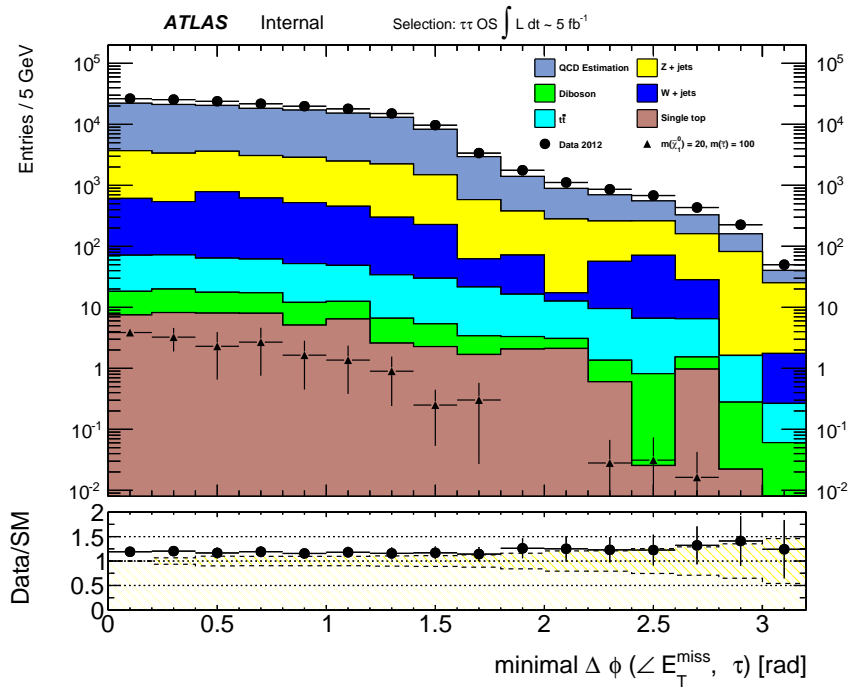


Fig. 5.8: Distribution of  $\min.(\Delta\phi(\angle E_T^{\text{miss}}, \tau))$  in the OS region.

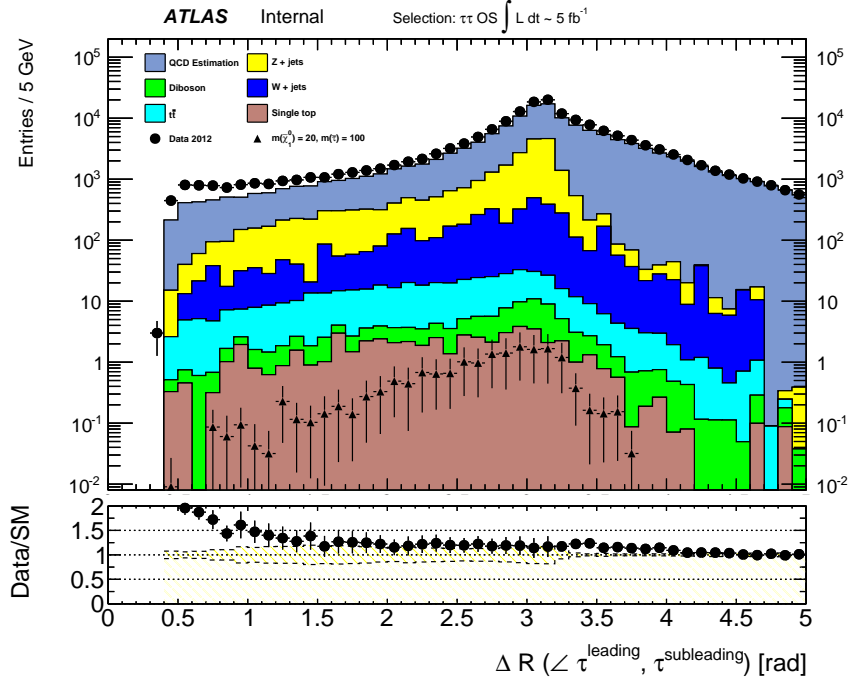


Fig. 5.9: Distribution of  $\Delta R(\tau, \tau)$  in the OS region.

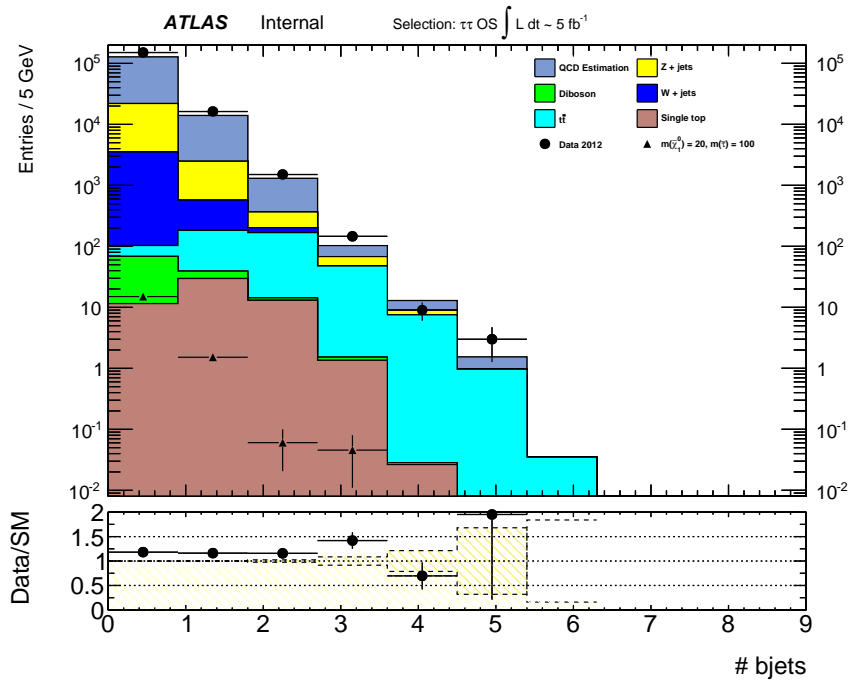


Fig. 5.10: Distribution of the number of b-jets in the OS region.

## 5.5 Signal Region

The signal region was developed using a scan of the parameter space spanned by the variables  $E_T^{miss}$ ,  $m_{eff} = H_T + E_T^{miss}$  and  $H_T = p_T^{\tau_{leading}} + p_T^{\tau_{subleading}}$ .

The taus originating from the decay of the produced staus, are expected to have higher  $p_T$  on average due to the large mass of the stau (here 100-120 GeV) than the taus that are produced in SM processes. Furthermore large  $E_T^{miss}$  is expected in events with direct stau production due to the escaping neutralinos and neutrinos. Due to the large mass of the neutralino  $\chi_0^1$  (here 0-40 GeV) the missing transverse energy  $E_T^{miss}$  is expected to be larger on average than in SM processes.

$m_{eff}$  is defined as the sum of  $E_T^{miss}$  and  $H_T$ , and therefore it is also expected to be a good discriminant between signal and SM events. The distributions of these variables after the preselection cuts are shown in the appendix B. As expected they show differences in the shape of the signal and SM background distribution and therefore the selection criteria for these variables have the ability to reject SM background events to a larger extent than signal events.

The following optimization of the signal region was carried out for one of the signal points. The signal point that was chosen is characterized by  $m(\tilde{\tau}) = 100$  GeV,  $m(\tilde{\chi}_1^0) = 20$  GeV. This point was chosen due to its relatively large cross-section compared to the other points.

First 2-D scans were carried out. In Figure 5.14 the result of the 2-D scan of the cut values for  $H_T$  and  $m_{eff}$  is shown. The values on the  $x$ - and  $y$ -axis correspond to the value under which events are rejected. The  $\frac{S}{\sqrt{S+B}}$  is computed for each cut value pair and is plotted on the  $z$ -axis. As can be seen from the plot the highest significance 0.72 is reached for  $H_T > 220$  GeV,  $m_{eff} > 220$  GeV.

In Figure 5.16 the result of the 2-D scan for the cut values for  $E_T^{miss}$  and  $m_{eff}$  is shown. The highest significance 0.68 is reached here for  $E_T^{miss} > 100$  GeV,  $m_{eff} > 350$  GeV.

The highest significance overall is reached in the 2-D scan, for the cut values for  $E_T^{miss}$  and  $H_T$ . The optimal cut value pair is found at  $E_T^{miss} > 140$  GeV,  $H_T > 120$  GeV which leads to a significance of 0.85.

In addition to the 2-D scans, a 3-D scan for all three variables was carried out. However the significance that was reached when cutting on all three variables did not improve the value of 0.85 that was found in the  $E_T^{miss}$  vs  $H_T$  scan.

The selection criteria for the signal region are summarized in Table 5.5.

Signal Region
<hr style="width: 50%; margin: 0 auto;"/>
OS region
Preselection cuts
$E_T^{miss} > 140$ GeV
$H_T > 120$ GeV

Table 5.5: Selection criteria for the signal region

The event yields in the Signal Region are shown in Table 5.6 for data and SM background

contributions for  $20.7 \text{ fb}^{-1}$ . The QCD estimation in the Signal Region for  $20.7 \text{ fb}^{-1}$  cannot be estimated as the analysis is blinded to  $5 \text{ fb}^{-1}$ . In Table 5.7 the event yields for the SUSY signal points and their respective significance are shown.

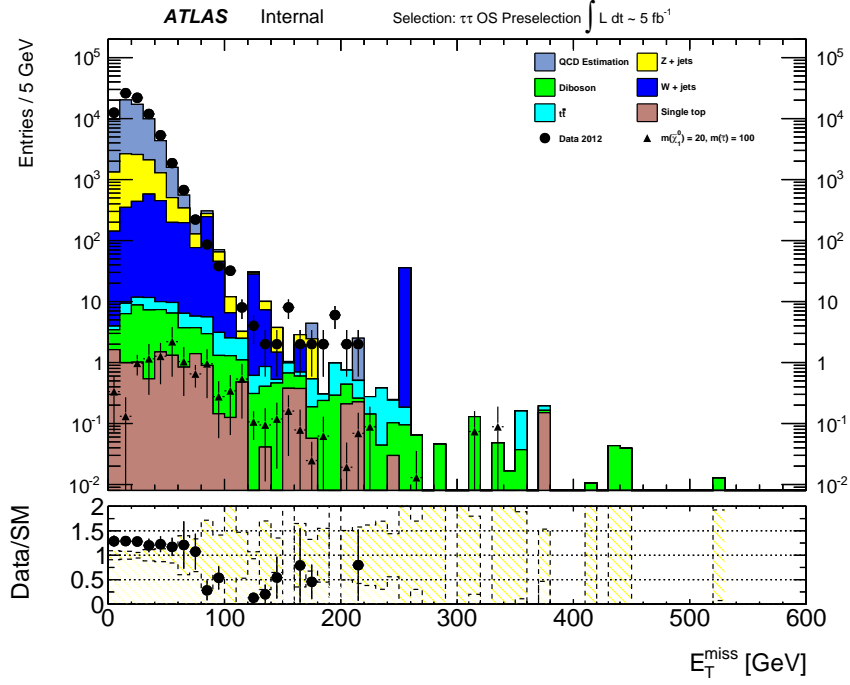


Fig. 5.11: Distribution of  $E_T^{\text{miss}}$  after the preselection cuts have been applied.



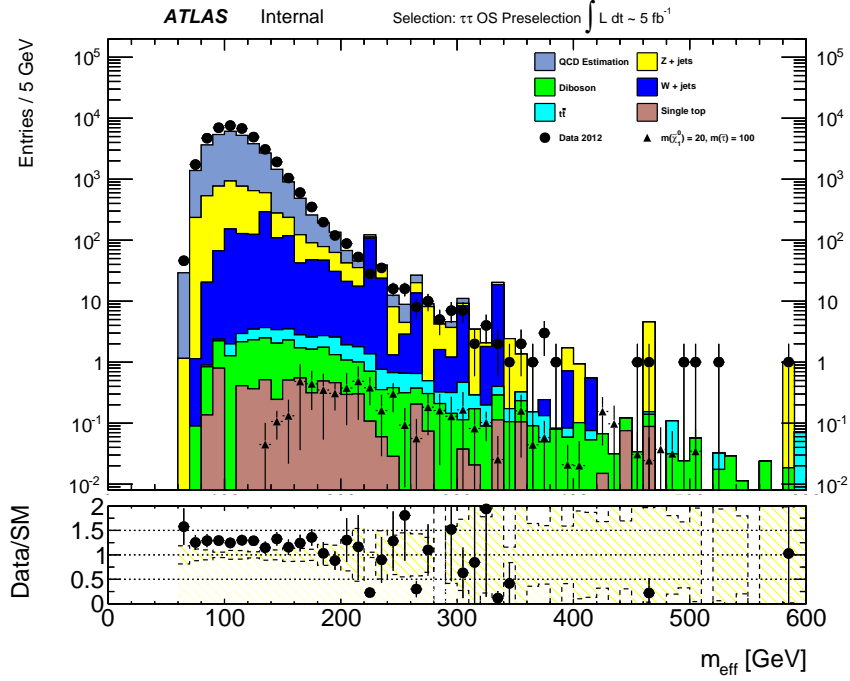


Fig. 5.12: Distribution of  $m_{\text{eff}}$  after the preselection cuts have been applied.

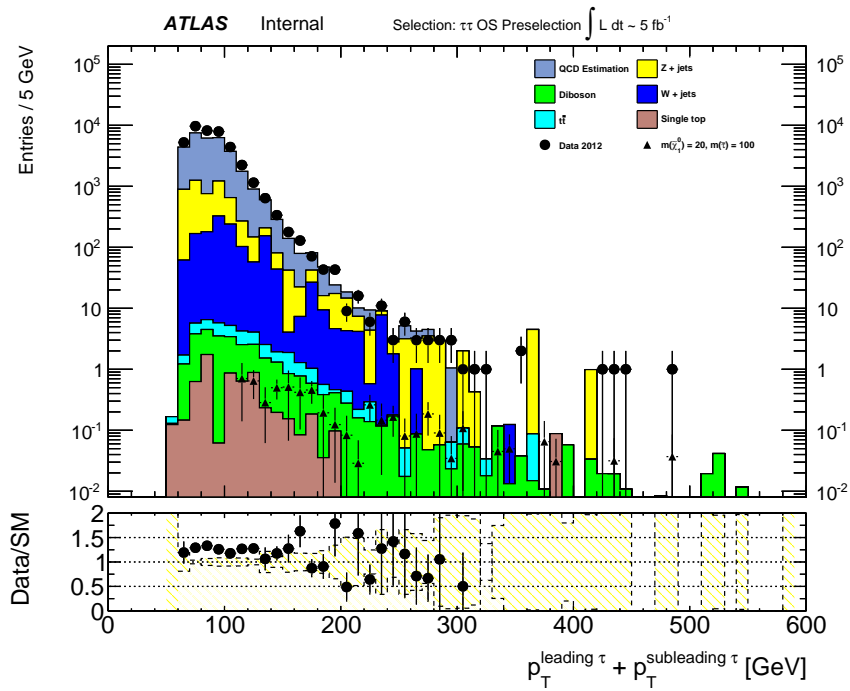


Fig. 5.13: Distribution of  $H_T$  after the preselection cuts have been applied.

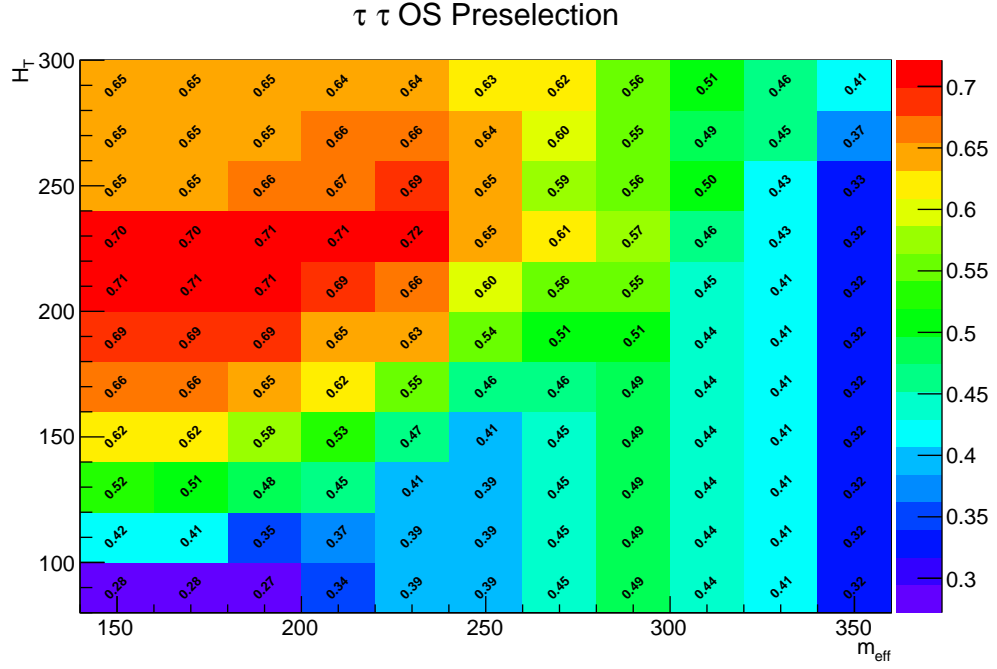


Fig. 5.14: Result of the cut-parameter scan of  $H_T$  vs  $m_{eff}$  cut values. The significance  $\frac{S}{\sqrt{S+B}}$  is plotted on the z-axis.

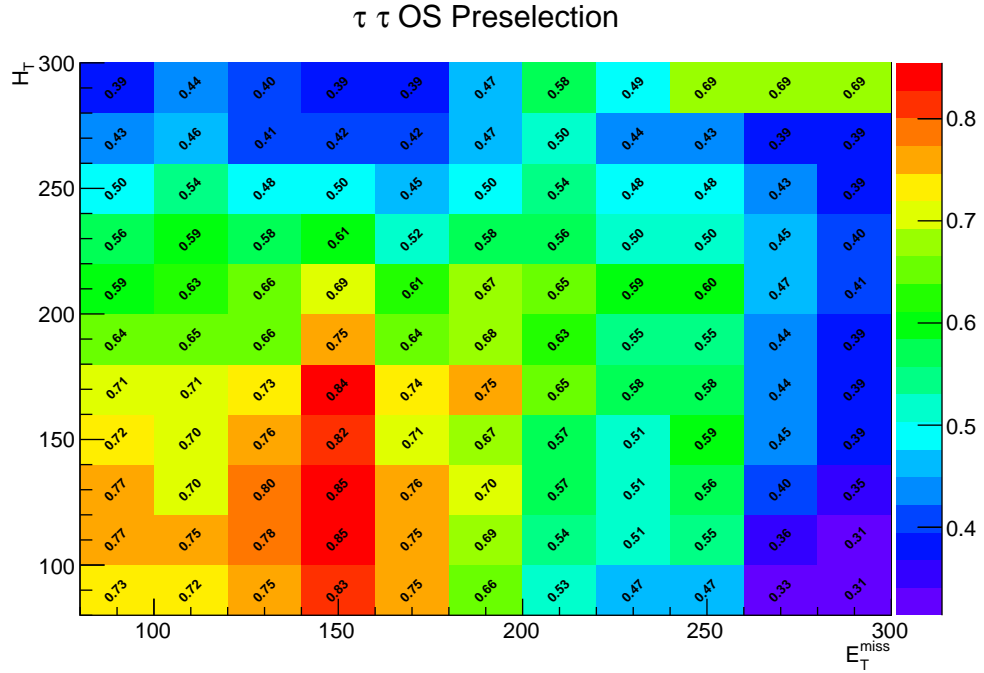


Fig. 5.15: Result of the cut-parameter scan of  $H_T$  vs  $E_T^{miss}$  cut values. The significance  $\frac{S}{\sqrt{S+B}}$  is plotted on the z-axis.

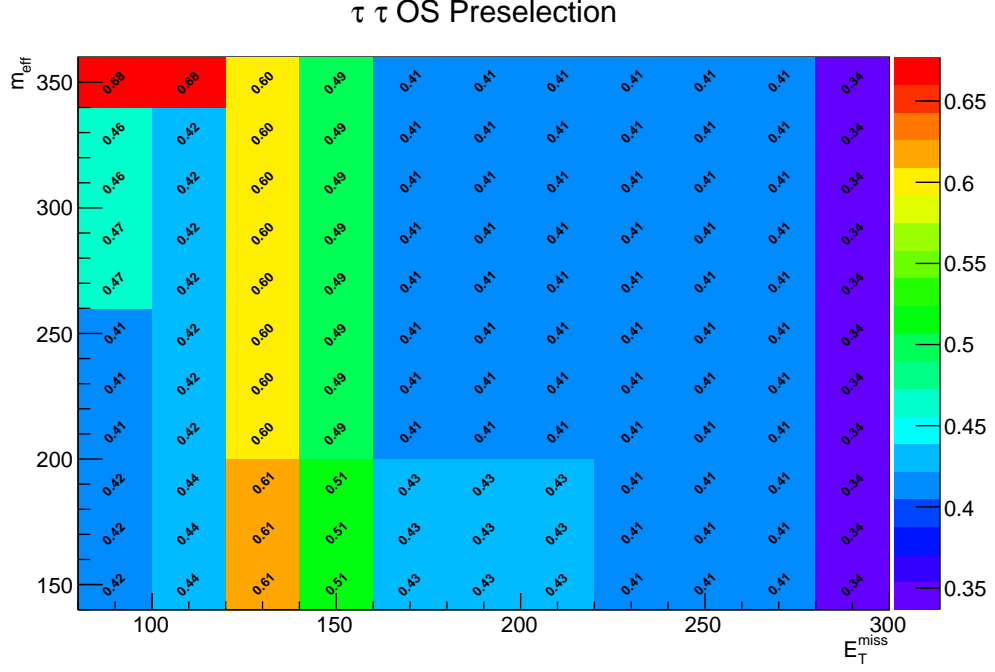


Fig. 5.16: Result of the cut-parameter scan of  $m_{eff}$  vs  $E_T^{miss}$  cut values. The significance  $\frac{S}{\sqrt{S+B}}$  is plotted on the z-axis.

	OS region	Preselection region	Signal Region
Data	$6740010 \pm 16410$	$161100 \pm 802$	$56.000 \pm 7.483$
Sum SM background	$518491 \pm 1456$	$128180 \pm 183$	
Z+Jets	$82080 \pm 60$	$17080 \pm 30$	$2.860 \pm 0.001$
W+Jets	$15430 \pm 0.1$	$5440 \pm 0.01$	$8.659 \pm 0.002$
DiBoson	$271.6 \pm 3.8$	$92.50 \pm 2.07$	$1.541 \pm 0.129$
SingleTop	$222.3 \pm 8.6$	$24.03 \pm 2.78$	$0.140 \pm 0.094$
$t\bar{t}$	$1540 \pm 16$	$64.49 \pm 3.14$	$1.018 \pm 0.186$
QCD	$419148 \pm 1456$	$105480 \pm 181$	

Table 5.6: Event yields for data (scaled to  $20.7\text{fb}^{-1}$ ), MC Contributions (normalized to  $20.7\text{fb}^{-1}$ ) and the QCD estimation( $20.7\text{fb}^{-1}$ ) for the OS region , the preselection region and the Signal Region.

Signal		Signal Region	$\frac{S}{\sqrt{S+B}}$ (SR)
$m_{\tilde{\tau}}$ [GeV]	$m_{\tilde{\chi}_0}$ [GeV]		
100	0	$6.68 \pm 0.84$	$0.84 \pm 0.05$
100	20	$6.77 \pm 0.84$	$0.85 \pm 0.05$
100	40	$3.81 \pm 0.63$	$0.49 \pm 0.03$
120	0	$5.91 \pm 0.59$	$0.75 \pm 0.04$

Table 5.7: Event yields for the SUSY signal points (normalized to  $20.7\text{fb}^{-1}$ ) and the  $\frac{S}{\sqrt{S+B}}$  significance in the Signal Region

## 5.6 Exclusion limits

In order to quantify the sensitivity of the analysis expected upper exclusion limits on the signal strength  $\mu$  are computed using the formalism outlined in section 5.3.2.

The errors on the signal and background event yields are poissonian and correspond to the errors given in Table 5.6 and 5.7.

The CL scans for each SUSY signal point are shown in Figures 5.17, 5.18, 5.19 and 5.20. A  $p$ -value of 1 indicates full agreement with the background only hypothesis while a hypothesis with a  $p$ -value equal or below 0.05 is considered to be excluded if the background-only hypothesis is true. The value for the signal strength  $\mu$  where the expected CLs is at  $p = 0.05$  gives the lowest production cross-section  $\mu \cdot \sigma_{prod}$  for direct stau production that is expected to be excluded with this analysis.

Table 5.8 lists the expected limits on  $\mu$  and the corresponding  $1\sigma$  and  $2\sigma$  band limits. In order for the analysis to be sensitive to direct stau production, meaning that the analysis has the power to exclude it, the exclusion limit has to be found at a signal strength  $\mu$  equal or smaller than 1. This is not the case and therefore this analysis is in conclusion not sensitive to direct stau production.

Furthermore in order to obtain observed exclusion limits, data cannot serve as a SM background estimate as was done in this analysis. The estimation of SM background from MC simulations or data-driven methods also adds systematic in addition to statistical errors. In order to quantify the sensitivity of the analysis in this case the exclusion limits were also computed using a systematic error of 30 % on background in addition to the poissonian statistical error. The resulting upper exclusion limits and the corresponding  $1\sigma$  and  $2\sigma$  band limits are shown in Table 5.9. The CL scans for each SUSY signal point are shown in Figure 5.21, 5.22, 5.23 and 5.24. As expected the sensitivity of the analysis decreases when a systematic error on background is added.

Signal		Upper Limit $\mu$	$-1\sigma$	$+1\sigma$	$-2\sigma$	$+2\sigma$
$m_{\tilde{\tau}}$ [GeV]	$m_{\tilde{\chi}_0}$ [GeV]					
100	0	3.71	2.52	5.68	1.82	8.79
100	20	3.65	2.49	5.60	1.79	8.66
100	40	6.66	4.49	10.40	3.24	16.28
120	0	4.18	2.85	6.46	2.67	10.03

Table 5.8: Upper limit for the signal strength  $\mu$  that is not expected to be excluded by the analysis for  $20.7\text{fb}^{-1}$ . The error on data is assumed to be only statistical.

Signal		Upper Limit $\mu$	$-1\sigma$	$+1\sigma$	$-2\sigma$	$+2\sigma$
$m_{\tilde{\tau}}$ [GeV]	$m_{\tilde{\chi}_0}$ [GeV]					
100	0	5.77	4.23	7.97	3.28	11.13
100	20	5.68	4.19	7.87	3.21	10.98
100	40	10.21	7.50	14.22	5.71	20.13
120	0	6.54	4.80	9.04	3.71	12.66

Table 5.9: Upper limit for the signal strength  $\mu$  that is not expected to be excluded by the analysis for  $20.7\text{fb}^{-1}$ . The error on data is assumed to be a combination of statistical and systematic. A systematic error of 30 % is assumed.

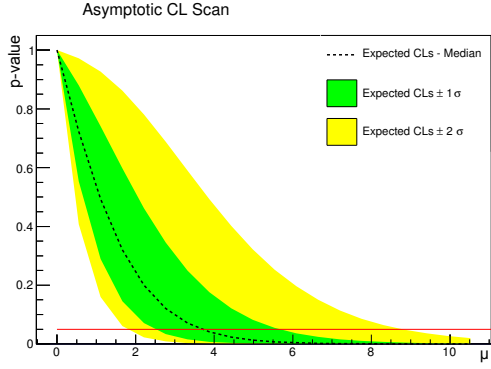


Fig. 5.17: Exclusion limit plot ( $p$ -value vs. signal strength  $\mu$ ) for the SUSY signal characterized by  $m_{\tilde{\tau}} = 100 \text{ GeV}$ ,  $m_{\tilde{\chi}_0} = 0 \text{ GeV}$  using only a statistical error for the background.

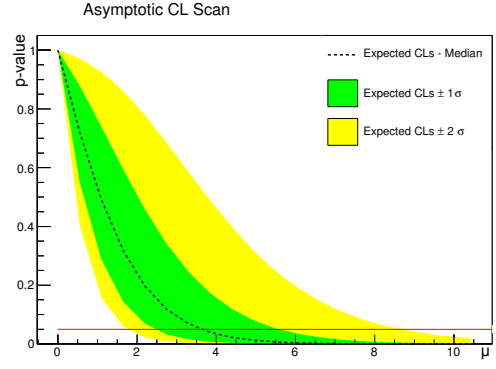


Fig. 5.18: Exclusion limit plot ( $p$ -value vs. signal strength  $\mu$ ) for the SUSY signal characterized by  $m_{\tilde{\tau}} = 100 \text{ GeV}$ ,  $m_{\tilde{\chi}_0} = 20 \text{ GeV}$  using only a statistical error for the background.

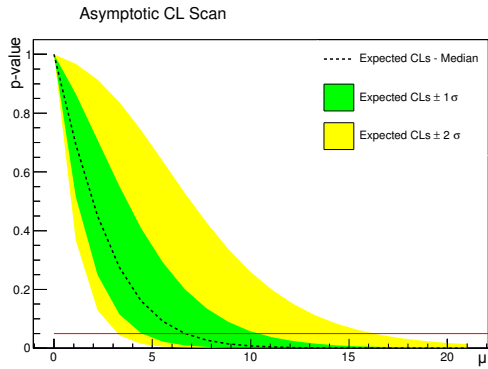


Fig. 5.19: Exclusion limit plot ( $p$ -value vs. signal strength  $\mu$ ) for the SUSY signal characterized by  $m_{\tilde{\tau}} = 100 \text{ GeV}$ ,  $m_{\tilde{\chi}_0} = 40 \text{ GeV}$  using only a statistical error for the background.

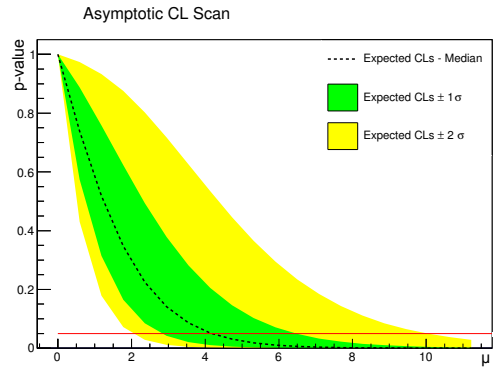


Fig. 5.20: Exclusion limit plot ( $p$ -value vs. signal strength  $\mu$ ) for the SUSY signal characterized by  $m_{\tilde{\tau}} = 120 \text{ GeV}$ ,  $m_{\tilde{\chi}_0} = 0 \text{ GeV}$  using only a statistical error for the background.

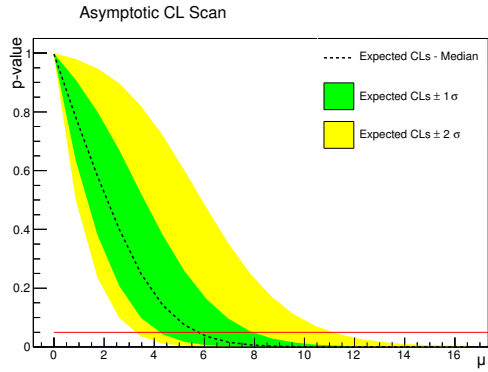


Fig. 5.21: Exclusion limit plot ( $p$ -value vs. signal strength  $\mu$ ) for the SUSY signal characterized by  $m_{\tilde{\tau}} = 100 \text{ GeV}$ ,  $m_{\tilde{\chi}_0} = 0 \text{ GeV}$  using a systematic error of 30 % for the background in addition to the statistical error.

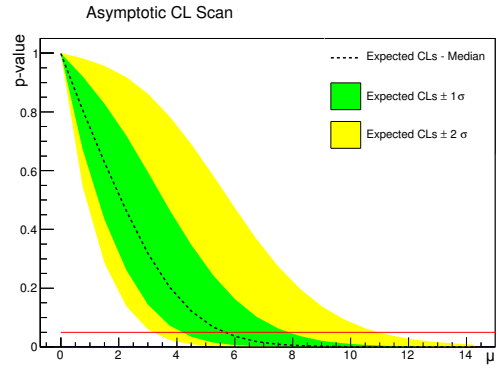


Fig. 5.22: Exclusion limit plot ( $p$ -value vs. signal strength  $\mu$ ) for the SUSY signal characterized by  $m_{\tilde{\tau}} = 100 \text{ GeV}$ ,  $m_{\tilde{\chi}_0} = 20 \text{ GeV}$  using a systematic error of 30 % for the background in addition to the statistical error.

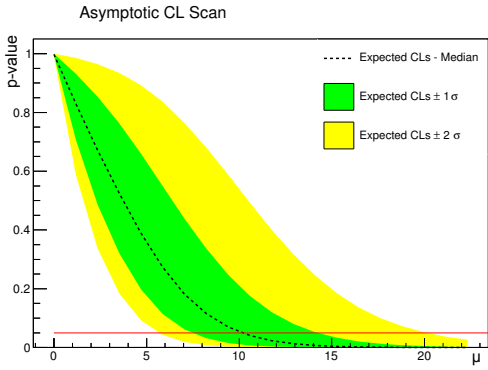


Fig. 5.23: Exclusion limit plot ( $p$ -value vs. signal strength  $\mu$ ) for the SUSY signal characterized by  $m_{\tilde{\tau}} = 100 \text{ GeV}$ ,  $m_{\tilde{\chi}_0} = 40 \text{ GeV}$  using a systematic error of 30 % for the background in addition to the statistical error.

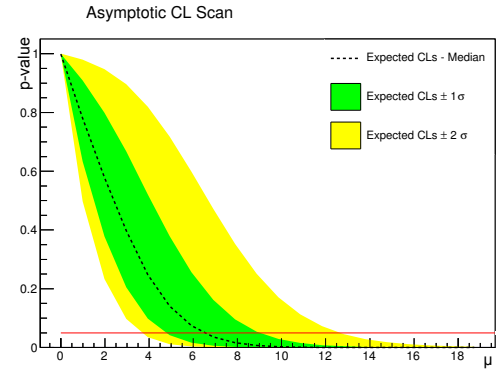


Fig. 5.24: Exclusion limit plot ( $p$ -value vs. signal strength  $\mu$ ) for the SUSY signal characterized by  $m_{\tilde{\tau}} = 120 \text{ GeV}$ ,  $m_{\tilde{\chi}_0} = 0 \text{ GeV}$  using a systematic error of 30 % for the background in addition to the statistical error.

---

## CHAPTER 6

# Further optimization studies of direct gaugino and direct stau searches

The ATLAS collaboration searches for SUSY in different distinct production channels. One of those channels is the direct electroweak production of sparticles leading to two hadronically decaying taus in the final state. The studies presented in this chapter were carried out to improve the sensitivity of this analysis.

Two studies were carried out. The first study (presented in section 6.1) answers the question if the sensitivity of the analysis could be improved if the selection requirement on the number of taus in the final state is changed.

The second study (presented in section 6.2) answers the question if lower trigger thresholds for the di-tau trigger have the potential to improve the sensitivity of the analysis. Both studies are carried out at truth level which means that the detector simulation is not taken into account. This allows us to decouple the ‘physical’ properties of the SUSY decays from reconstruction effects.

A signal grid with 169 points was simulated with Herwig++ [50] for  $p$ - $p$  collisions with a center of mass energy  $\sqrt{s} = 8$  TeV. The pMSSM parameters were chosen in such a way to achieve significant production cross-sections for the electroweak production of charginos, neutralinos and staus. In this grid only right-handed staus are included. The stau mass  $m_{\tilde{\tau}}$  is set to a low value of 95 GeV above the conservative LEP limit of 81.7 GeV [10] for every grid point. The other sleptons are set to be very heavy. In summary the significant pMSSM parameters for the generated grid are the following:

- $M_2 \in [100, 500]$  GeV
- $\mu \in [100, 500]$  GeV
- $M_1 = 50$  GeV
- $\tan(\beta) = 50$
- $m_{\tilde{\tau}} = 95$  GeV

The masses of the neutralinos and charginos depend on  $M_1, M_2$ ,  $\tan(\beta)$  and  $\mu$  and therefore vary throughout the grid.

The relative cross-sections for direct gaugino and direct stau production in this grid are



shown in Figure 6.1.

The relative cross-sections vary according to the masses of charginos and neutralinos. For high  $M_2$  and  $\mu$  the relative cross-section for direct stau production is large due to the high mass of the neutralinos and charginos. The rest of the grid is dominated by the production of the lightest charginos and neutralinos  $\tilde{\chi}_1^\pm$ ,  $\tilde{\chi}_1^0$  and  $\tilde{\chi}_2^0$ . In addition heavy charginos and neutralinos are also produced with a significant cross-section. These will decay to lighter charginos and neutralinos due to  $R$ -parity conservation. The branching fraction of  $\tilde{\chi}_2^\pm$  is shown in Figure 6.4. The branching fractions of the  $\tilde{\chi}_1^\pm$  and  $\tilde{\chi}_2^0$  decay modes are shown in Figure 6.2 and 6.3 respectively. The decay of  $\tilde{\chi}_1^\pm$  and  $\tilde{\chi}_2^0$  are almost exclusively to  $\tilde{\tau} \nu$  and  $\tilde{\tau} \tau$  respectively. For low  $M_2$  and  $\mu$  the decay to  $\tilde{\chi}_1^0 + \text{jets}$  has a significant branching ratio. As the analysis imposes a jet veto the event yield in this region of the grid is expected to be small. The Feynman diagrams for direct gaugino production are shown in Figure 2.5.

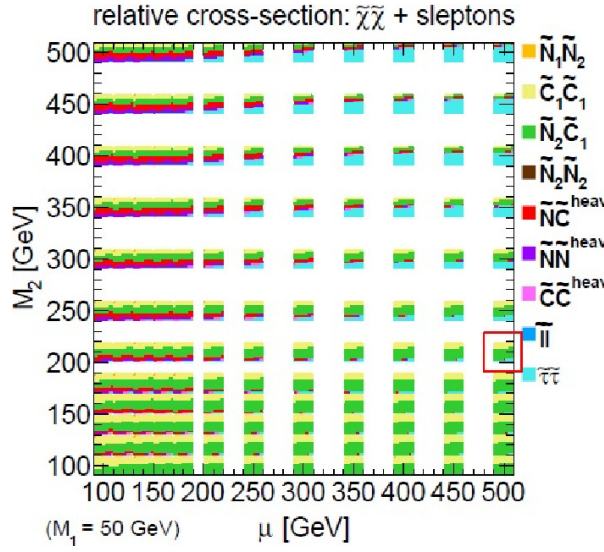


Fig. 6.1: Relative production cross-sections in the pMSSM signal grid. The size of the coloured area in a rectangle for a specific process is proportional to its cross-section. The plot was provided by a member of the workgroup.

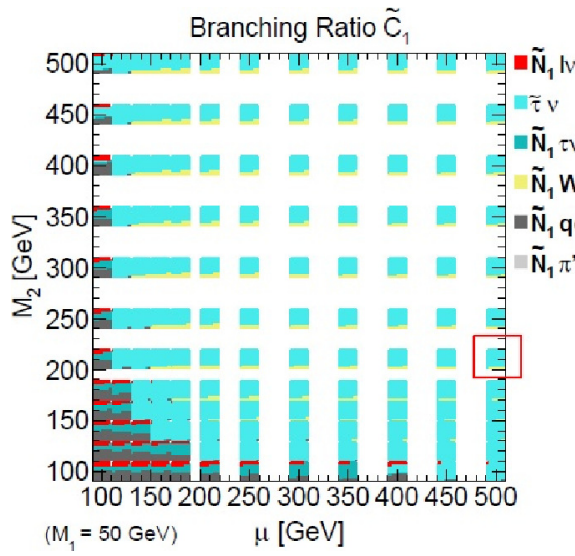


Fig. 6.2: Branching fractions for the decay of  $\tilde{\chi}_1^\pm$ . The plot was provided by a member of the workgroup.

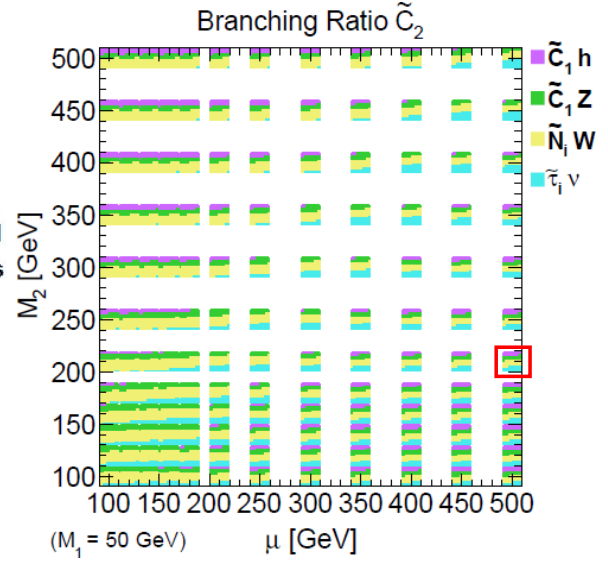


Fig. 6.4: Branching fractions for the decay of  $\tilde{\chi}_2^\pm$ . The plot was provided by a member of the workgroup.

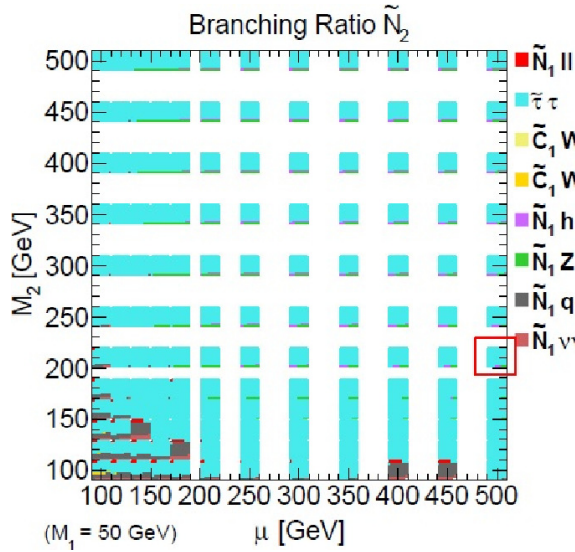


Fig. 6.3: Branching fractions for the decay of  $\tilde{\chi}_2^0$ . The plot was provided by a member of the workgroup.

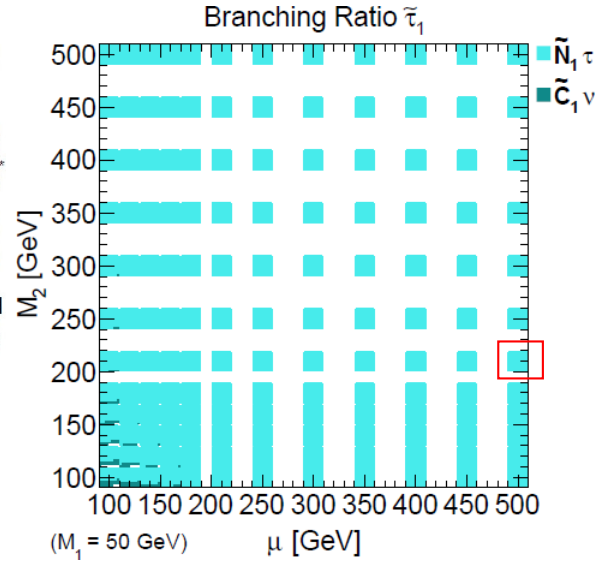


Fig. 6.5: Branching fractions for the decay of  $\tilde{\tau}$ . The plot was provided by a member of the workgroup.

## 6.1 Number of taus

At the time this study was carried out the di-tau analysis selected events with exactly two taus in the final state.

The question that this study is trying to answer is whether the sensitivity of the analysis can be improved by also selecting events with exactly one tau and events with more than two taus in the final state. In Figures 6.1, 6.2, 6.3, 6.5 the signal point characterized by  $M_1 = 50 \text{ GeV}, M_2 = 210 \text{ GeV}$  and  $\mu = 500 \text{ GeV}$  (marked with a red rectangle) is taken as a benchmark. As an example we will compute the expected branching ratios to single tau, two tau, and multitau events.

The relative production cross-sections<sup>1</sup> for this signal point are

- $\sigma_{rel}(\tilde{\chi}_2^0 \tilde{\chi}_1^\pm) = 63\%$
- $\sigma_{rel}(\tilde{\chi}_1^+ \tilde{\chi}_1^-) = 30\%$
- $\sigma_{rel}(\tilde{\tau} \tilde{\tau}) = 5\%$
- $\sigma_{rel}(other) \sim 2\%$

The branching ratios for charginos, neutralinos, staus and other particles taking part in the decay chain are the following:

- $BR(\tilde{\tau} \rightarrow \tilde{\chi}_1^0 \tau) = 100\%$
- $BR(\tilde{\chi}_2^0 \rightarrow \tilde{\tau} \tau) = 100\%$
- $BR(\tilde{\chi}_1^\pm \rightarrow \tilde{\tau} \nu) = 92\%$
- $BR(\tilde{\chi}_1^\pm \rightarrow \tilde{\chi}_1^0 W) = 8\%$
- $BR(W \rightarrow \tau \nu) = 11\%$  [10]
- $BR(W \rightarrow invisible) = 1.4\%$  [10]
- $BR(\tau_{hadronic}) = 65\%$  [10]

Using these branching ratios one can calculate the theoretically expected event yield for events with a single tau, exactly two taus and more than two taus in the final state

---

<sup>1</sup>Production cross-sections are scaled by a filter efficiency

for the di-tau analysis. In the following the branching ratio to heavy gauginos will be neglected ( $BF(other) < 1\%$ ).

$$\begin{aligned}
BF(> \tau\tau) &= BF(\tilde{\chi}_2^0 \tilde{\chi}_1^\pm) \cdot BF(\tilde{\chi}_2^0 \rightarrow \tilde{\tau}\tau) \cdot (BF(\tilde{\chi}_1^\pm \rightarrow \tilde{\tau}\nu) \cdot BF(\tilde{\tau} \rightarrow \tilde{\chi}_1^0 \tau)^3 \\
&\quad \cdot BF(\tau_{hadronic})^3 + BF(\tilde{\chi}_1^\pm \rightarrow \tilde{\chi}_1^0 W) \cdot BF(W \rightarrow \tau\nu) \\
&\quad \cdot BF(\tilde{\tau} \rightarrow \tilde{\chi}_1^0 \tau)^2 \cdot BF(\tau_{hadronic})^3) \\
&= 13.80\% \\
BF(\tau\tau) &= BF(\tilde{\chi}_2^0 \tilde{\chi}_1^\pm) \cdot BF(\tilde{\chi}_2^0 \rightarrow \tilde{\tau}\tau) \cdot BF(\tau_{hadronic})^2 \cdot BF(\tilde{\chi}_1^\pm \rightarrow \tilde{\chi}_2^0 W) \\
&\quad \cdot BF(W \rightarrow invisible) + BF(\tilde{\tau}\tilde{\tau}) \cdot BF(\tilde{\tau} \rightarrow \tilde{\chi}_1^0 \tau)^2 \cdot BF(\tau_{hadronic})^2 \\
&\quad + BF(\tilde{\chi}_1^+ \tilde{\chi}_1^-) \cdot (BF(\tilde{\chi}_1^\pm \rightarrow \tilde{\tau}\nu)^2 \cdot BF(\tilde{\tau} \rightarrow \tilde{\chi}_1^0 \tau)^2 \cdot BF(\tau_{hadronic})^2 \\
&\quad + 2BF(\tilde{\chi}_1^\pm \rightarrow \tilde{\tau}\nu) \cdot BF(\tilde{\chi}_1^\pm \rightarrow \tilde{\chi}_1^0 W) \cdot BF(\tilde{\tau} \rightarrow \tilde{\chi}_1^0 \tau) \cdot BF(W \rightarrow \tau\nu) \\
&\quad \cdot BF(\tau_{hadronic})^2 + BF(\tilde{\chi}_1^\pm \rightarrow \tilde{\chi}_1^0 W)^2 \cdot BF(W \rightarrow \tau\nu)^2 \cdot BF(\tau_{hadronic})^2) \\
&= 17.16\% \\
BF(\tau) &= 0\%
\end{aligned}$$

In Figures 6.6, 6.7 and 6.8 the ratio of events with exactly one tau, exactly two taus and more than two taus in the final state are shown.

The branching ratios for the signal point for which the branching ratios were computed earlier are as expected. Events including hadronic taus only account to  $\sim 31\%$  of all events. The rest of the events contains leptonically decaying taus or/and additional leptons. Different analyses cover these decay modes.

- $BR(> \tau\tau) = 17\%$
- $BR(\tau\tau) = 13\%$
- $BR(\tau) = 1\%$

The branching fraction of 1 % to final states with a single tau is due to the non-zero branching fraction to heavy charginos and neutralinos which was neglected in the previous calculation.

Overall the number of events with a final state with more than two taus ( $> \tau\tau$ ) exceeds the number of events with exactly two taus throughout the whole grid. This is mainly due to  $\tilde{\chi}_2^0 \tilde{\chi}_1^\pm$  production. Therefore it is a promising option to include events with more than two taus in the di-tau analysis.

The number of events with exactly one tau is very small compared to the other channels throughout most of the grid. Only for very low  $\mu$  values the event yields are comparable. This is due to the fact that in this region of the parameter space the relative production cross-section for heavy charginos and neutralinos is significantly large. Heavy charginos and neutralinos lead to mostly final states with additional leptons and jets which are vetoed in this analysis. Therefore decays such as  $\tilde{\chi}_1^0 \tilde{\chi}_2^\pm \rightarrow \tilde{\chi}_1^0 \tilde{\chi}_1^0 W \rightarrow \tilde{\chi}_1^0 \tilde{\chi}_1^0 \tau\nu$  have a relatively large contribution.

However looking at the whole grid it is not desirable to include single tau events in the di-tau analysis because the event yield is quite small compared to the event yield for the channel with exactly two taus and to the event yield for the channel with more than two taus ( $> \tau\tau$ ). In addition the SM background will increase significantly due to i.e  $W \rightarrow \tau\nu$  events. Furthermore a single tau trigger with a reasonable  $p_T$  threshold is not available yet.

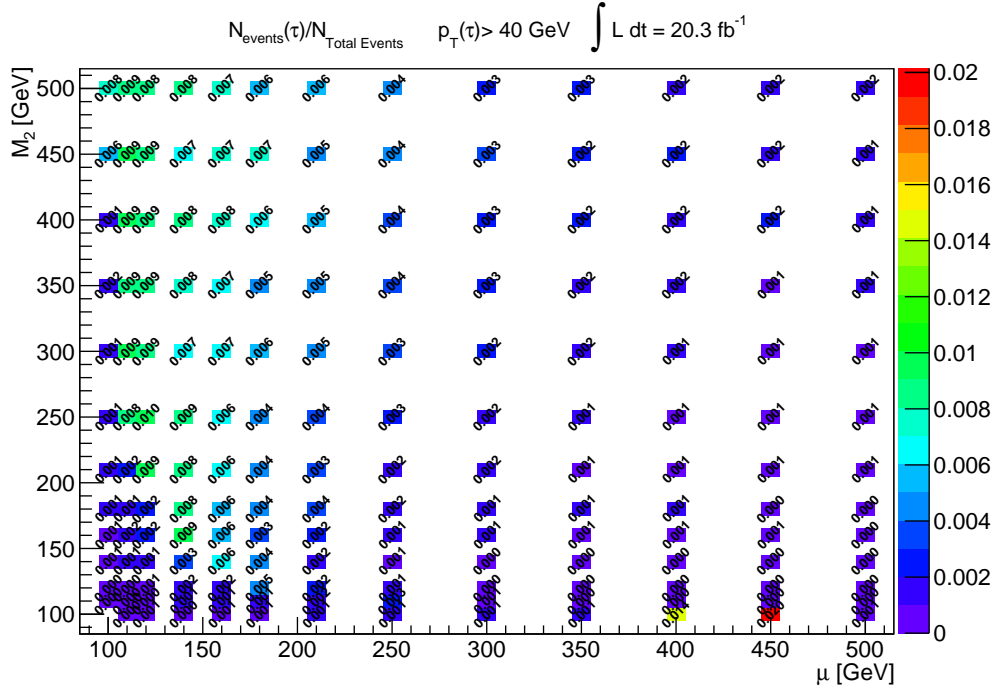


Fig. 6.6: Number of events with a single tau in the final state relative to the total number of events in the signal region. Only taus with  $p_T > 40 \text{ GeV}$  are selected.

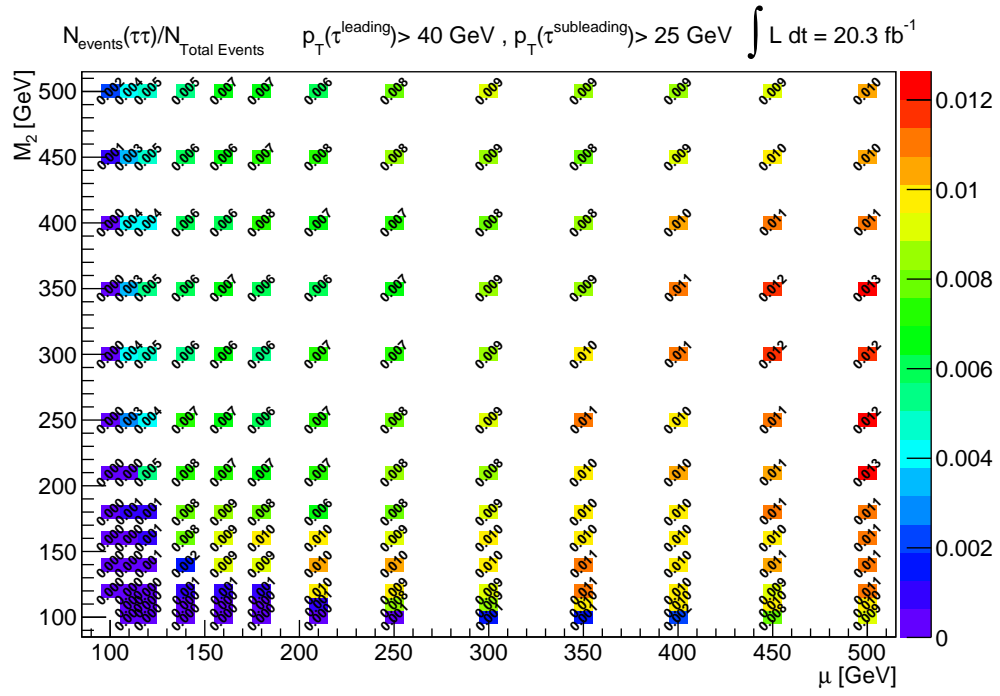


Fig. 6.7: Number of events with exactly two taus in the final state relative to the total number of events in the signal region. The leading tau has  $p_T > 40$  GeV and the subleading tau has to have  $p_T > 25$  GeV.

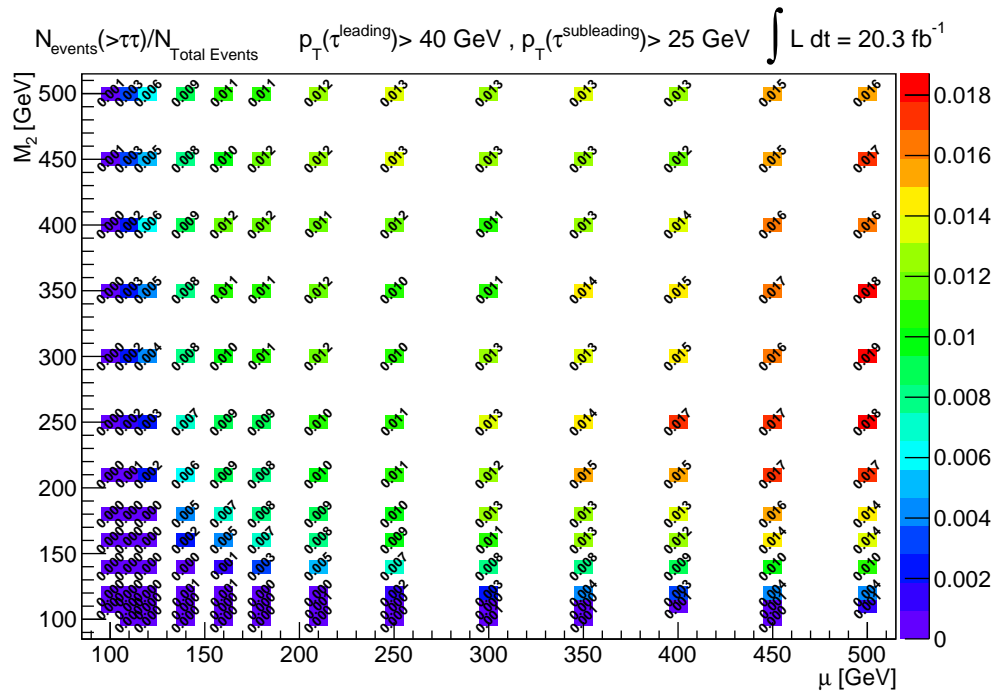


Fig. 6.8: Number of events with more than two taus in the final state relative to the total number of events in the signal region. The leading tau has  $p_T > 40$  GeV and all other taus have to have  $p_T > 25$  GeV.

## 6.2 Trigger thresholds

Another possibility to increase the signal event yield in the  $\tau\tau$  region is to lower the  $p_T$  thresholds in events triggered by the di-tau trigger EF\_tau29Ti\_medium1\_tau20Ti\_medium1. The setting used in the analysis is  $p_T(\tau^{leading}) > 40$  GeV and  $p_T(\tau^{subleading}) > 25$  GeV. Using these  $p_T$  thresholds the di-tau trigger is operated in the plateau region [24]. However one could lower the requirements and work in the so called turn-on region of the trigger. This means parametrising the trigger efficiency as a function of  $p_T$ . In Figure 6.7, 6.9 and 6.10 the relative event yields of events with final states with exactly two taus with  $p_T$  thresholds (40,25) GeV, (30,20) GeV and (20,20) GeV are shown. Using a lower  $p_T$  threshold of (30,20) GeV increases the event yield by 1-7 % throughout the grid compared to the event yields with (40,25) GeV threshold. However the SM background contribution increases by  $\sim 20\%$ . Lowering the  $p_T$  thresholds to (20,20) GeV increases the event yield by an additional 1-6 % but the increase of the SM background contribution is larger. In conclusion the use of lower  $p_T$  thresholds is not a feasible option to improve the sensitivity of the analysis.

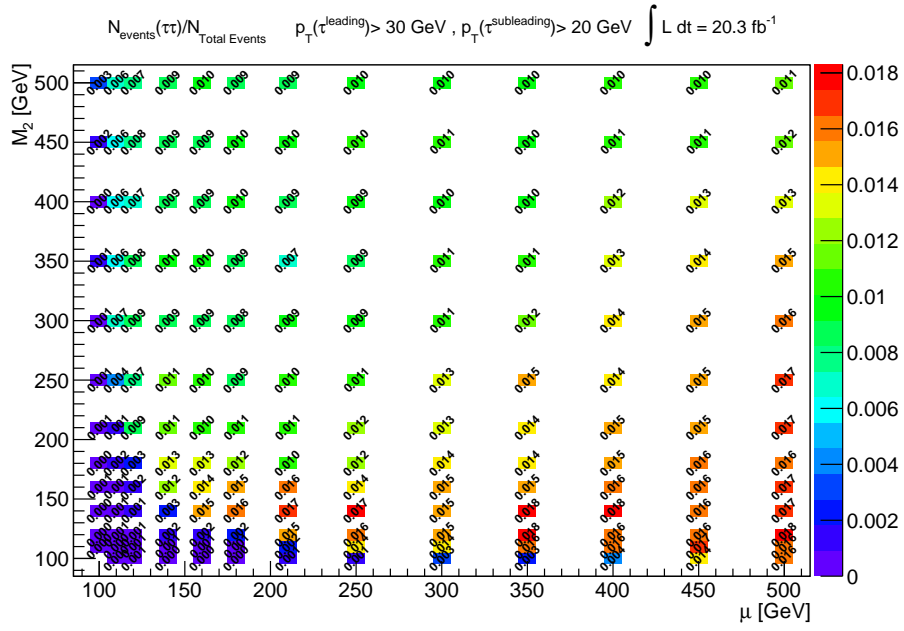


Fig. 6.9: Number of events with exactly two taus in the final state relative to the total number of events in the signal region. The leading tau has  $p_T > 30$  GeV and the subleading tau has to have  $p_T > 20$  GeV.

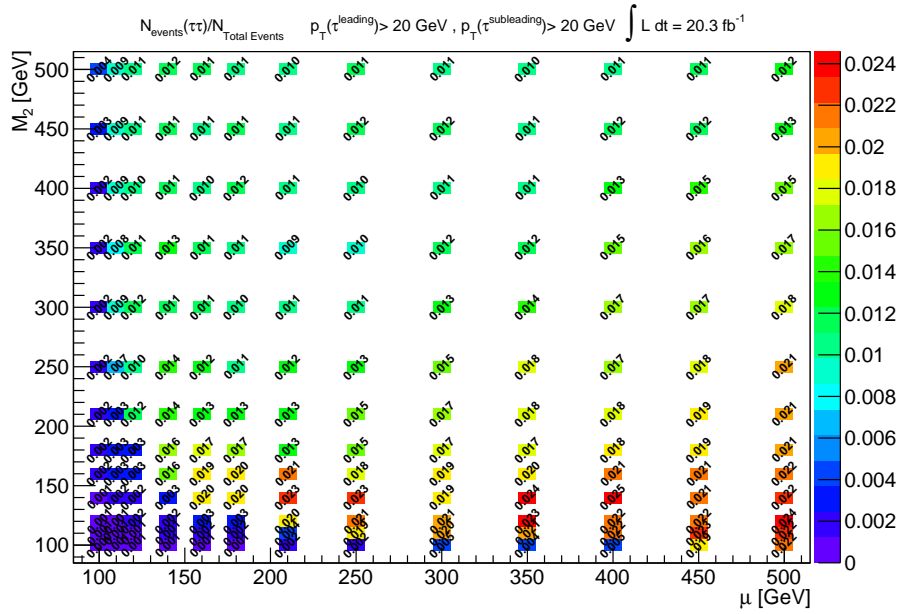


Fig. 6.10: Number of events with exactly two taus in the final state relative to the total number of events in the signal region. The leading tau has  $p_T > 20$  GeV and the subleading tau has to have  $p_T > 20$  GeV.



---

# CHAPTER 7

## Conclusion and Outlook

In this thesis two different studies have been presented. In chapter 5 an analysis for the search for direct stau production in  $p$ - $p$  collisions with a center-of-mass collision energy  $\sqrt{s} = 8$  TeV at the LHC has been presented. The SUSY model under consideration was the pMSSM including R-parity conservation.

The analysis is not sensitive to the process of direct stau production. The analysis reaches the best sensitivity for direct stau production in the pMSSM at the mass point ( $m_{\tilde{\tau}} = 100$  GeV,  $m_{\tilde{\chi}_0} = 20$  GeV). The upper limit on the cross-section for direct stau production that cannot be excluded is in this case  $\sigma/\sigma_{SUSY} = 3.65$  with  $\sigma_{SUSY} = 131.16$  fb (NLO).

Including a systematic uncertainty of 30% on the background estimate the upper limit in this case becomes  $\sigma/\sigma_{SUSY} = 5.68$ .

One promising approach for the search for direct stau production was a multivariant analysis (MVA) which has been carried out inside the ATLAS collaboration but was also not sensitive. As the production cross-section for direct stau production will increase for higher center-of-mass collision energy an analysis for direct stau production might be sensitive for  $p$ - $p$  collisions at  $\sqrt{s} = 14$  TeV and higher integrated luminosity.

In chapter 6 two studies have been presented which aimed to improve the sensitivity of a di-tau analysis for the search for electroweak direct gaugino and direct stau production in the framework of the pMSSM. It has been found that it is not feasible to use lower  $p_T$  thresholds for the di-tau trigger EF\_tau29Ti\_medium1\_tau20Ti\_medium1 as the SM background increase is significantly larger than that of the SUSY signal event yield throughout the pMSSM grid under study.

Furthermore it has been found that the selection of events with more than two taus in addition to events with exactly two taus is promising to improve the sensitivity of the analysis.

As a result of these studies the ATLAS di-tau analysis was extended to select events with at least two hadronically decaying taus in the final state [24]<sup>1</sup>.

---

<sup>1</sup>The analysis achieved to exclude chargino masses up to 350 GeV for a massless lightest neutralino in simplified models for a scenario of direct production of wino-like chargino pairs decaying into the lightest neutralino via an intermediate on-shell stau. Furthermore masses up to 330 (300) GeV are excluded for lightest neutralino masses below 50 (100) GeV for pair production of degenerate charginos and next-to-lightest neutralinos [24].

# APPENDIX A

## Variable Distributions in the OS region

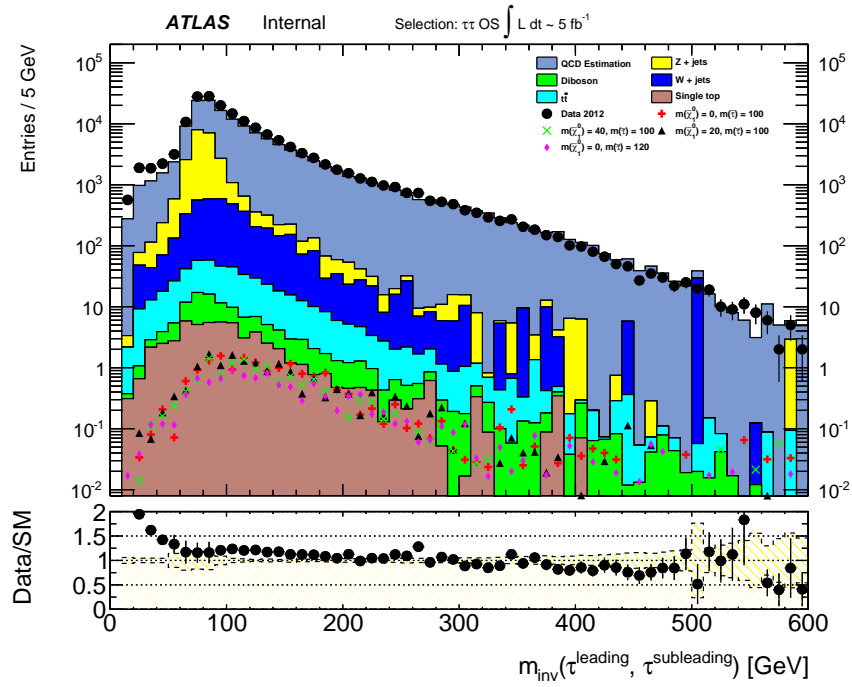


Fig. A.1: Distribution of  $m(\tau, \tau)$  in the OS region.

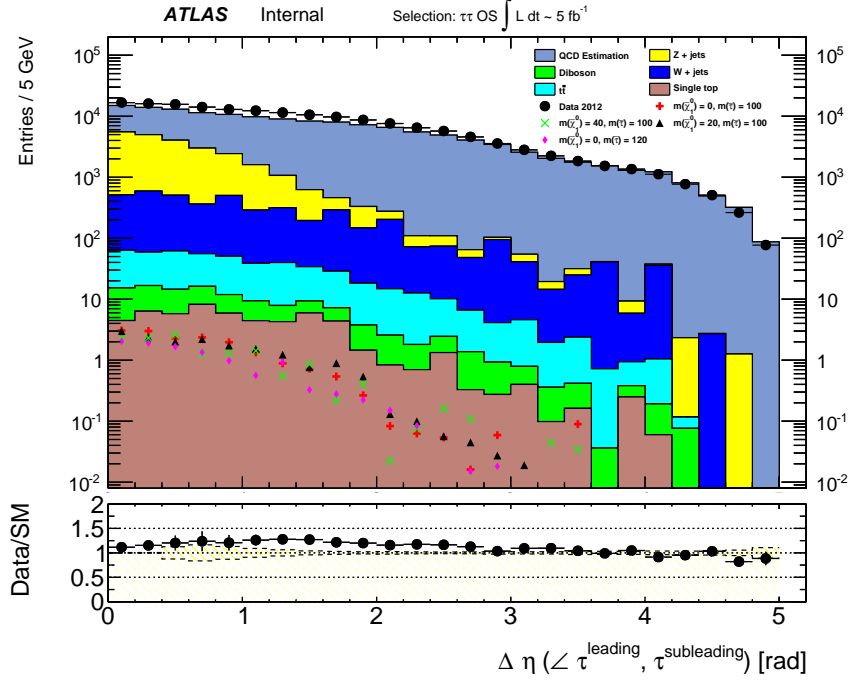


Fig. A.2: Distribution of  $\Delta\eta(\tau, \tau)$  in the OS region.

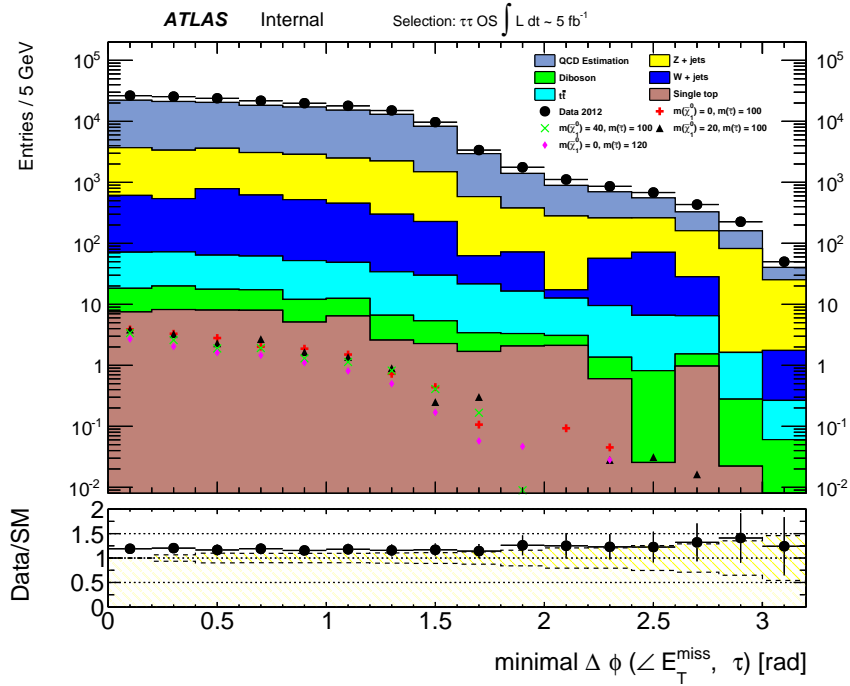


Fig. A.3: Distribution of  $\min.(\Delta\phi(\angle E_T^{\text{miss}}, \tau))$  in the OS region.

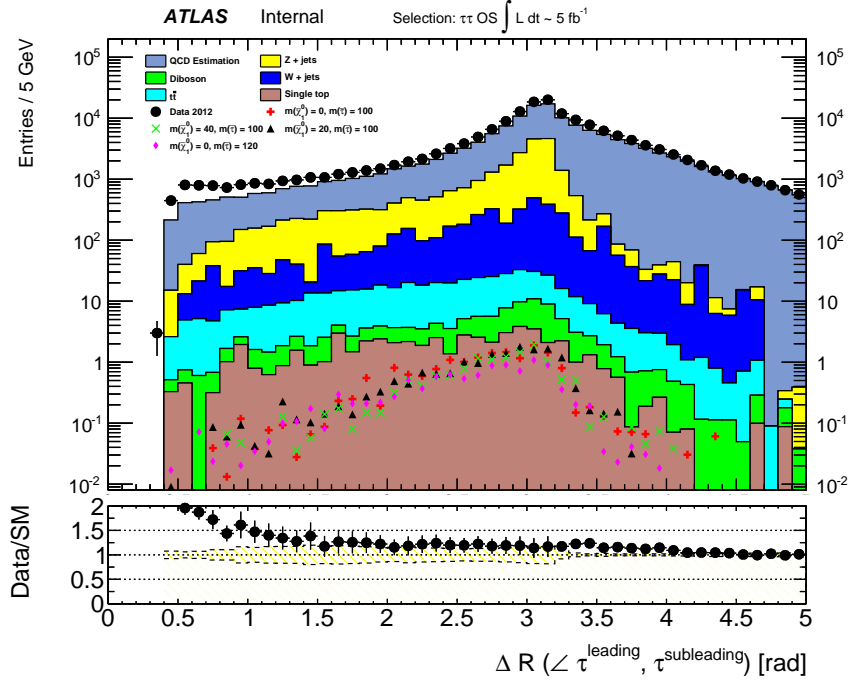


Fig. A.4: Distribution of  $\Delta R(\tau, \tau)$  in the OS region.

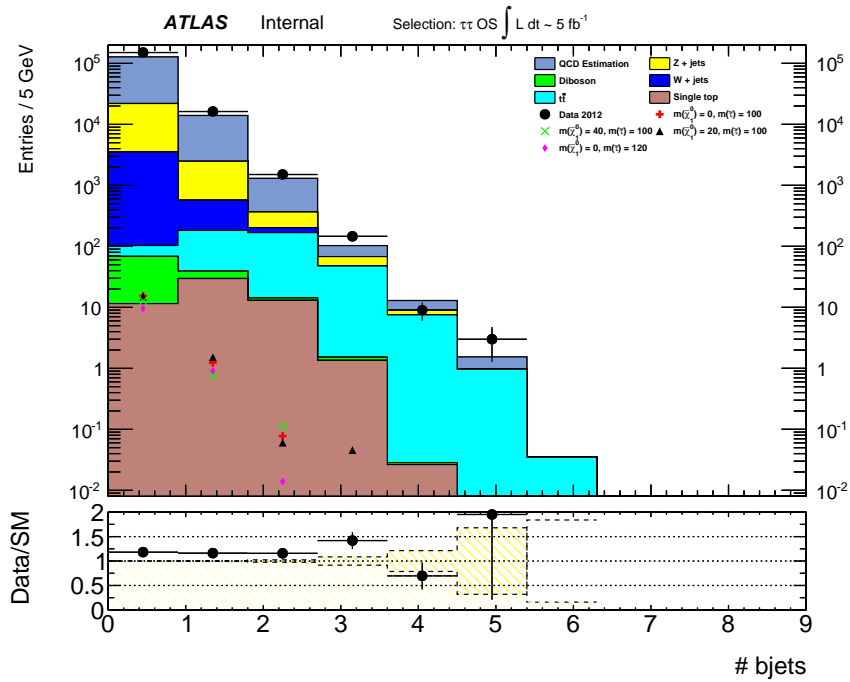


Fig. A.5: Distribution of the number of b-jets in the OS region.

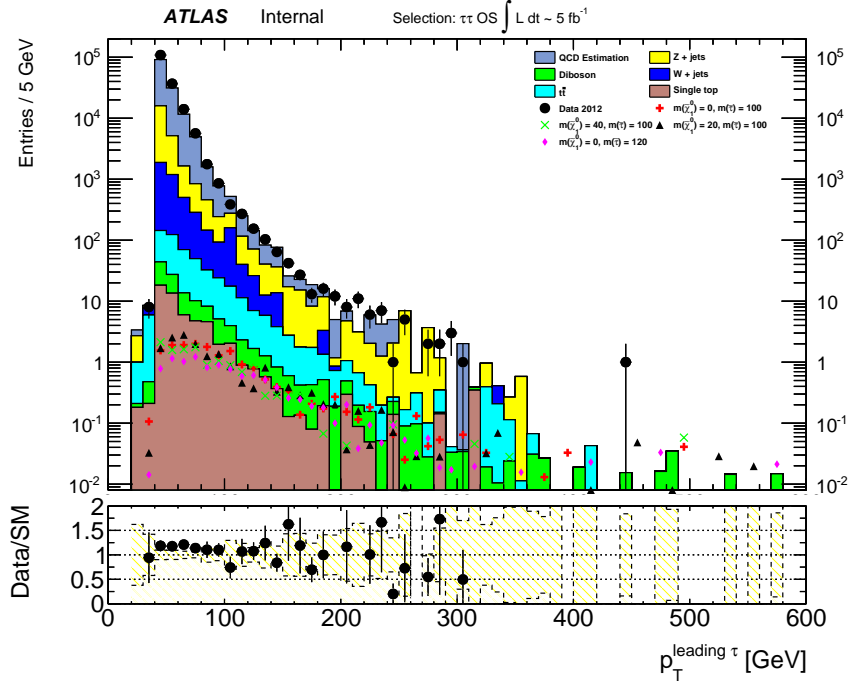


Fig. A.6: Distribution of  $p_T(\tau^{leading})$  in the OS region.

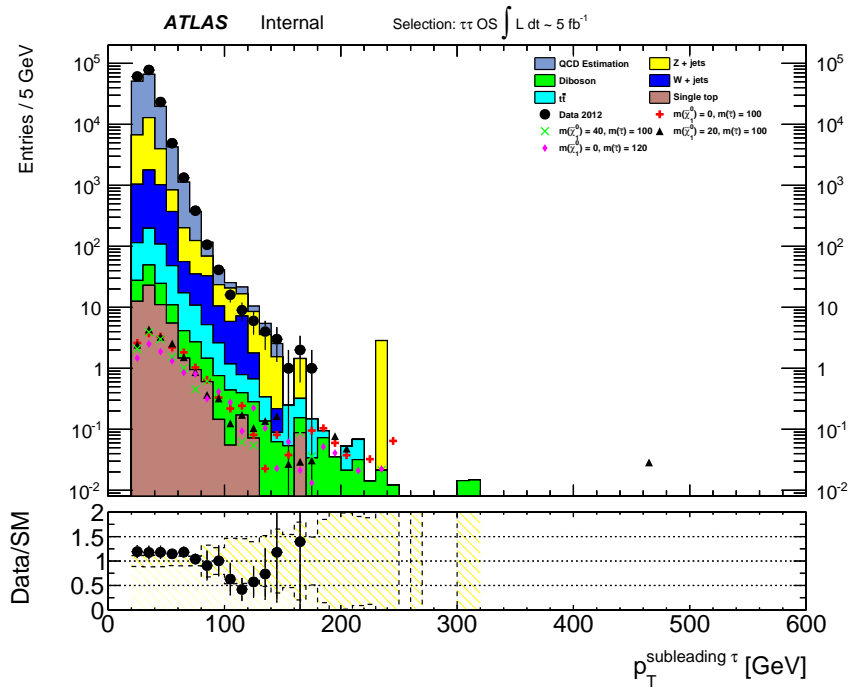


Fig. A.7: Distribution of  $p_T(\tau^{subleading})$  in the OS region.

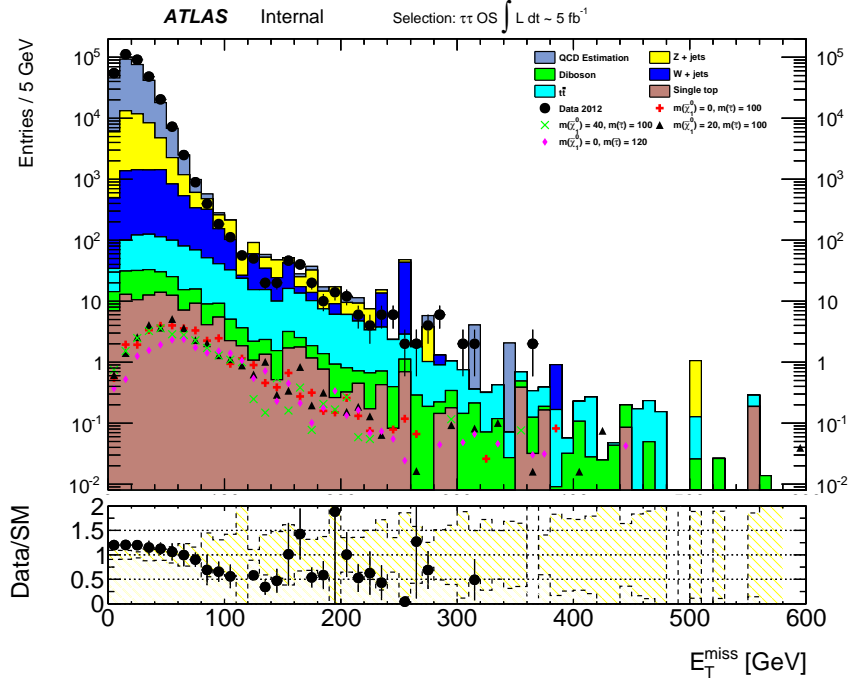


Fig. A.8: Distribution of  $E_T^{\text{miss}}$  in the OS region.

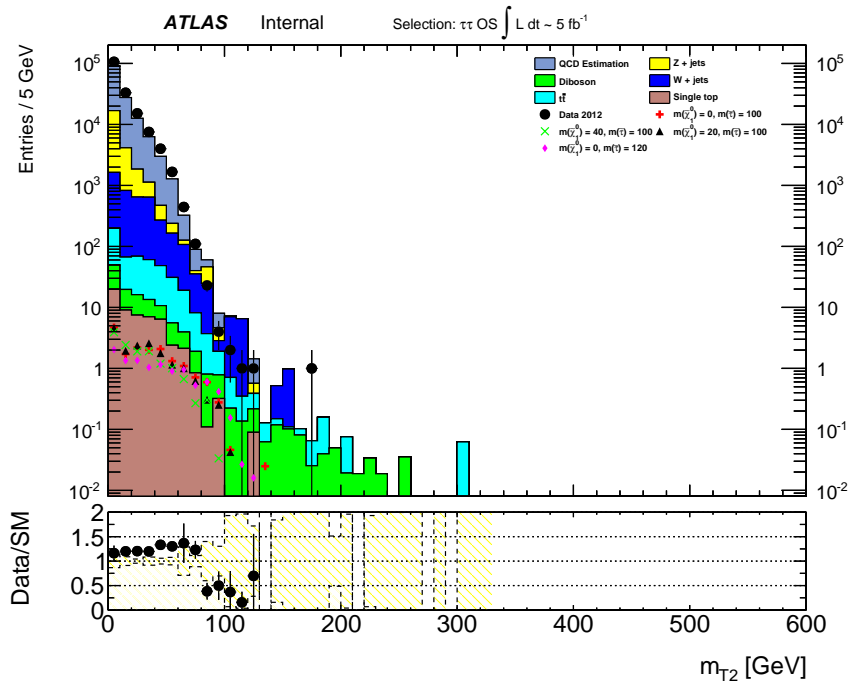


Fig. A.9: Distribution of  $m_{t_2}$  in the OS region.

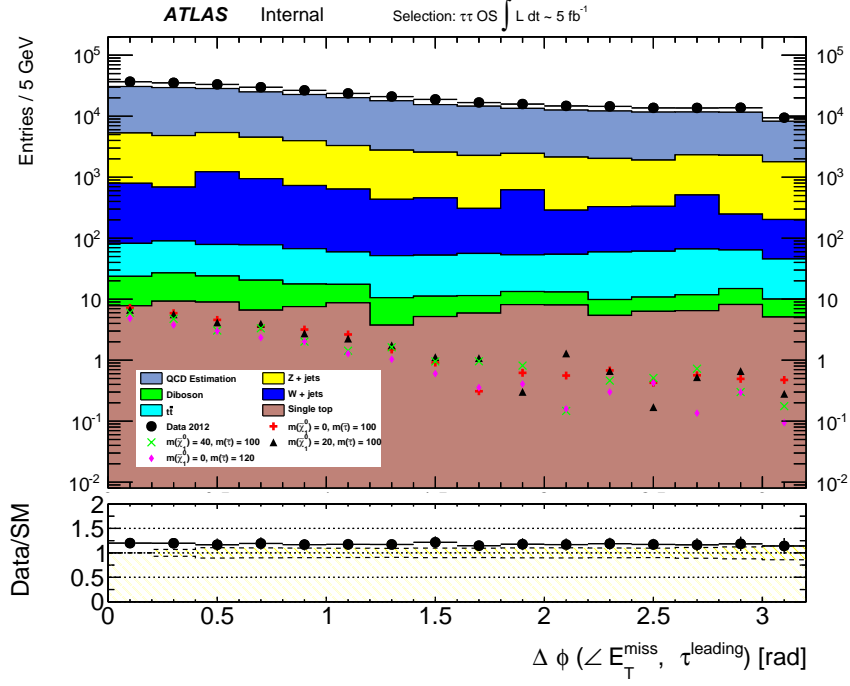


Fig. A.10: Distribution of  $(\Delta\phi(\angle E_T^{\text{miss}}, \tau^{\text{leading}}))$  in the OS region.

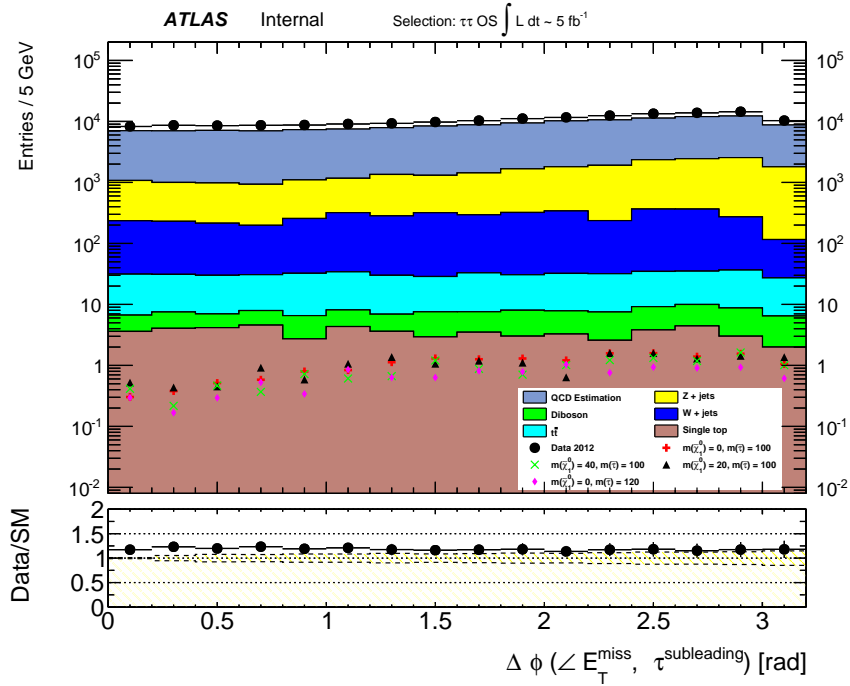


Fig. A.11: Distribution of  $(\Delta\phi(\angle E_T^{\text{miss}}, \tau^{\text{subleading}}))$  in the OS region.

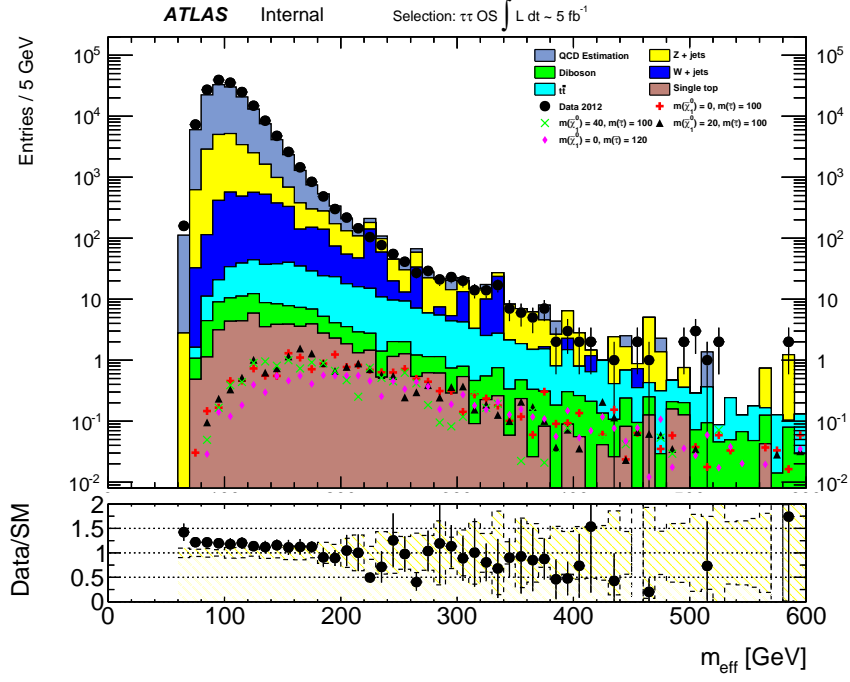


Fig. A.12: Distribution of  $m_{\text{eff}}$  in the OS region.

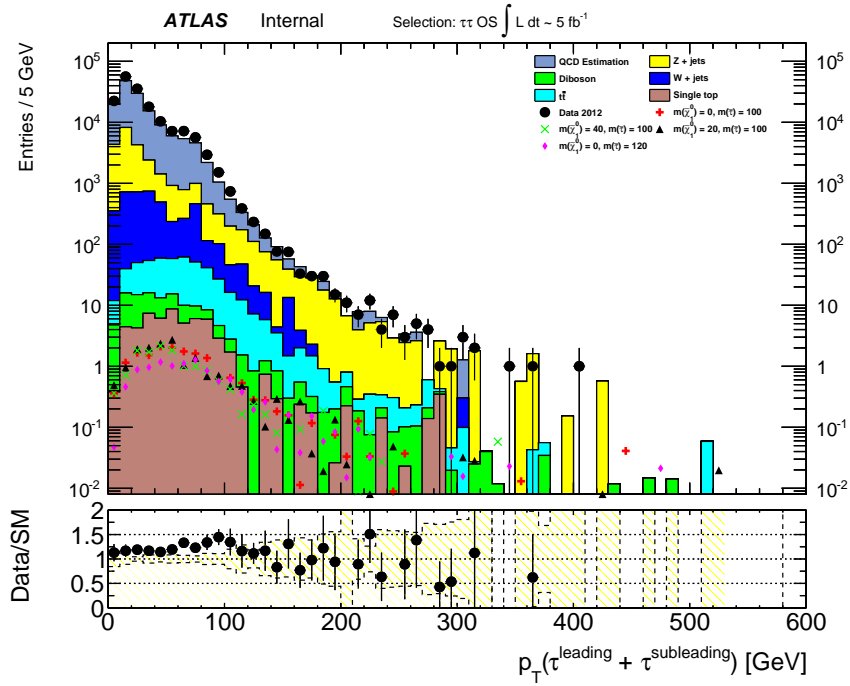


Fig. A.13: Distribution of  $p_T(\tau^{\text{leading}} + \tau^{\text{subleading}})$  in the OS region.



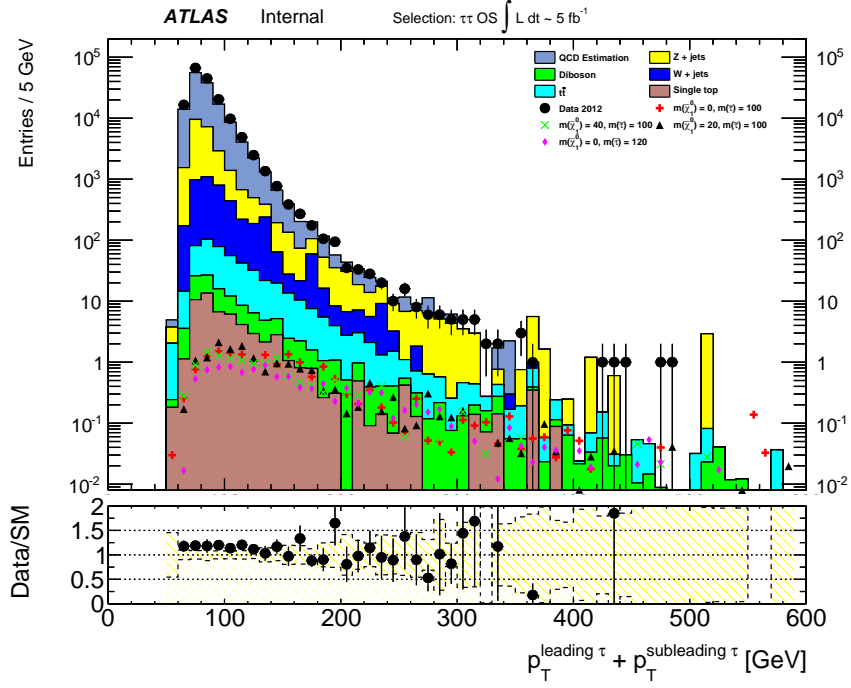


Fig. A.14: Distribution of  $p_T(\tau^{\text{leading}}) + p_T(\tau^{\text{subleading}})$  in the OS region.

# APPENDIX B

## Variable Distributions in the OS+Preselection region

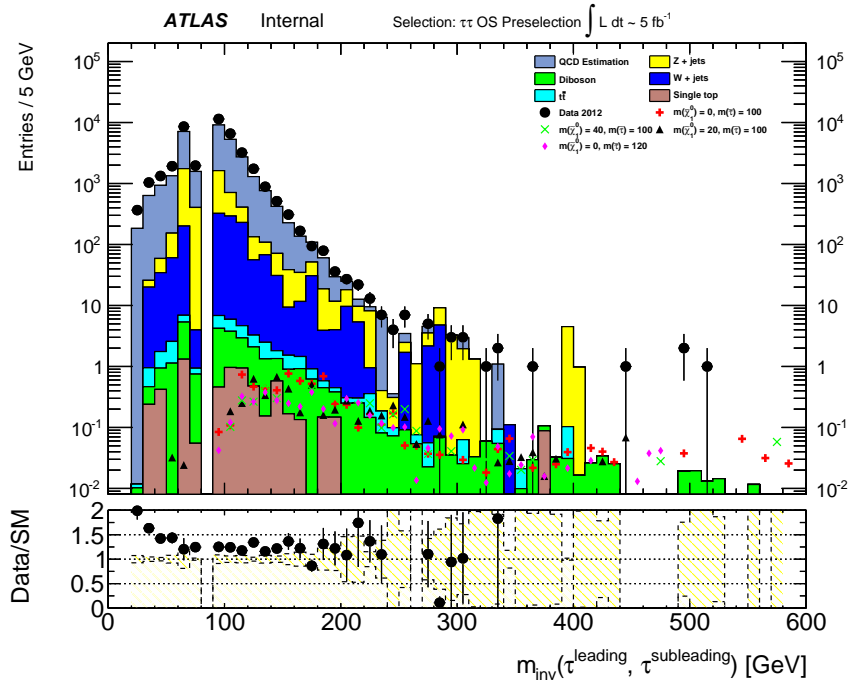


Fig. B.1: Distribution of  $m(\tau, \tau)$  after the Preselection cuts have been applied.

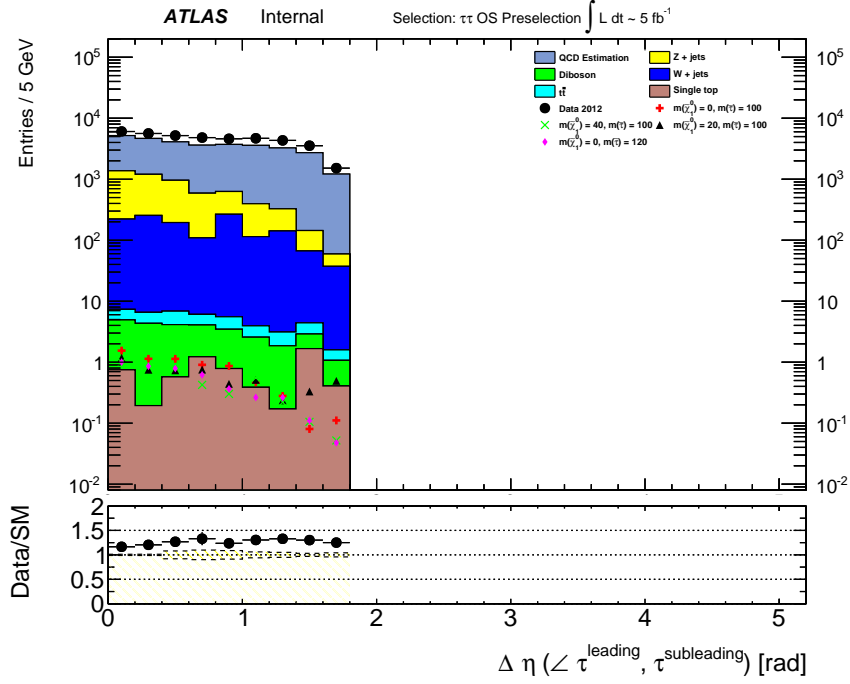


Fig. B.2: Distribution of  $\Delta\eta(\tau, \tau)$  after the Preselection cuts have been applied.

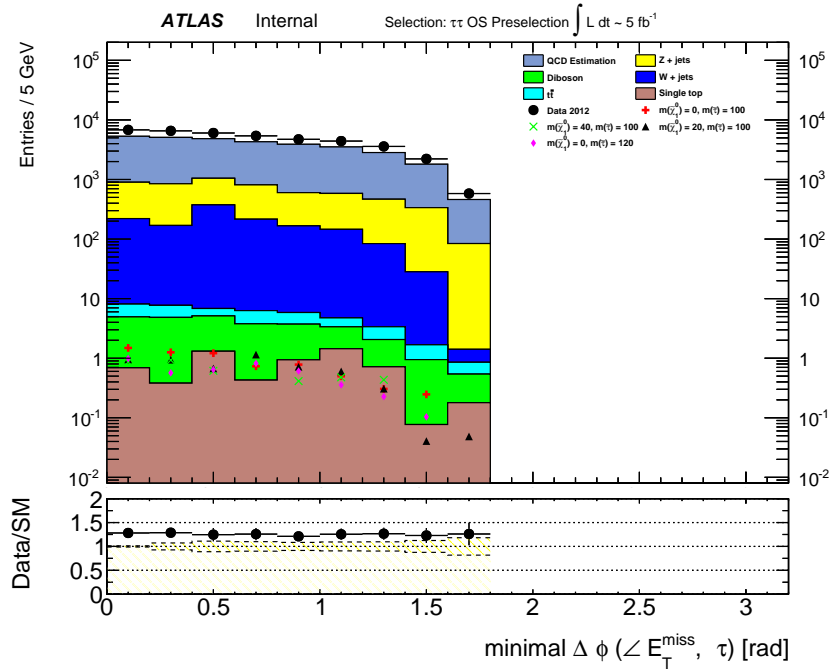


Fig. B.3: Distribution of  $\min.(\Delta\phi(\angle E_T^{\text{miss}}, \tau))$  after the Preselection cuts have been applied.

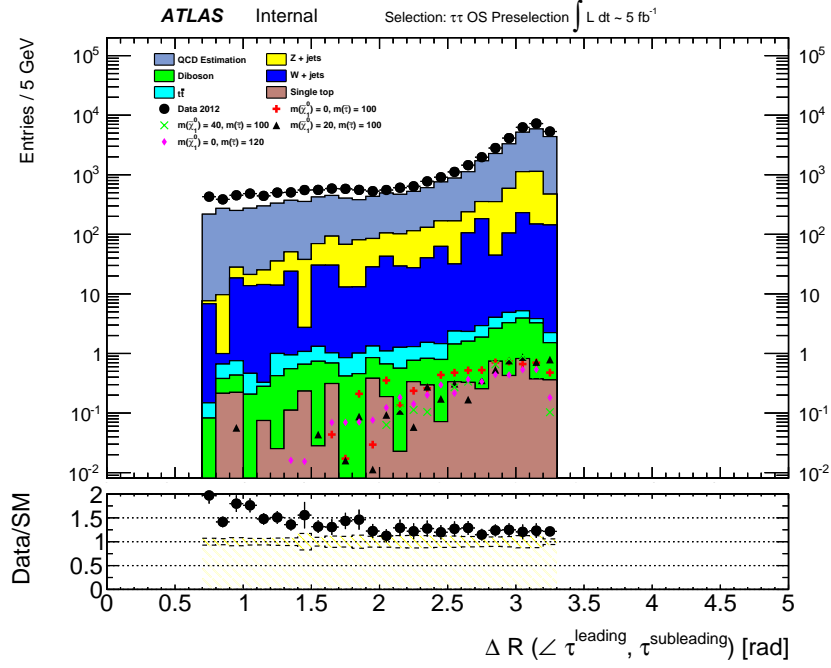


Fig. B.4: Distribution of  $\Delta R(\tau, \tau)$  after the Preselection cuts have been applied.

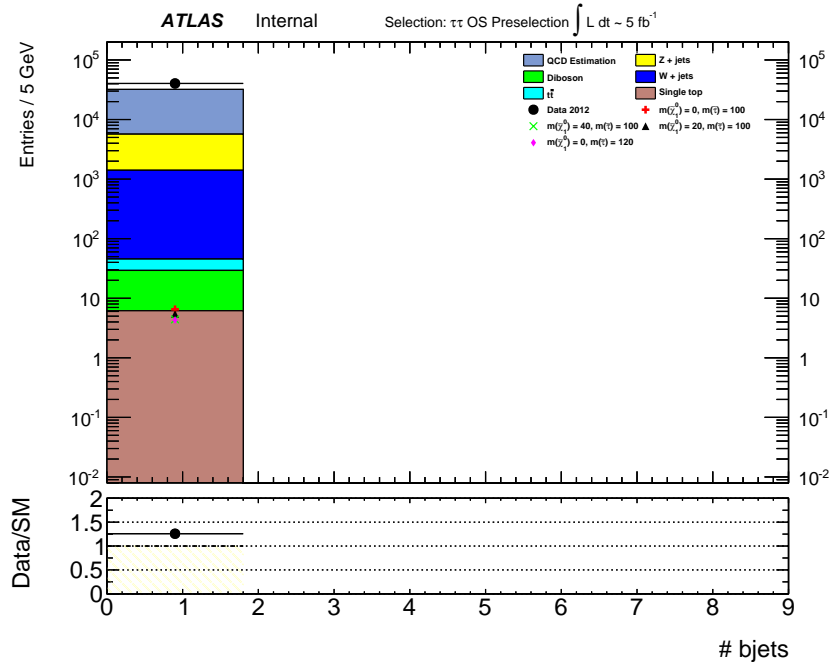


Fig. B.5: Distribution of the number of b-jets after the Preselection cuts have been applied.

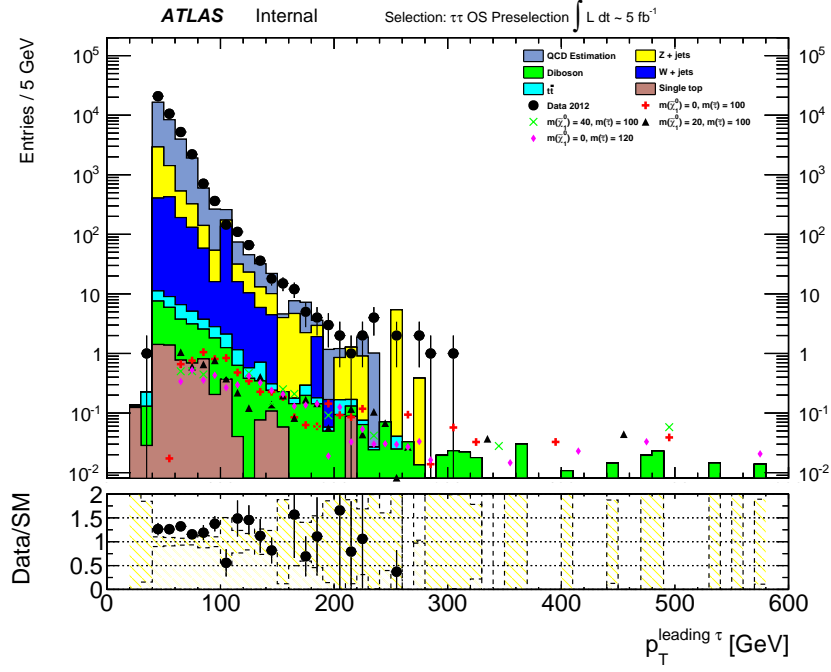


Fig. B.6: Distribution of  $p_T(\tau^{\text{leading}})$  after the Preselection cuts have been applied.

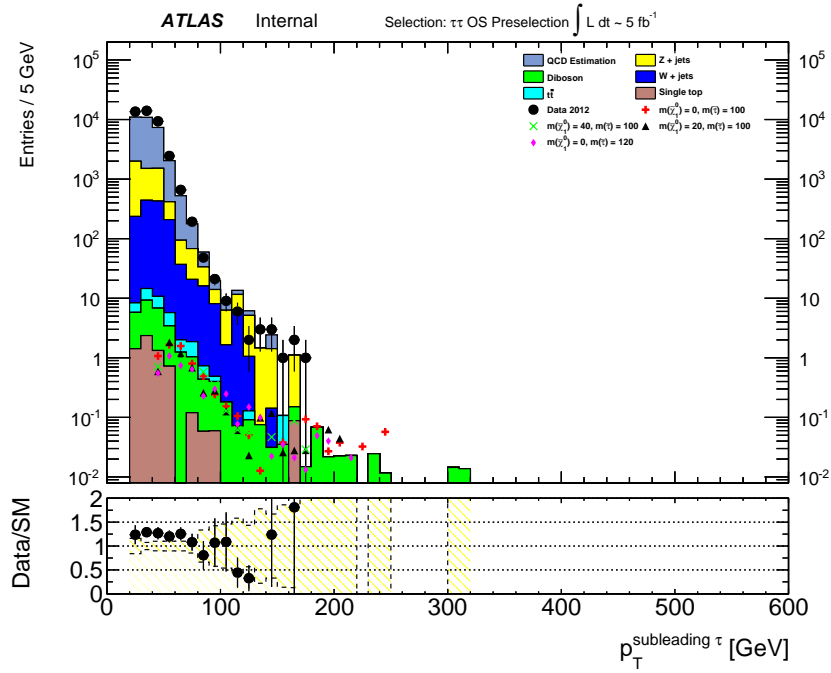


Fig. B.7: Distribution of  $p_T(\tau^{\text{subleading}})$  after the Preselection cuts have been applied.

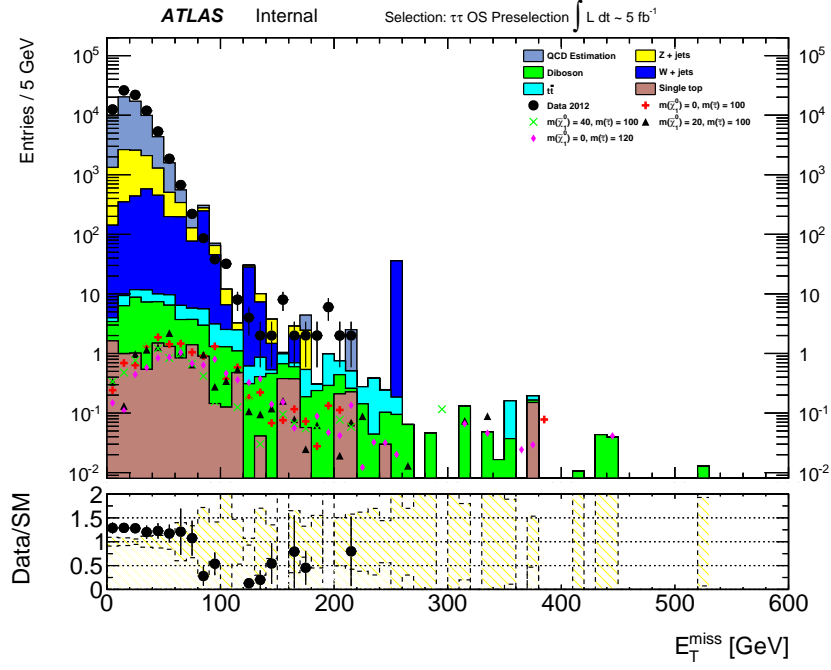


Fig. B.8: Distribution of  $E_T^{\text{miss}}$  after the Preselection cuts have been applied.

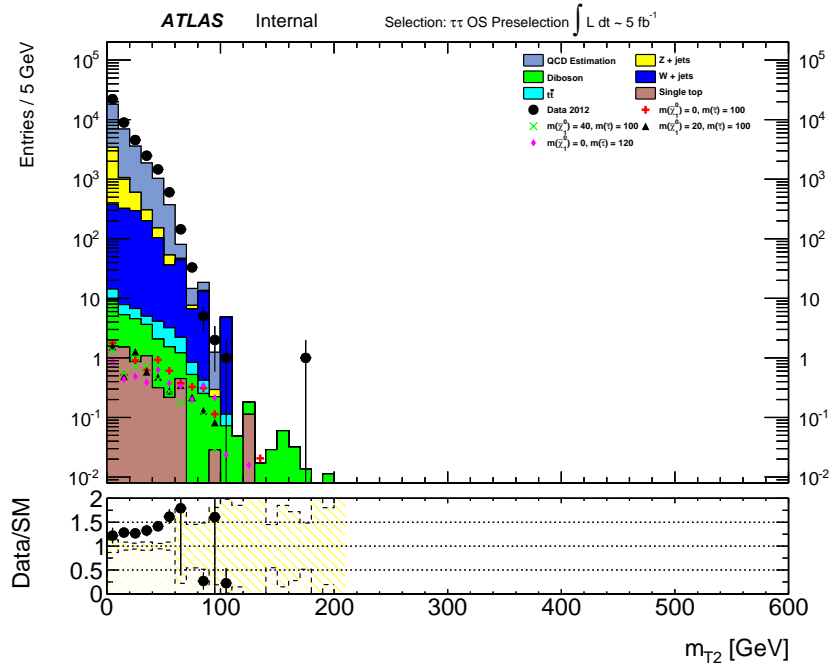


Fig. B.9: Distribution of  $m_{t2}$  after the Preselection cuts have been applied.

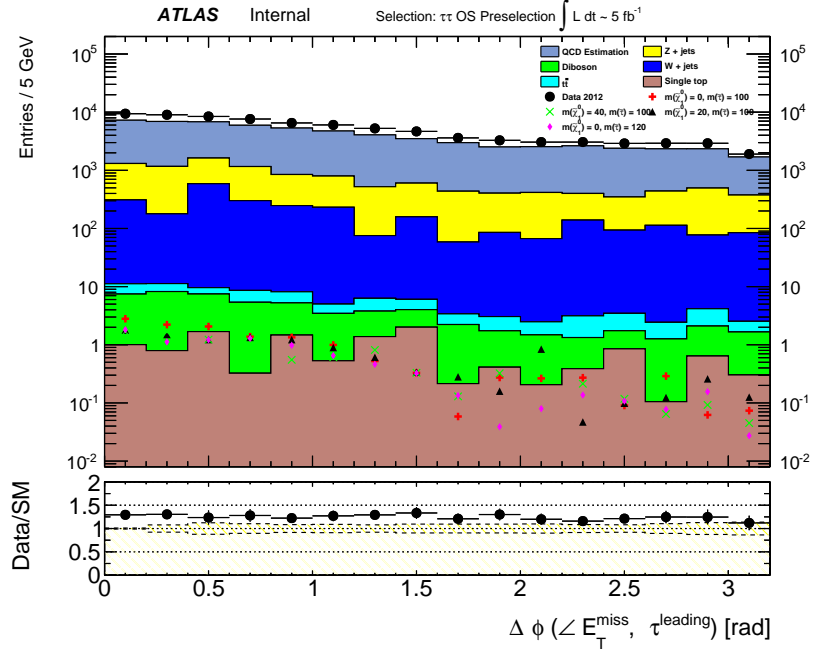


Fig. B.10: Distribution of  $(\Delta\phi(\langle E_T^{miss}, \tau^{leading} \rangle))$  after the Preselection cuts have been applied.

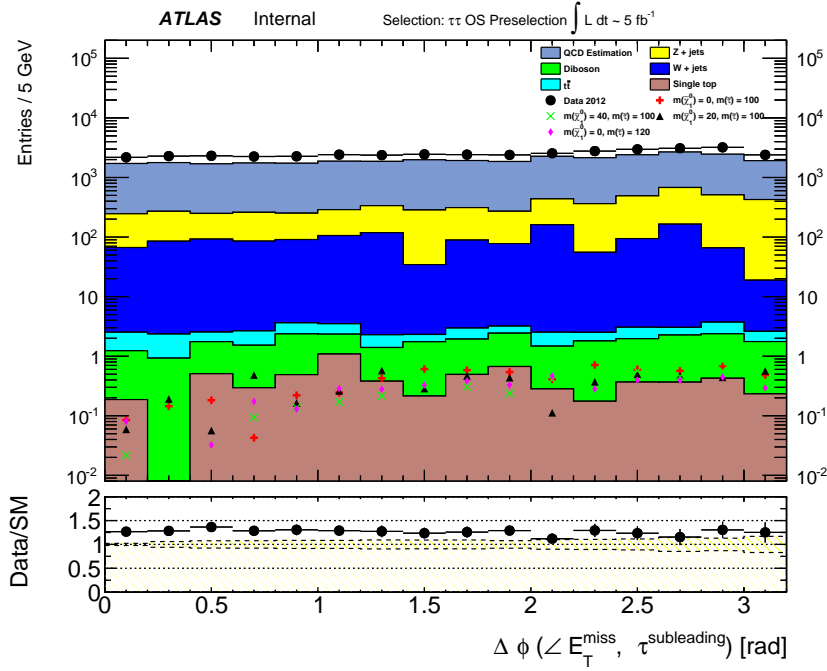


Fig. B.11: Distribution of  $(\Delta\phi(\langle E_T^{miss}, \tau^{subleading} \rangle))$  after the Preselection cuts have been applied.

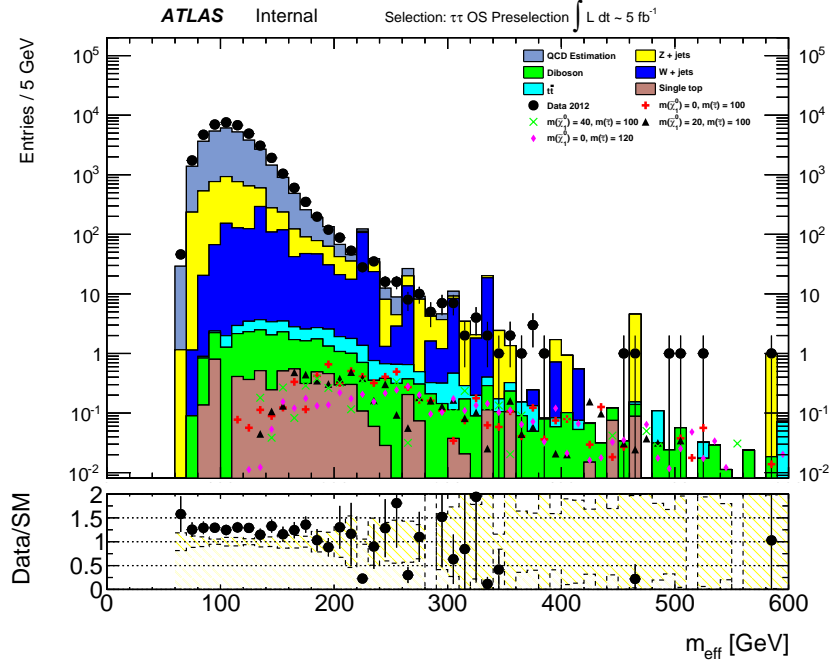


Fig. B.12: Distribution of  $m_{eff}$  after the Preselection cuts have been applied.

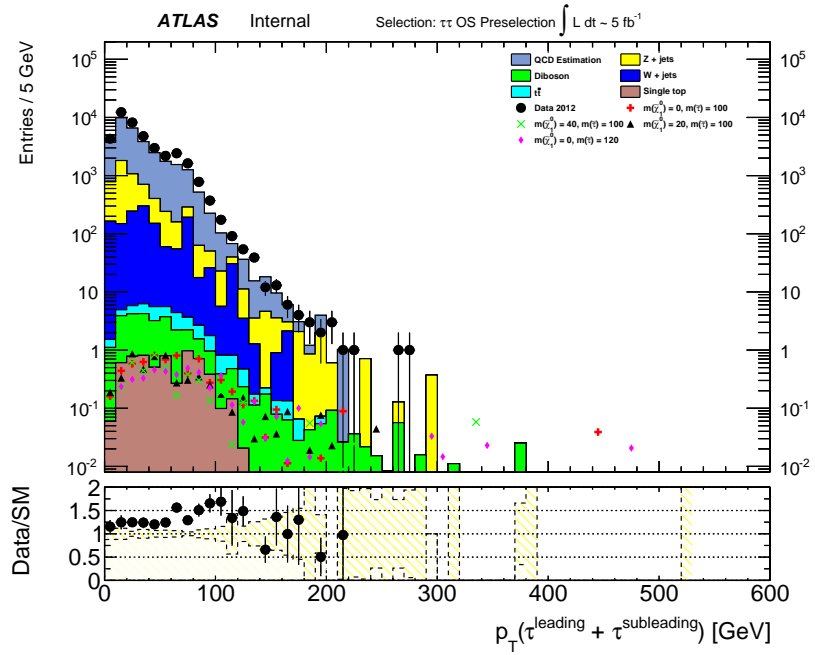


Fig. B.13: Distribution of  $p_T(\tau^{leading} + \tau^{subleading})$  after the Preselection cuts have been applied.



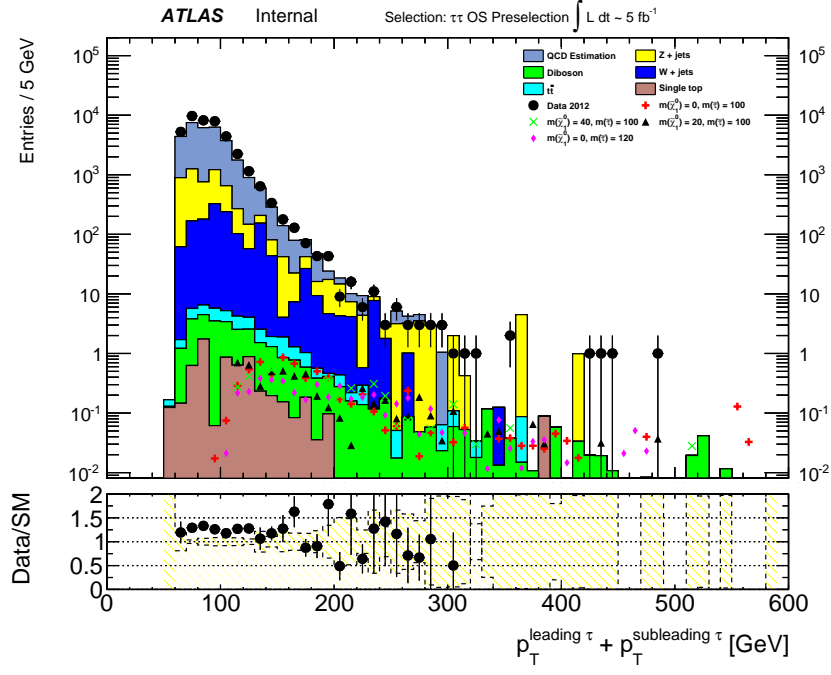


Fig. B.14: Distribution of  $p_T(\tau^{\text{leading}}) + p_T(\tau^{\text{subleading}})$  after the Preselection cuts have been applied.

---

# Bibliography

- [1] THE ATLAS COLLABORATION: A particle consistent with the Higgs Boson observed with the ATLAS Detector at the Large Hadron Collider. In: *Science* 338 (2012), S. 1576–1582 [1](#), [5](#), [14](#)
- [2] THE CMS COLLABORATION: Observation of a new boson at a mass of 125 GeV with the CMS experiment at the LHC. In: *Phys.Lett.* B716 (2012), S. 30–61 [1](#), [5](#), [14](#)
- [3] THE ATLAS COLLABORATION: *Search for direct production of charginos and neutralinos in events with three leptons and missing transverse momentum in  $21\text{fb}^{-1}$  of  $pp$  collisions at  $\sqrt{s} = 8\text{TeV}$  with the ATLAS detector.* Mar 2013. – ATLAS-CONF-2013-035 [2](#)
- [4] THE ATLAS COLLABORATION: Search for direct production of charginos and neutralinos in events with three leptons and missing transverse momentum in  $\sqrt{s} = 7\text{TeV}$   $pp$  collisions with the ATLAS detector. In: *Phys.Lett.* B718 (2013), S. 841–859 [2](#)
- [5] THE ATLAS COLLABORATION: Search for direct slepton and gaugino production in final states with two leptons and missing transverse momentum with the ATLAS detector in  $pp$  collisions at  $\sqrt{s} = 7\text{TeV}$ . In: *Phys.Lett.* B718 (2013), S. 879–901 [2](#)
- [6] THE CMS COLLABORATION: Search for electroweak production of charginos and neutralinos using leptonic final states in  $pp$  collisions at  $\sqrt{s} = 7\text{TeV}$ . In: *JHEP* 1211 (2012), S. 147 [2](#)
- [7] BETHGE, K. ; SCHRÖDER, U.E.: *Elementarteilchen und ihre Wechselwirkungen.* Wiley-vch, 2006 [3](#)
- [8] GRIFFITHS, D.: *Introduction to Elementary Particle Physics.* Wiley-vch, 2009 [3](#)
- [9] SCHROEDER, D.V. ; PESKIN, M.E.: *An Introduction to Quantum Field Theory.* Addison-Wesley, 1995 [3](#)
- [10] J. BERINGER ET AL. (PARTICLE DATA GROUP): Review of Particle Physics. In: *Phys. Rev.* D86 010001 (2012), S. 1+ [4](#), [36](#), [38](#), [59](#), [62](#)
- [11] HOWARD BAER, Xerxes T.: *Weak Scale Supersymmetry.* Cambridge, 2006 [5](#)

- [12] LEITCH, Erik M. ; KOVAC, J.M. ; HALVERSON, N.W. ; CARLSTROM, J.E. ; PRYKE, C. u. a.: DASI three-year cosmic microwave background polarization results. In: *Astrophys.J.* 624 (2005), S. 10–20 [5](#)
- [13] MELCHIORRI, A. ; ADE, P. A. R. ; BERNARDIS, P. de ; BOCK, J. J. ; BORRILL, J. ; BOSCALERI, A. ; CRILL, B. P. ; TROIA, G. D. ; FARESE, P. ; FERREIRA, P. G. ; GANGA, K. ; GASPERIS, G. de ; GIACOMETTI, M. ; HRISTOV, V. V. ; JAFFE, A. H. ; LANGE, A. E. ; MASI, S. ; MAUSKOPF, P. D. ; MIGLIO, L. ; NETTERFIELD, C. B. ; PASCALE, E. ; PIACENTINI, F. ; ROMEO, G. ; RUHL, J. E. ; VITTORIO, N.: A measurement of Omega from the North American test flight of BOOMERANG. In: *astro-ph/9911445* (1999) [5](#)
- [14] MARKEVITCH, M. ; GONZALEZ, A. H. ; CLOWE, D. ; VIKHLININ, A. ; DAVID, L. ; FORMAN, W. ; JONES, C. ; MURRAY, S. ; TUCKER, W.: Direct constraints on the dark matter self-interaction cross-section from the merging galaxy cluster 1E0657-56. In: *astro-ph/0309303* (2003) [5](#)
- [15] KOWALSKI, M. u. a.: Improved Cosmological Constraints from New, Old and Combined Supernova Datasets. In: *Astrophys.J.* 686 (2008), S. 749–778 [5](#)
- [16] HINSHAW, G. u. a.: Nine-Year Wilkinson Microwave Anisotropy Probe (WMAP) Observations: Cosmological Parameter Results. In: *arXiv* (2012) [5](#)
- [17] KAZAKOV, D I.: Beyond the Standard Model (in Search of Supersymmetry). In: *hep-ph/0012288* (2001) [6](#)
- [18] MARTIN, Stephen P.: A Supersymmetry primer. In: *hep-ph/9709356* (1997) [6](#), [12](#)
- [19] R. ARNOWITT, A. H. C. ; NATH, Pran: The Development of Supergravity Grand Unification: Circa 1982-85. In: *Int.J.Mod.Phys.* (2012). – arXiv:1206.3175 [9](#)
- [20] GIUDICE, G.F. ; RATAZZI, R.: Theories with gauge mediated supersymmetry breaking. In: *Phys.Rept.* 322 (1999), S. 419–499 [9](#)
- [21] RANDALL, Lisa ; SUNDRUM, Raman: Out of this world supersymmetry breaking. In: *Nucl.Phys.* B557 (1999), S. 79–118 [9](#)
- [22] CHACKO, Z. ; LUTY, Markus A. ; NELSON, Ann E. ; PONTON, Eduardo: Gaugino mediated supersymmetry breaking. In: *JHEP* 0001 (2000), S. 003 [9](#)
- [23] PLEHN, T. ; BEENAKKER, W. ; HOEPKER, R. ; KRAEMER, M. ; SPIRA, M. ; ZERWAS, P.: *Prospino graph*. <http://www.thphys.uni-heidelberg.de/~plehn/index.php?show=prospino&visible=tools>, 2013 [11](#), [37](#)
- [24] THE ATLAS COLLABORATION: *Search for electroweak production of supersymmetric particles in final states with at least two hadronically decaying taus and missing transverse momentum with the ATLAS detector in proton-proton collisions at*

- $\sqrt{s} = 8 \text{ TeV}$ . CERN, Geneva, Mar 2013. – ATLAS-CONF-2013-028 [13](#), [29](#), [35](#), [40](#), [66](#), [68](#)
- [25] EVANS, Lyndon ; BRYANT, Philip: LHC Machine. In: *JINST* 3 (2008), S. S08001 [14](#)
- [26] THE ATLAS COLLABORATION: *ATLAS Public Documentation*. <https://twiki.cern.ch/twiki/bin/view/AtlasPublic/LuminosityPublicResults>, 2013 [15](#), [16](#), [35](#)
- [27] NUCLEAR RESEARCH (GENEVA), European O.: *CERN Homepage*. <http://www.cern.ch>, 2013 [15](#)
- [28] THE ATLAS COLLABORATION: The ATLAS Experiment at the CERN Large Hadron Collider. In: *JINST* 3 (2008), S. S08003 [16](#), [27](#), [40](#)
- [29] THE ATLAS COLLABORATION: *The ATLAS factsheet*. 2011 [16](#), [20](#)
- [30] COMMITTEE, LHC E.: *ATLAS: technical proposal for a general-purpose pp experiment at the Large Hadron Collider at CERN*. CERN, Geneva, 1994 [16](#)
- [31] THE ATLAS COLLABORATION: *ATLAS collaboration homepage*. <http://www.atlas.ch>, 2013 [17](#), [20](#), [21](#), [22](#), [24](#)
- [32] LAMPRECHT, Martin: *Studien zu Effizienz und Akzeptanz des ATLAS-Myontriggers mit simulierten Messdaten*, Ludwig-Maximilians-Universität München, Diplomarbeit, 2007 [18](#)
- [33] LHCC, LHC Experiments Committee ;.: *ATLAS magnet system: Technical Design Report, 1*. CERN, Geneva, 1997 [18](#), [19](#)
- [34] THE ATLAS COLLABORATION: Readiness of the ATLAS Liquid Argon Calorimeter for LHC Collisions. In: *Eur.Phys.J. C* 70 (2010), S. 723–753 [22](#)
- [35] DEILE, M. ; DIETL, H. ; DUBBERT, J. ; HORVAT, S. ; KORTNER, O. u. a.: Performance of the ATLAS precision muon chambers under LHC operating conditions. In: *Nucl.Instrum.Meth. A* 518 (2004), S. 65–68 [24](#)
- [36] WOTSCHACK, J: *ATLAS Muon Chamber Construction Parameters for CSC, MDT, and RPC chambers*. CERN, Geneva, Apr 2008. – ATL-MUON-PUB-2008-006. ATL-COM-MUON-2008-008 [24](#), [25](#)
- [37] CHIODINI, G ; ORLANDO, N ; SPAGNOLO, S: *ATLAS RPC time-of-flight performance*. CERN, Geneva, Apr 2012. – ATL-MUON-PROC-2012-002 [25](#)
- [38] JENNI, Peter ; NESSI, Marzio ; NORDBERG, Markus: *Zero Degree Calorimeters for ATLAS*. CERN, Geneva, Jan 2007. – LHCC-I-016. CERN-LHCC-2007-001 [26](#)

- [39] JAKOBSEN, S: *Calibration, testing, commissioning and first data of ALFA at LHC*. CERN, Geneva, Sep 2011. – ATL-LUM-PROC-2011-002 27
- [40] JONES, R.W.L. ; BARBERIS, D.: The ATLAS computing model. In: *PoS EPS-HEP2009 (2009)*, S. 448 28
- [41] BROCHU, F ; DZHUNOV, I ; EBKE, J ; EGEDE, U ; ELMSHEUSER, J ; JHA, M K. ; KOKOSZKIEWICZ, L ; LEE, H C. ; MAIER, A ; MOSCICKI, J ; MUNCHEN, T ; REECE, W ; SAMSET, B ; SLATER, M ; TUCKETT, D ; STER, D Van d. ; WILLIAMS, M: *Reinforcing user data analysis with Ganga in the LHC era: scalability, monitoring and user-support*. CERN, Geneva, Jan 2011. – ATL-SOFT-PROC-2011-011 28
- [42] CACCIARI M., Salam G. ; G., Soyez: The anti-kt jet clustering algorithm. In: *JHEP 0804 (2008)*, S. 063 29
- [43] LAMPL, W. ; LAPLACE, S. ; LELAS, D. ; LOCH, P. ; MA, H. u.a.: Calorimeter clustering algorithms: Description and performance. In: *ATL-LARG-PUB-2008-002 (2008)* 29
- [44] THE ATLAS COLLABORATION: Local Hadronic Calibration. In: *ATLAS-LARG-PUB-2009-001 (2008)* 29
- [45] CLEMENT, C. ; AL.: Searching for direct gaugino production and direct slepton production with two leptons and missing transverse momentum at  $\sqrt{s} = 8$  TeV (supporting INT note), Tech. Rep. In: *ATL-COM-PHYS-2012-XXX (2012)* 30
- [46] THE ATLAS COLLABORATION: Commissioning of the ATLAS high-performance b-tagging algorithms in the 7 TeV collision data. In: *ATLAS-CONF-2011-102 (2011)* 30
- [47] THE ATLAS COLLABORATION: Expected Performance of the ATLAS Experiment - Detector, Trigger and Physics. In: *hep-ex (2009)* 30
- [48] THE ATLAS COLLABORATION: Determination of the tau energy scale and the associated systematic uncertainty in proton-proton collisions at  $\sqrt{s} = 7$  TeV with the ATLAS detector at the LHC in 2011. In: *ATLAS-CONF-2012-054 (2012)* 30
- [49] E. DAWE E., D. O. ; PROTOPOPESCU, S.: *Using Boosted Decision Trees for Hadronic Tau Identification, Tech. Rep.* CERN, Geneva, 2011 30, 31
- [50] AL., M. B.: Herwig++ Physics and Manual. In: *Eur.Phys.J.C (2008)* 36, 37, 59
- [51] THE ATLAS COLLABORATION: Improved luminosity determination in pp collisions at  $\sqrt{s} = 7$  TeV using the ATLAS detector at the LHC. In: *arXiv (2013)* 37

- [52] GLEISBERG, T. ; HOECHE, Stefan. ; KRAUSS, F. ; SCHONHERR, M. ; SCHUMANN, S. u. a.: Event generation with SHERPA 1.1. In: *JHEP* 0902 (2009), S. 007 [38](#)
- [53] MANGANO, Michelangelo L. ; MORETTI, Mauro ; PICCININI, Fulvio ; PITTAU, Roberto ; POLOSA, Antonio D.: ALPGEN, a generator for hard multiparton processes in hadronic collisions. In: *JHEP* 0307 (2003), S. 001 [38](#)
- [54] FRIXIONE, Stefano ; WEBBER, Bryan R.: Matching NLO QCD computations and parton shower simulations. In: *JHEP* 0206 (2002), S. 029 [38](#)
- [55] KERSEVAN, Borut P. ; RICHTER-WAS, Elzbieta: The Monte Carlo event generator AcerMC version 2.0 with interfaces to PYTHIA 6.2 and HERWIG 6.5. In: *JHEP* (2004) [38](#)
- [56] SJOSTRAND, T. ; MRENNNA, S. ; SKANDS, P.Z.: A Brief Introduction to PYTHIA 8.1. In: *Comput. Phys. Commun.* 178 (2008), S. 852–867 [38](#)
- [57] THE UA2 COLLABORATION: A measurement of two-jet decays of the W and Z bosons at the CERN  $p\bar{p}$  collider. In: *Z.Phys. C - Particles and Fields* (1991) [40](#), [42](#)
- [58] COWAN, Glen ; CRANMER, Kyle ; GROSS, Eilam ; VITELLS, Ofer: Asymptotic formulae for likelihood-based tests of new physics. In: *European Physical Journal C: Particles and Fields* 71 (2011), Nr. 2, S. 1554 [43](#), [44](#)

---

# Acknowledgments

This thesis was written at Garching Forschungszentrum near Munich at Lehrstuhl Schaile. I would like to thank Prof. Dorothee Schaile for the opportunity to do research and write my masterthesis in the field of Supersymmetry. In terms of academic support my biggest thanks goes to my supervisor Federica Legger whose door was always open for questions and discussions and guided me throughout my year at the Lehrstuhl. My colleagues at the Lehrstuhl were also very helpful in academic discussions and they made this year a fun and fruitful experience.

I thank Johanna Sundberg for her great support and that she has brightened up every single day even though I spent a lot of time with thesis. I also have to thank her for early mornings in the office and I thank Nicolas Banane for late nights and discussions about physics and the universe.

Finally I thank my parents for their huge support throughout this thesis and all my life.

Erklärung:

Hiermit erkläre ich, die vorliegende Arbeit selbständig verfasst zu haben und keine anderen als die in der Arbeit angegebenen Quellen und Hilfsmittel benutzt zu haben.

München, den 2.08.2013